Spatial representation regularity and brain infra slow oscillation

Yifan Luo

Cognitive neuroscience

SISSA

Supervisor

Alessandro Treves

A thesis submitted for the degree of

Doctor of Philosophy

Trieste 2023

Abstract

Following a general introduction in Chapter 1, this thesis is divided into two main parts.

The first part, consisting of chapters 2 to 6, focuses on grid cells and spatial cognition. Chapter 2 provided a concise overview of the experimental results on spatial representations. Chapter 3 introduces various models that have been proposed to elucidate the formation of grid cells. In chapters 4 and 5, we investigate our model of grid pattern formation based on adaptation follow questions include grid pattern in non-planar environments like a burrow environment, grid pattern anchoring in a square environment, and grid pattern distortion in an irregular environment like a trapezoid environment. In Chapter 6, due to the increasing complexity and richness of functions attributed to grid cells being described recently, we aim to describe the basic encoding properties of grid cells with a simplified self-organized model.

The second part, encompassing chapters 7 to 9, is dedicated to exploring another form of regularity representation in the brain, which is brain oscillations. Specifically, our focus lies on infra-slow oscillations with periods lasting around several hundred seconds, observed in the frontal and parietal cortex during both natural sleep and anesthesia. In Chapters 7 and 8, we performed analyses of recordings obtained during natural sleep, exploring the intricate properties of infra-slow oscillations and their interactions with oscillations at faster timescales. Transitioning to Chapter 9, we shifted our attention to analyzing recordings acquired during states of anesthesia.

Contents

List of Figures

Chapter 1

General Introduction

Knowing where one is, where to go, and how to get there are some of the most fundamental and important challenges faced by all animals. Spatial cognition is the concept from neuroscience that concerns questions that appear from these topics.

The hippocampus formation and its surrounding areas are particularly appealing for spatial cognition study due to two reasons: Firstly, it exhibits a relatively simple architecture, which, if not entirely, is definitely much easier and better defined than other cortex areas. It shapes a comprehensible hierarchical structure with the hippocampus sitting at the top, receiving multiple lines of converging inputs. Secondly, the recording of local activities shows a close correlation with many spatial concepts, such as location, direction, distance, speed, and time, among others. Although explicit explanations about the questions we have and the mechanisms the brain employs are still a work in progress, the knowledge accumulated based on what is already known enables us, at the very least, to attempt defining a division of work among these areas. It helps us describe the mechanisms underlying the generation of various types of representations, specific computations involved, and their respective roles in the process.

The information conveyed through spatial concepts is stored in the firing patterns of individual neurons and the collective activity patterns of neuron ensembles. Recent research has revealed the mechanisms behind these neural codes and their role in spatial cognition. Two types of neuron firing patterns in the hippocampus formation encoding locations may sit at the top of the information flow hierarchy, which are place cells (O'Keefe, Dostrovsky, 1971) and grid cells (Fyhn et al., 2004; Hafting et al., 2005). Discovered at a distance of 30 years from one another, they are the prominent neuron types found in the hippocampus and in the medial entorhinal cortex, respectively. Grid cells sit one synapse away from hippocampal place cells both as an input and output of the hippocampal circuit (Kloosterman et al., 2003; Witter,

Moser, 2006). The relationship between place cells and grid cells is demonstrated by their similarity in representation, although they remain distinct in their response to changes in the environment, and appear to rely on different dynamic processes.

Grid cells are remarkable for their remarkable regularity. The regularity of the grid pattern allows for more accurate and efficient spatial navigation, as the individual can use the grid pattern as a reference point to determine their location relative to their surroundings. Research also suggests that the regularity of grid cell patterns may be important for other cognitive functions such as memory consolidation and decision-making, further highlighting the importance of precise spatial cognition for overall cognitive performance.

After a general prologue on spatial cognition (Chapter 2) and the computational mechanism of grid cell modeling (Chapter 3), we investigate the formation of grid patterns in a realistic burrow environment in chapter 4, using a virtual rat to explore it and allowing the simulated mEC units to form patterns through a self-organization process. Our findings show that the mEC units can create a stable representation of the entire environment. However, due to the limited size of the chambers in natural burrows, the grid units can only express a few fields, and the symmetry structure is only locally observed. By incorporating these results, we are able to better understand the process of grid pattern formation in real-world scenarios.

We then proceed to chapter 5, we put forward the idea that the grid cell firing pattern is not solely determined by the path integration information that would result in a hexagonal grid pattern. Instead, it also responds to local information and long-range correlations, which could potentially lead to shifts or distortions in the grid pattern. We try to clarify this idea by simulation with a virtual rat sampling the environment with a biased strategy of the border area to account for the phenomenon that the grid pattern is stably anchored to the wall in the square environment with a 7.5° (Stensola et al., 2015), and reduce the frequency of changes in running direction to let the virtual rat trajectories contain more long-range correlation can be captured by self-organization model to show long-range correlation would cause the grid pattern distortion in irregularly shaped environments such as trapezoids.

Then in chapter 6, based on the recent experimental results and simulation findings regarding pattern formation of mEC units in burrow environments, we proceed with a discussion on grid cell encoding properties with a simplify self-organized model.

This thesis is divided into two main parts. below is the second part which centers around oscillations, particularly infra-slow oscillations, which are often associated with regularity and periodicity.

From chapter 7 to chapter 9, our focus shifted to brain oscillations, which play a significant role in representing the regularity of brain activity (Buzsáki, 2006). Specifically, we delved into the study of infra slow oscillations in freely behaving rats, as well as in anesthetized rats.

In chapter 7, from freely behaving rats, infra slow oscillation range of around several hundred seconds appeared clearly. Detailed properties were analyzed in this chapter. In chapter 8, we show that infra slow oscillations in several frequency bands exhibit bimodality, which characterized by a relatively abrupt transition between high and low values. Furthermore, different frequency bands display distinct coupling structures. In chapter 9, we conducted an analysis of infra slow oscillations in anesthetized rats. These oscillations manifest in various forms, including upper envelope, lower envelope, up state duration, down state duration, state duration, up/down duration ratio, and up/state duration ratio. Furthermore, the different frequency bands are all coupled together.

Chapter 2

Introduction of Spatial Cognition and Oscillation

Spatial cognition can be described as the study of how humans and animals perceive, process, and use spatial information to navigate through their environment and interact with objects in space. It encompasses a range of mental processes such as perception, attention, memory, reasoning, and problem-solving that are involved in spatial tasks like wayfinding, map reading, spatial orientation, and spatial memory (Waller, Nadel, 2012).

Traditionally, research on the brain has mainly focused on studying the earliest sensory areas, particularly those associated with the early visual stream (Hubel, Wiesel, 1959, 1998). However, efforts to study regions further downstream have been met with challenges due to the complexity of the neural activities and structures involved. Recent advances in spatial cognition research have been a significant step forward, revealing that neurons in the hippocampal formation and related areas provide detailed representations of spatial information (Waller, Nadel, 2012; Moser et al., 2017; Hardcastle et al., 2017). These findings highlight the potential for investigating neuronal coding beyond typical sensorimotor processing and extending our understanding into the more complex cortices that govern higher-level cognition. This presents exciting opportunities for further exploration and discovery in the field of neuroscience.

Recent research has revealed a variety of different types of spatial representations in the brain. These start with place cells (O'Keefe, Dostrovsky, 1971), which are followed by head direction cells (Ranck, 1984; Taube et al., 1990a,b), grid cells (Fyhn et al., 2004; Hafting et al., 2005), and border/boundary vector cells (Solstad et al., 2008; Lever et al., 2009), among others. Many of the results are from the hippocampus. Together, these different types of cells create a diverse family that narrates a

fascinating scientific story about spatial cognition. As more research is conducted in this area, it is likely that new members of this family will continue to be discovered, providing even deeper insights into how the brain interprets and represents spatial information.

This chapter will provide a brief review of some experimental findings that will serve as the foundation for subsequent discussions on modeling studies. Some of these findings will be revisited throughout the thesis.

2.1 Hippocampus and place cells

Anatomically, both the rodent and primate (human included) hippocampus that have been heavily studied can be subdivided into three primary sub-regions (dentate gyrus (DG), CA3, and CA1). These regions differ in their connectivity, interneurons, and projection neurons (Andersen et al., 2007; van Strien et al., 2009).

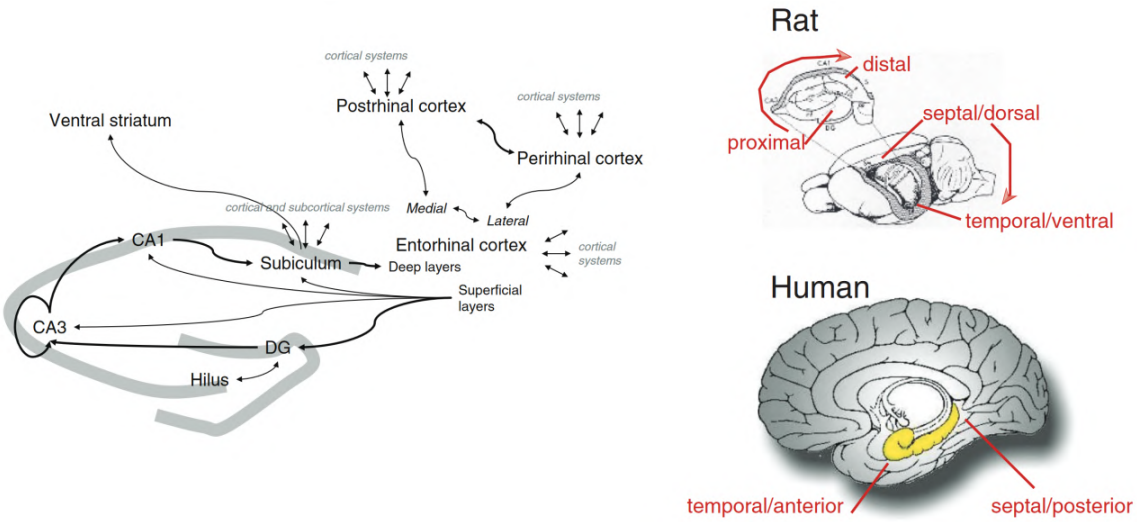

Figure 2.1: Hippocampal anatomy in the rat and human. The diagram on the left is based on the details known from rat anatomy. On the right, the image shows the comparative location of the hippocampus in both rats and humans. Adapted from (Waller, Nadel, 2012).

The activity of place cells in the rodent hippocampus is one of the most notable encoding patterns that reveal how complex cognition is represented in neurons (O'Keefe, Dostrovsky, 1971; O'Keefe, 1976). These cells exhibit an increased firing rate when the animals enter specific areas of their environment, as depicted in Figure 2.2. Building upon this observation and drawing inspiration from Tolman's concept

of cognitive map in the brain, O'Keefe and Nadel proposed that place cells are fundamental components of an allocentric spatial cognitive map in animals (O'Keefe, Nadel, 1979). Place cells exist in all three sub-regions of the hippocampus (DG, CA3, CA1), but in the DG, the place fields tend to be more sparsely distributed (Gothard et al., 2001; Jung et al., 1994) and responsive to subtle changes in the environment (Leutgeb et al., 2007).

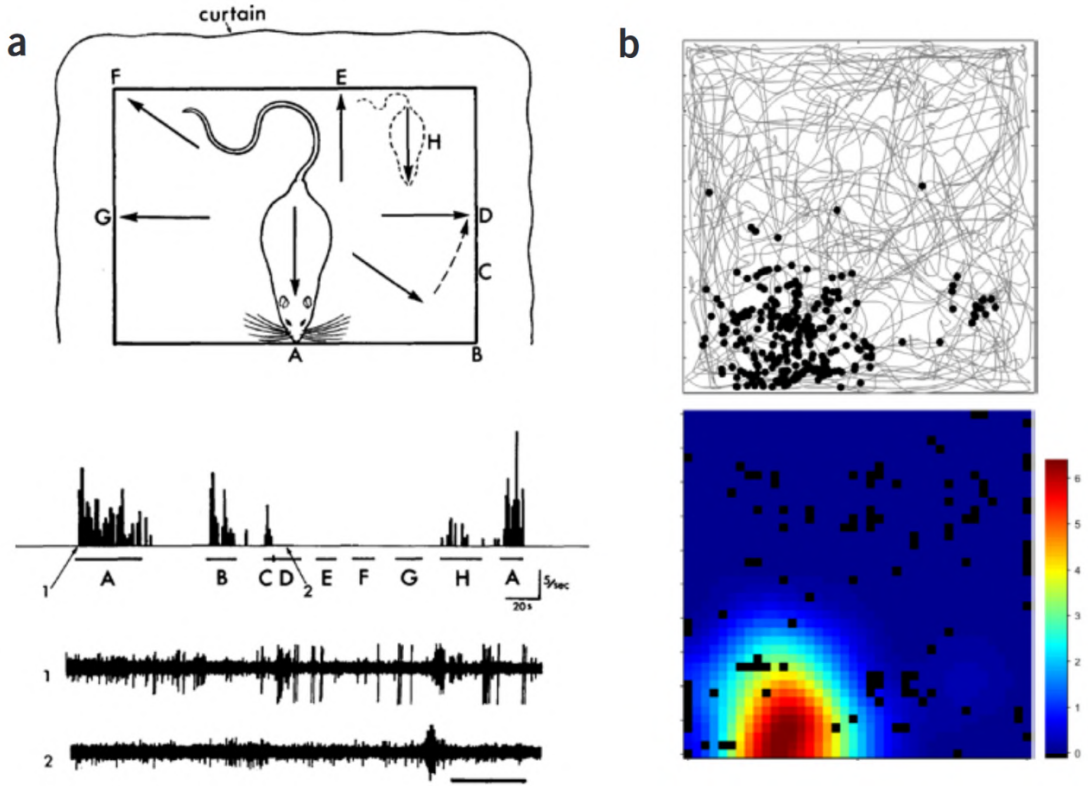

Figure 2.2: Place cells. (a) First place cell described(O'Keefe, Dostrovsky, 1971). (b) An example of the spatial distribution of spikes from a hippocampal place cell is illustrated. On the top, the trajectory of the rat is depicted as a gray line, while the spike locations of this particular cell are superimposed as black dots. The bottom section shows a color-coded rate map, where dark red represents the maximum firing rate of the corresponding place cell. The blue color indicates silence, and the region surrounding the maximum firing rate, which also exhibits a relatively higher firing rate, is referred to as the 'place field' of this place cell. Adapted from (Moser et al., 2017).

In the following, we will explore the characteristics of place cells, which can be classified into three main categories: single-cell properties, firing sequence, and context sensitivity.

2.1.1 Encoding properties of place cells

A typical place cell in the hippocampus is characterized by a confined firing field known as a place field, which corresponds to a specific spatial area within an experimental environment. The environment in which the majority of place cell properties have been described is typically a standardized cylinder with a diameter of 1 meter or a square box with sides measuring 1 meter. Different place cells exhibit distinct place fields, which can vary in terms of their shape, size, and intensity of firing. However, the exact significance of these variations remains uncertain.

Along the dorsal-to-ventral axis, there is a clear trend of increasing size for corresponding place fields. Place cells in the dorsal region tend to have smaller place fields, whereas those in the ventral region exhibit larger place fields (Jung et al., 1994; Kjelstrup et al., 2008; Royer et al., 2010). This encoding structure allows for the representation of multiscale information about space (Fiete et al., 2008; Maurer et al., 2005). The presence of broad place fields provides an opportunity for different types of information to be integrated within a single cell. This may explain why the ventral hippocampus is often associated with contextual and environmental-emotional associations, as it enables the incorporation of diverse information within these larger place fields (Bannerman et al., 2004).

In a linear track, which can be viewed as a one-dimensional environment, many place cells exhibit preferential firing when the rat moves in one direction but not in the other. However, in a normal two-dimensional environment, most, if not all, place cells are omnidirectional. Additionally, in a three-dimensional environment, both bats (Yartsev, Ulanovsky, 2013) and rats (Grieves et al., 2020) have place cells that encode the three-dimensional space uniformly, indicating that these cells represent the spatial information across multiple dimensions.

Place cells are not limited to having only one firing field per environment. In a typical laboratory setting, which often consists of a small and regular environment, most place cells exhibit a single field. However, in larger and more complex environments, some place cells may display multiple firing fields. This is considered an adaptive mechanism that enables the efficient encoding of intricate and expansive surroundings (Fenton et al., 2008; Rich et al., 2014).

As animals traverse a place field of a specific place cell, the relationship between the timing of spikes in that cell and the local field potential theta oscillation at around 7 Hz undergoes a distinct alteration. Initially, the spikes of the place cell occur later in the theta cycle upon entering the place field, but they progressively shift to earlier

phases of the cycle upon exiting the field. This phenomenon, known as phase precession, refers to the change in the phase relationship between spikes and theta oscillation as an animal moves through a place field (O'Keefe, Recce, 1993; Skaggs et al., 1996). It is hypothesized that phase precession may serve as a potential mechanism for the binding and compression of sequential events, allowing for the integration of temporal information within the spatial representation of the hippocampus.

2.1.2 Sequence properties of place cells

In addition to exhibiting higher firing rates within their place fields, hippocampal place cells also display increased firing rates when the animal pauses or rests. Remarkably, by decoding the spatial location information from recorded hippocampal place cells, it becomes possible to reconstruct the trajectory that the animal has recently traveled. This phenomenon is referred to as replay, as it involves the reactivation or replaying of the neural activity patterns associated with the animal's past experiences or spatial navigation. Replay events are believed to play a crucial role in memory consolidation and the offline processing of spatial information (Frank et al., 2004; Kentros et al., 1998; Wilson, McNaughton, 1993, 1994).

When a rat is positioned at a choice point, it has been observed that the hippocampal place cells exhibit sequences of firing activity that create the illusion of the rat traversing a particular path, even though it has not physically done so (Davidson et al., 2009; Foster, Wilson, 2006; Gupta et al., 2010). This phenomenon is referred to as preplay, as it involves the representation of future trajectories before they are actually executed. These findings provide valuable insights into the mechanisms underlying critical functions in which the hippocampal formation is involved, such as the consolidation of long-term memory (Marr, Brindley, 1971; Sutherland, McNaughton, 2000) and future planning (Foster, Wilson, 2006; Diba, Buzsáki, 2007; Karlsson, Frank, 2009; Lansink et al., 2009). Preplay suggests that the hippocampus is not only involved in encoding past experiences but also in simulating and planning future spatial trajectories based on internal representations and contextual information.

2.1.3 Context sensitivity

The spatial representations in the hippocampus are heavily influenced by sensory input. If the external cues that provide spatial information change, the place cells may undergo shifts in the locations they represent. They can also become silent or exhibit

activity in different locations. Furthermore, the firing rates of place cells can be modulated in response to changing sensory input (Muller et al., 1987; Sharp et al., 1990; Bostock et al., 1991; Kubie, Muller, 1991). The term 'remapping' was introduced to describe these changes in the spatial representation of place cells. Subsequently, terms like 'global,' 'partial,' and 'local' remapping were coined to characterize how the ensemble of place cells responds to such changes (Knierim, McNaughton, 2001). The recruitment of various forms of remapping allows the hippocampus to possess a large capacity for encoding spatial information, enabling flexible and adaptive representations of the environment.

Research has demonstrated that changes in the way stimuli are represented by hippocampal cells can occur not only due to variations in spatial features, but also in response to variations in other nonspatial aspects of the environment, such as color (Bostock et al., 1991), texture (Young et al., 1994), and temporal stages of the experiment (Hampson et al., 1993). These findings suggest that hippocampal cells integrate information from multiple sensory modalities, responding conjunctively to both spatial and nonspatial variables. By considering the effects of these diverse environmental factors on neural activity, we can begin to develop a more comprehensive understanding of how the brain processes and represents complex stimuli in the world around us.

2.2 Entorhinal Cortex and Grid Cells

Following the initial discovery of place cells in the hippocampus, significant efforts have been dedicated to studying spatial cognition within and around this brain region. This led to numerous significant experimental and theoretical study results being proposed regarding the encoding of brain spatial information. One such result is the recordings in the dorsal medial entorhinal cortex (mEC), which is considered the interface of the hippocampus as it is only one synapse away (Kloosterman et al., 2004; Witter, Moser, 2006; Moser et al., 2014b). The detailed circuit is depicted in Figure 2.3.

2.2.1 Encoding properties of grid cells

The grid cell encoding patterns shown in Figure 2.4 indicate that cells in this region exhibit sharply defined firing fields, similar to those observed in the hippocampus. However, unlike hippocampal spatial encoding cells, each cell in the medial entorhinal

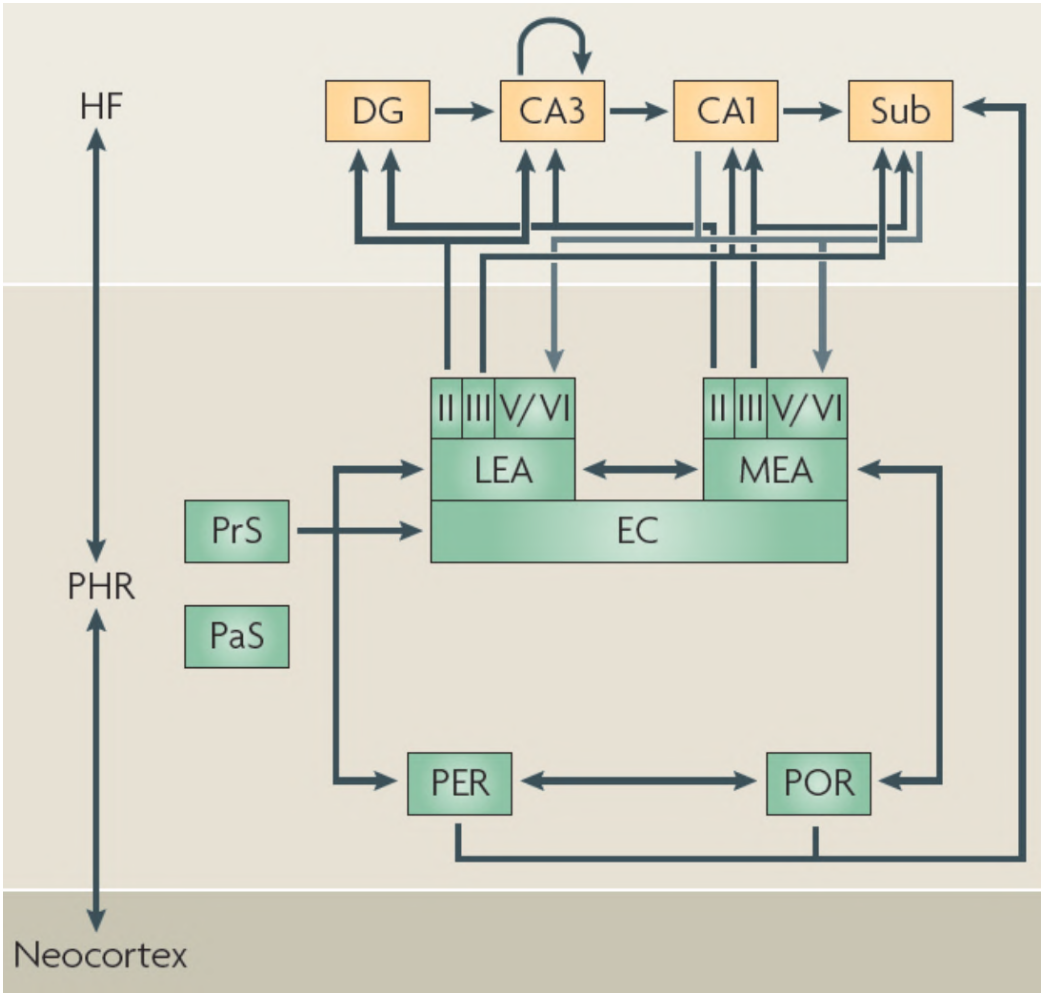

Figure 2.3: Schematic representation of the parahippocampal-hippocampal circuitry. According to this standard view, neocortical projections are aimed at the parahippocampal region (PHR), which in turn provides the main source of input to the hippocampal formation (HF). The EC has projects to all subregions of the hippocampal formation. Entorhinal layer II projects to the dentate gyrus (DG) and CA3, whereas layer III projects to CA1 and the subiculum (Sub). The Roman numerals indicate cortical layers. Adapted from van Strien et al. (2009).

cortex (mEC) has multiple firing fields that are distributed throughout the environment. These fields form a hexagonal grid, effectively tessellating the entire space available to the animal (Fyhn et al., 2004; Hafting et al., 2005).

The grid is characterized by its orientation relative to the environment, spatial phase (location), period (distance between fields), as well as the size and firing rates of its firing fields.(Hafting et al., 2005; Stensola et al., 2012; Tukker et al., 2021).

In layer III and deep-layer of mEC, grid cells were found also encoding head directions, shown in Figure 2.4 d (Sargolini et al., 2006). Phase precession is commonly

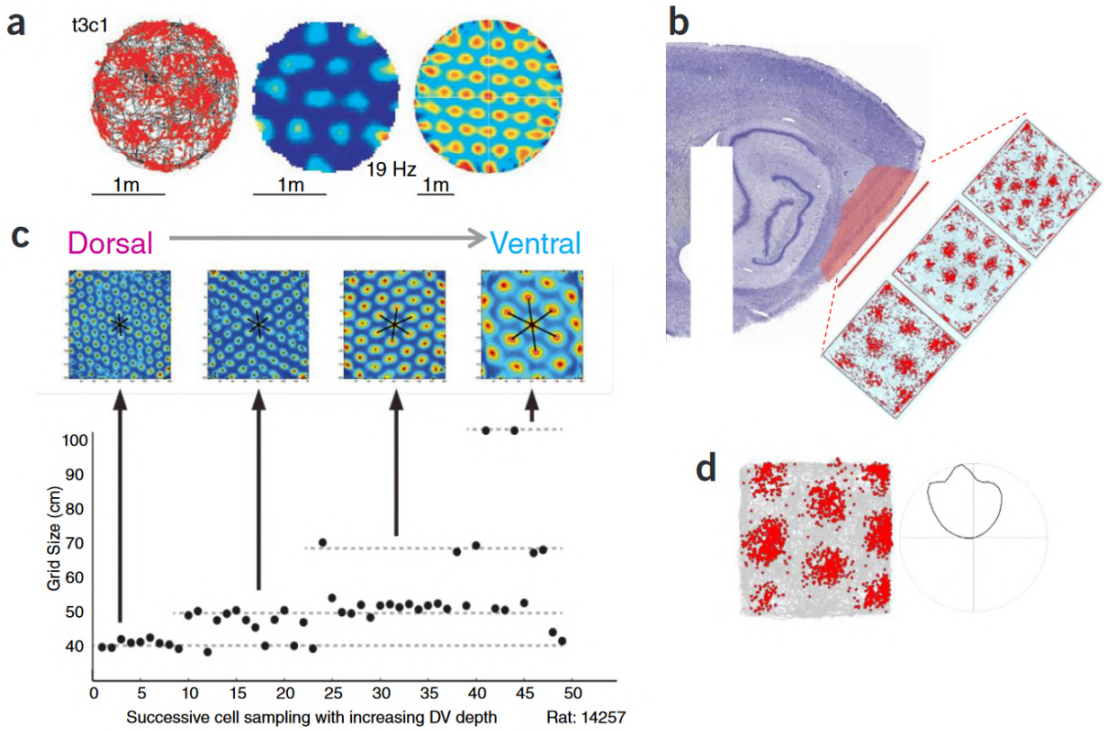

Figure 2.4: Grid cells. (a) Firing patterns of one of the first grid cells reported in Hafting et al. (2005). Left: black line indicates the trajectories of the rat with spike locations from this cell in red spots superimposed on top of it. Middle: color-coded rate map with peak rate indicated (peak rate to no firing represented from red to dark blue). Right: spatial autocorrelogram, color-coded from blue (r = –1) through green (r = 0) to red (r = 1). (b) Sagittal section of the rat brain showing the hippocampus and the MEC (red) and grid cells of different scales recorded at three locations on the dorsoventral axis (trajectories with spike locations as in a). Note that the expansion of grid scale changes from dorsal to ventral MEC. (c) Grid cells show module organization (Stensola et al., 2012). (d) Conjunctive grid × head direction cell in layer III of MEC. Adapted from Moser et al. (2017)

observed in layer II neurons in the mEC, it is not as prevalent in neighboring layer III neurons (Hafting et al., 2008).

The axes of the grids are offset from the walls by an angle of 7.5° degrees. This offset was proposed in order to minimize symmetry with the borders of the environment and enhance the distinctiveness of the grid patterns (Stensola et al., 2015).

Grid cell responds differently on one-dimensional tracks, the encoding fields are not arranged periodically, peak amplitudes vary across fields, and the mean spacing between fields is larger than in two-dimensional environments (Yoon et al., 2016). And in three-dimensional environment, only local order has been reported to reserved (Ginosar et al., 2021).

This spatially periodic firing pattern is originally considered to be independent of the geometric properties of the environment. However, experiments have pointed at increased irregularity and plasticity of grid activity patterns, whether due to large environments (Stensola et al., 2015), non-standard shapes (Krupic et al., 2015), modulation by local cues (Ismakov et al., 2017), boundary changes (Wernle et al., 2017) or the presence of goals (Boccara et al., 2019).

Experiments with monkeys have expanded the range of spaces that can be represented by grid cells. These experiments demonstrated the existence of neurons in the entorhinal cortex (EC) that exhibit firing patterns in a hexagonal lattice of on positions a screen, corresponding to the visual space being explored by the animals (Killian et al., 2012).

Grid cells, similar to place cells have been found to exhibit responses to non-spatial features in addition to their role in spatial representation (Aronov et al., 2017; Bellmund et al., 2018). For example, studies have shown that grid cells in the entorhinal cortex can encode information about reward-related variables, such as the anticipation and delivery of rewards (Aronov et al., 2017). These findings suggest that grid cells may play a role in reward processing and motivation. Furthermore, grid cells have also been found to respond to non-spatial sensory cues. In a study by Bellmund et al. (2018), grid cells in the entorhinal cortex of humans were observed to exhibit firing patterns modulated by visual cues, even without any spatial information. This suggests that grid cells may be involved in processing and integrating sensory information from different modalities, contributing to the formation cognitive of maps and spatial representations. The ability of grid cells to respond to both spatial and non-spatial features highlights their versatility and suggests their involvement in a wide range of cognitive processes. These findings provide further insights into the complex nature of grid cell function and their contribution to cognitive mapping and navigation.

Grid cells have not only been observed in the entorhinal cortex, but also in other brain regions such as the somatosensory cortex and visual cortex (Long, Zhang, 2021; Long et al., 2021). These findings suggest that grid cell-like properties may be present in multiple sensory modalities, indicating a broader role for grid cell networks in spatial representation and navigation across different sensory domains. The presence of grid cells in these diverse brain regions highlights the significance of spatial coding and suggests a potential integration of spatial information across various sensory systems.

2.2.2 Correlation between grid cells

Grid cells exhibit variations in grid spacing, grid phase, and grid orientation. It has been observed that grid cells in close proximity to each other tend to have similar grid orientations and spatial periods (Hafting et al., 2005; Stensola et al., 2012).

When a rat is introduced to a novel environment, the grid cells in its brain maintain a consistent pattern firing same the with field size and grid spacing. However, there are changes notable in the grid phase and orientation. Remarkably, these alterations occur consistently across all within cells same module (Fyhn et al., 2007).

By sampling a large number of grid cells across the dorsoventral axis within animals, researchers have identified four or five distinct modules characterized by a common grid spacing and orientation (Stensola et al., 2012). Interestingly, the increase in grid spacing along the axis appears to occur in discrete jumps, with a ratio approximately equal to $\sqrt{2}$, as depicted in Figure 2.4c. This finding suggests a systematic organization of grid cells, where the spacing between grid fields from proximity modules increases in a specific and consistent manner.

2.2.3 Context sensitivity

When a rat is placed in a new environment, the grid cells in its brain continue to fire a in consistent pattern with the same field size and grid spacing. However, there are notable changes in the grid phase and grid orientation. Interestingly, these alterations occur consistently across all nearby cells within the same module (Fyhn et al., 2007).

2.3 Other forms of spatial responses

In addition to place cells in the hippocampus and grid cells in the mEC, the brain employs various other mechanisms to encode spatial concepts and understand the relationships between objects and environments. These mechanisms enable us to comprehend and navigate the spatial world around us. Two important patterns involved in this process are head direction cells, and boundary cells or boundary vector cells.

2.3.1 Head direction cells

Head direction cells were first discovered in the postsubiculum of rats by Ranck in 1984 (Ranck, 1984). These specialized neurons exhibit firing activity when the rat's head is oriented within a specific range of directions, known as the preferred direction

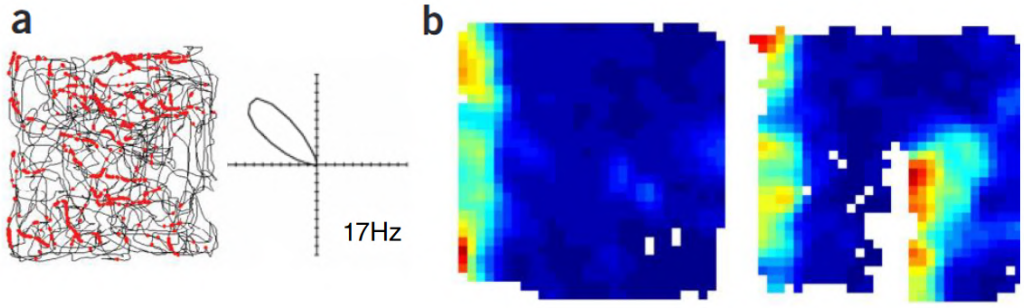

Figure 2.5: Examples of the firing patterns of a head direction Cell (left) and of a border Cell (right). a, a head direction cell, spikes are covering the whole environment when the head of the rat is heading upper right. b, a border cell, encodes the wall on the left side, when a new wall is introduced parallel to the left wall, a new field has appeared shown in the rate map on the right. Adapted from Sargolini et al. (2006) and Solstad et al. (2008).

and relatively remain silent for other directions. The firing rate of head direction cells typically follows a triangular or Gaussian tuning curve, with the highest firing rate occurring in the preferred direction and gradually decreasingly symmetric around it (Taube et al., 1990a,b).

Each head direction cell has a unique preferred direction, meaning that different cells within the head direction cell population are active for specific directions the rat is facing. This population of head direction cells collectively represents the full range of possible head orientations. By integrating the of activity these cells, the brain can establish a stable reference frame for spatial navigation and orientation, allowing the rat to accurately perceive its heading in the environment.

2.3.2 Border cells

Border cells are a type of neuron that exhibit activity near the borders of an environment. They were initially documented by Solstad et al. (2008); Savelli et al. (2008). These cells possess firing fields that undergo a change in location when the position of the subject shifts. Moreover, when new borders are introduced into the environment, additional firing fields are added. If two border cells fire along adjacent borders in one enclosure, they are likely to fire along adjacent borders in other similar boxes as well.

egocentric and allocentric border cells (Hinman et al., 2019; Gofman et al., 2019),

Egocentric and allocentric border cells are two subtypes of border cells that have been identified in the brain. Hinman et al. (2019) and Gofman et al. (2019) have

conducted studies on these cell types. Egocentric border cells are neurons that exhibit activity near the borders of an environment based on the individual's own position or viewpoint. These cells encode the position of the borders relative to the individual's own body or reference frame. Allocentric border cells, on the other hand, encode the position of the borders in relation to external cues or landmarks in the environment. These cells are not influenced by the individual's own position or viewpoint, but rather represent the absolute location of the borders.

The coexistence of grid cells, border cells, head and direction cells in the medial entorhinal cortex, presubiculum, and parasubiculum has been demonstrated in a study by Boccara et al. (0201). This study emphasizes the of importance integrating spatial maps with information on location and direction in the brain's navigation and orientation processes. The coexistence of these cell types suggests that the brain integrates multiple sources of spatial information to create a comprehensive representation of the environment. This integration allows for more navigation accurate and orientation in space. The medial entorhinal cortex, presubiculum, and parasubiculum are all involved in this process, highlighting their crucial roles in spatial cognition.

2.4 Brain oscillations

Oscillation refers to the rhythmic and repetitive motion or behavior observed in many natural and engineered systems. It is characterized by the regular and periodic variation of a system's state or output over time. Oscillations can have various frequencies, amplitudes, and waveforms. The concept of oscillation plays a fundamental role in understanding the behavior and dynamics of various natural and engineered systems. Understanding oscillations is crucial in many fields, including physics, engineering, biology, and social sciences. Oscillatory systems can exhibit remarkable properties, such as resonance, synchronization, and entrainment, which have important implications for the functioning of biological systems, the design of electronic circuits, the stability of power grids, and the dynamics of social networks.

The term "brain oscillations" or "neural oscillations" describes the rhythmic and repetitive electrical activity that occurs spontaneously or in response to stimuli in neural tissue within the central nervous system. The discovery of brain oscillations is often attributed to Hans Berger (1873-1941), who recorded the first electroencephalogram (EEG).

The frequency ranges of brain oscillations are typically divided into several bands, delta (0.5-4 Hz), theta (4-8 Hz), alpha (8-12 Hz), beta (12-30 Hz), and gamma (30-

100 Hz) (Cole, Voytek, 2017). Each frequency band has been shown to be associated with different cognitive and physiological processes.

In recent decades, there has been a growing recognition of the correlation of brain oscillations as with in sensory-cognitive processes (Ward, 2003; Buzsáki, Draguhn, 2004). Researchers have increasingly emphasized the functional significance of these oscillations in various cognitive functions, including perception (Busch et al., 2009), attention (Jensen et al., 2007), memory (Lega et al., 2012), and information processing (Fries, 2015).

Infra-slow oscillations (ISO), which are a form of low-frequency brain activity occurring at a rate below 0.1 Hz, are significantly slower than traditional neural oscillations (Aladjalova, 1957).

ISO has been observed in various regions of the brain, including the cortex, thalamus, and hippocampus. It is believed to play a crucial role in coordinating and integrating neural activity across different brain regions, thereby facilitating communication and information processing (Watson, 2018; Dash, 2019).

Chapter 3

Models of grid cells

The discovery of grid cells is followed with discussions about the mechanism behind the generation of grid patterns and their potential functions (Giocomo et al., 2011b; Zilli, 2012; Moser et al., 2014a; Moser, Moser, 2013; Moser et al., 2017).

Many studies have focused on related questions (O'Keefe, Burgess, 2005; Burgess, Barry, 2007; Giocomo et al., 2007; Hasselmo et al., 2007; Burgess, 2008; Fuhs, Touretzky, 2006; Burak, Fiete, 2009; Shipston-Sharman et al., 2016; Kropff, Treves, 2008; Si, Treves, 2013; DiTullio, Balasubramanian, 2021), and despite differences between these models, they can be categorized into a few common prototypes. Below, we outline three main subclasses:

- Continuous attractor neural network models
- Oscillatory interference models
- Self-organized models

3.1 Continuous attractor neural network models

Continuous attractor neural network models are commonly employed to simulate grid cells by utilizing an interconnected system of neurons that generates a continuous attractor landscape. In these models, each neuron is assigned a specific spatial position or virtual location, and the strength of connections between neurons varies based on their distance. The activity of these neurons can be conceptualized as a moving "bump" or peak of firing that dynamically traverses the network in response to stimuli. The process of translation is believed to rely on a mechanism of path integration, where changes in speed and direction continuously modulate the effective

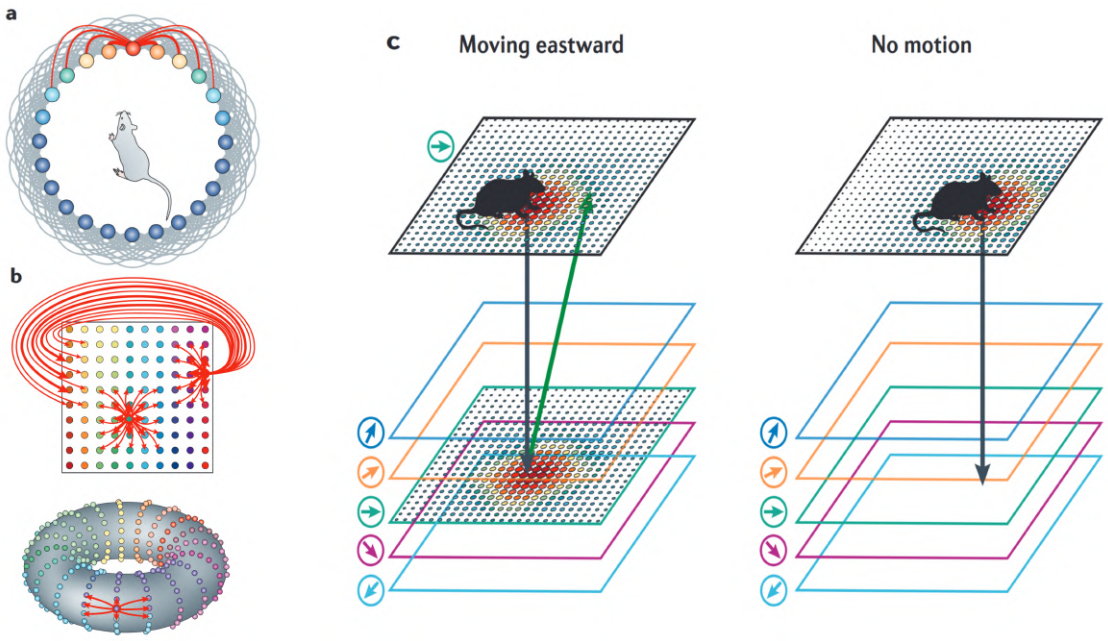

Figure 3.1: Schematic illustration of the continuous Attractor Neural Network Models. (a) One-dimensional continuous Attractor Neural Network, units are evenly distributed on a linear track (ring here to have a periodic boundary), and each unit connects with nearby cells with a synaptic strength (or connection probability) that declines as a function of distance. (b) Two dimensional continuous Attractor Neural Network, neurons are evenly distributed on a two dimensional space, the connections of neurons at the edges are wrapped around to create a periodic boundary. (c) By using an intermediate layer of cells that are conjunctive for position and head orientation, it is possible to make the bump move in correspondence with a rat's motion. Adapted from (McNaughton et al., 2006).

connectivity between cells (Zhang, 1996; Fuhs, Touretzky, 2006; Burak, Fiete, 2009; Shipston-Sharman et al., 2016).

Continuous attractor neural network models depend on the establishment of precise neural connections among neighboring neurons, which play a critical role in the formation of continuous attractors that are susceptible to noise. However, the requirement for precise connectivity in these models presents challenges when attempting to directly apply them as explanations for grid cells in the brain (Burak, Fiete, 2009).

3.2 Oscillatory interference model

The mechanism behind the generation of grid patterns is still a topic of ongoing research and debate. One proposed mechanism is the oscillatory interference model, which suggests that the grid pattern arises from the interaction between different

oscillatory frequencies in the entorhinal cortex. According to this model, the interference between these oscillations generates the hexagonal firing pattern observed in grid cells.

In the oscillatory interference model, the regular firing pattern of grid cells emerges within the cell as an interference results between a relatively constant theta oscillation with other internal or external theta oscillators with their frequency being modulated by the instantaneous velocity of the animals along a preferred direction (Burgess, Barry, 2007; Hasselmo et al., 2007; Burgess, 2008; Hasselmo, Brandon, 2008). The interference between each oscillator and the reference membrane oscillation results in the creation of bands of activity that have the same orientation as the preferred orientation of the oscillator that is modulated by velocity. As a result, if the velocity-controlled oscillators are oriented 60 degrees apart, it is expected that a periodic spatial activity with a hexagonal shape will be observed. The oscillatory interference model provides a theoretical framework for understanding how the interaction between theta oscillations and velocity-controlled oscillators can give rise to the characteristic hexagonal firing pattern observed in grid cells.

In this type of models, the exact neural circuits and regions involved in generating these oscillations are still under investigation, potential candidates include the medial entorhinal cortex, hippocampus, and other areas involved in spatial navigation and memory.

3.3 Self organization models

Self-organization models involve the identification of principles and mechanisms that lead to the spontaneous emergence of specific temporal or spatial patterns through interactions among individual units. Analyzing the properties of dynamical systems in self-organization models requires the use of mathematics, physics, and computer simulations (Karsenti, 2008).

In the context of grid cells, self-organization models emphasize the development of the network and the emergence of spatial patterns, rather than relying on specific hypotheses about network connectivity patterns (Kropff, Treves, 2008; Mhatre et al., 2012; Grossberg, Pilly, 2012; Pilly, Grossberg, 2013; Castro, Aguiar, 2014; Widloski, Fiete, 2014; Stepanyuk, 2015; DiTullio, Balasubramanian, 2021). These models aim to understand how grid cell firing patterns can arise through the self-organizing properties of neural networks, without explicitly specifying the exact connectivity patterns.

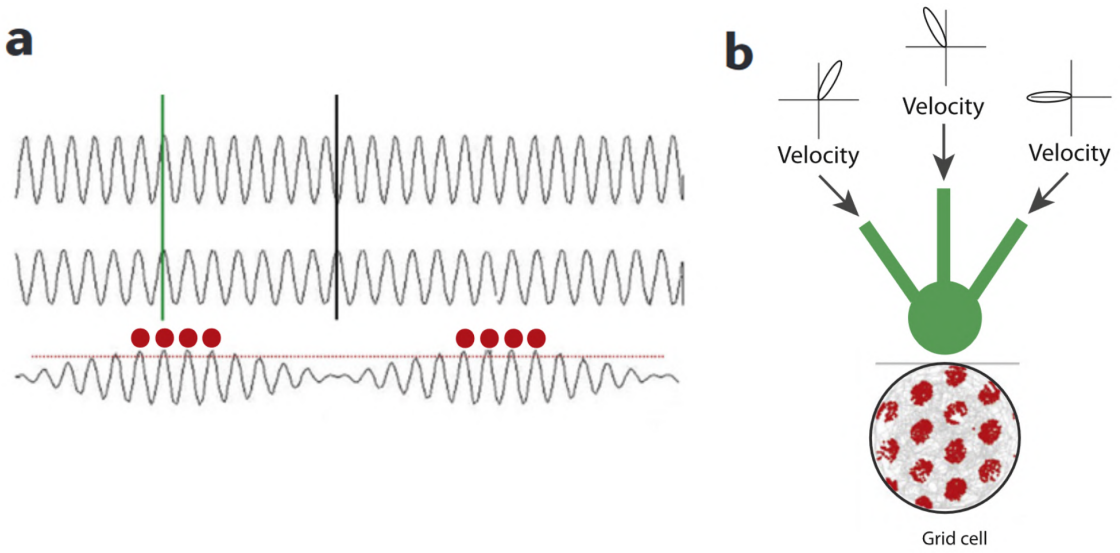

Figure 3.2: Schematic illustration of the interference model. (a), Example of interference between a single dendritic oscillation and a soma oscillation. When two oscillations are in phase (green line), their summation can result in a larger amplitude of the membrane potential fluctuations of the neuron, which is large enough to cross the threshold for action potential firing and generate a spike (red dot). On the other hand, if the summation of the oscillations does not reach the threshold for action potential firing, no spikes will be generated. (b) Top: the speed-modulated head direction input affect the frequency of oscillations in three different dendrites, three different head direction inputs have preferred firing directions offset by 60 degrees relative to each other, when the dendritic oscillations interact with the baseline soma oscillation, an interference pattern has been generated. Bottom: Applying a threshold to the interference pattern generatedcan produce a firing pattern that resembles that of grid cells. Adapted from (Giocomo et al., 2011a).

By focusing on the self-organization of spatial patterns, these models offer valuable insights into the development of grid cells and their characteristic firing properties. They provide alternative perspectives on the underlying mechanisms, moving away from pre-determined connectivity patterns and instead focusing on the emergent properties of neural networks. These models shed light on how grid cells can form their hexagonal firing patterns through the interactions and dynamics within the network. By simulating the self-organizing properties of neural networks, they contribute to our understanding of how spatial representations emerge in the brain.

Different models can indeed provide us with different perspectives on the properties of grid cells. Each model may make different assumptions, incorporate different mechanisms, or focus on different aspects of grid cell behavior. As a result, they can offer unique insights into the underlying mechanisms and functions of grid cells.

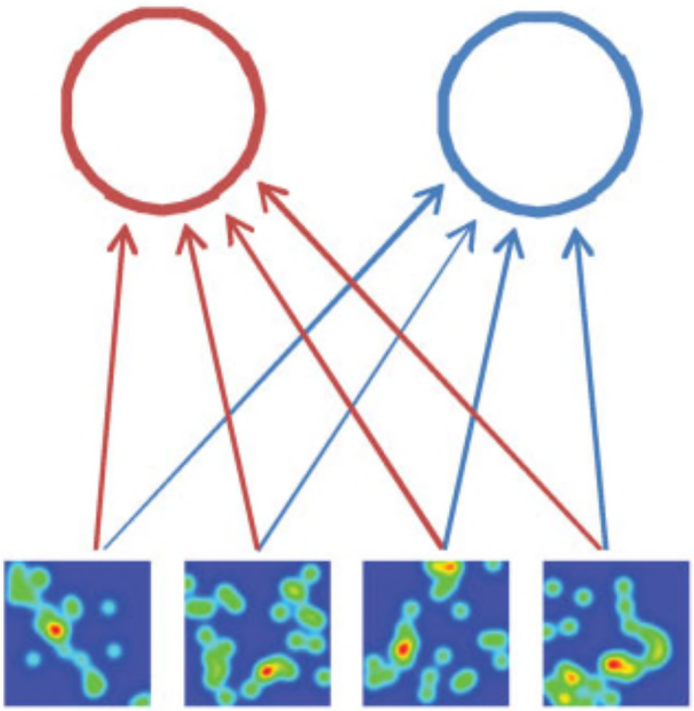

Figure 3.3: [Schematic illustration of the self organized model. The input layer supplies the second layer mEC units with spatially modulated input. Through synaptic adaptation, mEC units undergo self-organization by modifying their activity levels and strength of the connections between each other. As a result, the units in mEC organize themselves into a hexagonal grid pattern. Adapted from (Kropff, Treves, 2008).

For example, continuous attractor network models emphasize the role of attractor dynamics and synaptic connectivity in generating grid-like firing patterns. These models provide insights into how grid cells maintain their firing patterns and update them based on self-motion cues.

On the other hand, oscillatory interference models highlight the importance of theta oscillations and their interaction with velocity-controlled oscillators in generating grid cell firing patterns. These models provide insights into how grid cells integrate temporal and spatial information to encode the animal's position in space.

Self-organization models focus on the emergence of grid-like firing patterns through the interactions and plasticity of the network. These models provide insights into grid how cells may develop their firing properties without relying on pre-determined connectivity patterns.

By considering and comparing these different models, we can gain a more comprehensive understanding of the properties and mechanisms of grid cells. Each model

offers a unique perspective to contribute and our overall knowledge of how grid cells function in spatial navigation and cognition.

Chapter 4

Grid cells in wild

4.1 Introduction

The nervous system acquires from experience multiple representations of the external world. Extensively studied examples are in the hippocampus and adjoining cortices of rodents and other small mammals, near the apex of their cortical hierarchy(Felleman, Van Essen, 1991). There, the position of the animal in its immediate surroundings and other spatial variables are clearly prominent correlates of neural activity, as exemplified by 50 years of research on place cells (O'Keefe, Dostrovsky, 1971), but high level representations have been described also for other variables, including time(MacDonald et al., 2011; Buzsáki, Tingley, 2018), auditory frequency(Aronov et al., 2017), odours(Eichenbaum et al., 1987; Taxidis et al., 2020) and taste(Herzog et al., 2019). Spatial representations have been thoroughly studied in the laboratory, yielding amazing results (Moser et al., 2017) but in conditions rather different from those prevailing in the wild. The medial entorhinal cortex (mEC), one synapse upstream of and a major source of inputs to the hippocampus, includes numerous functionally-defined cell types contributing to spatial representations. Significant fractions of its cells have been characterized as grid cells(Hafting et al., 2005), border cells(Solstad et al., 2008), head direction and conjunctive cells(Sargolini et al., 2006), speed cells(Kropff et al., 2015) and irregular spatial cells(Diehl et al., 2017). Should we understand this characterization as encompassing the different components of a precisely engineered system, or as a list of some of the most salient properties expressed by this population of neurons, which is however not rigidly partitioned into cell classes? The question is made more relevant by the failure, over the years, to identify a precise correspondence of such putative classes with cell properties observed in other species, notably in primates.

Place cells fire action potentials when the animal moves through locations in the environment, specific to each cell, called place fields. A simple intuitive model envisages place cells as being assigned, at random, each a location in the environment to represent with its activity, so that at a population level from the list of cells active at a moment in time one can easily decode the position of the animal – who effectively, then, has available a spatial map with its own position annotated on it. This model does not seem outrageously inappropriate, particularly given that the majority of place cells show only one field in the classical laboratory environment, typically smaller than $1m^2$. Several recent experiments, however, show that in larger environments place cells often have multiple and irregularly arranged place fields(Fenton et al., 2008; Park et al., 2011; Rich et al., 2014; Harland et al., 2021). Still, since the multiple fields are irregularly arranged, one expects that a different list of active cells will uniquely identify each location. Thus place cells, on their own, should effectively represent or map a number of locations in space exponential in the number of cells considered. Even huge environments could be mapped by a sufficient number of place cells.

The effectiveness of the spatial code would appear more doubtful with grid cells, discovered later in the medial entorhinal cortex (mEC)(Hafting et al., 2005). At least in the simplest intuitive model, each grid cell fires at multiple discrete spaced locations, regularly arranged on a hexagonal pattern that tiles the entire space available to the animal in a laboratory environment. Taken to the extreme, the model would predict that the list of active cells is the same at all locations situated on the hexagonal pattern, which the code would then be unable to distinguish. But are the intuitive models abstracted from experiments in the lab relevant to ecological conditions, where these neural systems have evolved over millions of years?

In this paper, we focus on the pattern formation process of grid cells, based on feed-forward spatial information contributed by place cells, as expressed in our self-organizing adaptation model.

The spatial representations expressed by grid cells and place cells have been reported to differ substantially in the amount of local information they incorporate. Place cells can show global remapping, given sufficient changes in the external environment (Latuske et al., 2018), indicating that they are highly influenced by local spatial information. Grid cells, at least in flat regular environments, do not show global remapping, once the population as a whole has been *anchored* to the local environment (Stensola et al., 2015). Major changes in the environment, which cause the

global remapping of place cells, on an individual basis, appear to induce only a coherent population realignment by grid cells(Fyhn et al., 2007). Subsequent experiments have partially qualified these results, by showing that the grid pattern is influenced by walls(Barry et al., 2007), unstructured but oddly shaped environments(Krupic et al., 2015), local cues(Ismakov et al., 2017), goals(Boccara et al., 2019). The simple radical notion that grid cells provide a universal spatial metric has therefore been challenged. In addition, in the search of grid patterns in 3D environments, only local order, expressed e.g. by relatively uniform inter-field distances, has been seen to be partially preserved (Ginosar et al., 2021), in agreement with the theoretical predictions of the self-organizing adaptation model in 3D (Stella, Treves, 2015).

To better understand the spatial selectivity expressed by grid cells, it seems increasingly urgent to move out of artificial laboratory settings. Grid cells have been observed in several species, including rats (Hafting et al., 2005), mice (Fyhn et al., 2008) and crawling bats (Yartsev et al., 2011), with related cellular selectivity also in monkeys (Killian et al., 2012) and humans (Doeller et al., 2010; Jacobs et al., 2013), pointing at some degree of universality underlying the phenomenon. These animals experience space in their natural environment, whether large scale 2D where they roam, or 3D where they swim, jump, climb and fly, or curved and crooked, for those who live in burrows. One could start by considering three simple types of geometry, flat 2D, 3D, and curved.

Flat 2D(Kropff, Treves, 2008; Si et al., 2012; Si, Treves, 2013; Urdapilleta et al., 2017), 3D(Stella, Treves, 2015), and curved(Stella et al., 2013; Urdapilleta et al., 2015; Stella et al., 2020) environments have indeed all been considered in studies of the grid pattern emerging with the self-organizing adaptation model.

In this paper, we aim to further our understanding of grid patterns in burrows, where rats, arguably the most frequently used species for the study of spatial representations, usually live in the wild (Calhoun, 1962; Schweinfurth, 2020).

Norway rats, a most common strain of rats widely used in research, usually referred to as the *common* rat, have seen their burrowing habits meticulously described by John B. Calhoun (Calhoun, 1962), with the original motivation to control their proliferation in the city of Baltimore. Calhoun has produced estimates of the quantitative characteristics of typical burrows housing ca. 11 adult rats: on average 10 chambers (2 terminal; 8 with at least 2 entrances), linked by 40 tunnels (including on average 13 to exits; 20 internuncial; 7 blind). A sketch is shown in Figure 4.1 left (Calhoun, 1962). On these descriptions we base our virtual burrows, generated by an

in-house algorithm, one of which is shown in Figure 4.1 right. The yellow line is an example of a simulated trajectory.

4.2 Simulation

4.2.1 The construction of the burrows

Our computer model generates virtual burrows with a simple geometry, in which the chambers are represented by spheres, of variable diameter, while the tunnels are schematized as sequences of short curved cylinders (i.e. sections of tori) of variable length and external (curvature) radii, and fixed internal diameter – just enough for a virtual rat to run through. Spheres are thus assigned a center and a diameter, while curved cylinders are defined by a circular basis (with a fixed diameter and a centre and normal versor such that it lies on a sphere, or at the end of another tunnel segment) which is then translated along an arc of circumference (with parameters the versor and magnitude of the curvature radius, and the arc length). Additionally, we draw on the work of Calhoun (Calhoun, 1962) to define probability distributions for e.g. the diameters of the spheres and the lengths of the tunnels.

Burrow construction proceeds by generating a given number of spheres, with diameters and center-center distances compatible with the observed chamber sizes and distribution of tunnel lengths. Then, the internal burrow connectivity develops, randomly split between chamber-chamber and tunnel-chamber tunnels. Finally, some blind and exit tunnels are added.

The tunnels start with an existing object - sphere or tunnel - and define the initial segment of the new tunnel as a short, straight cylinder with the basis circumference

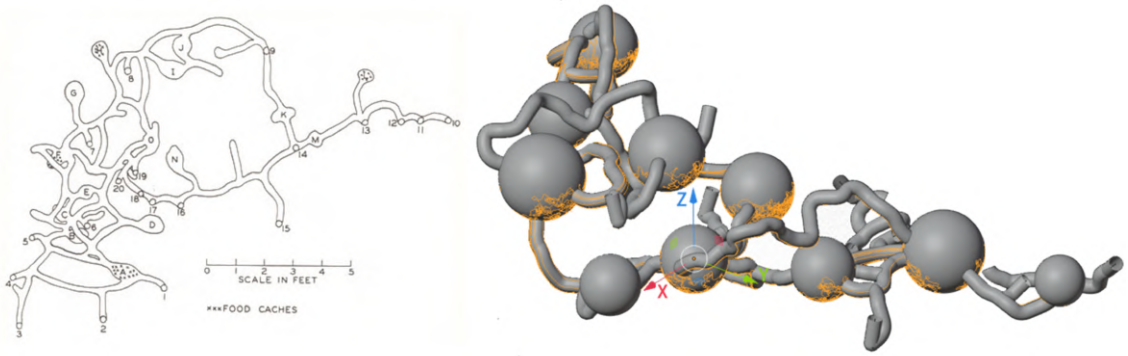

Figure 4.1: Left, sample map of a Norway rat burrow (Calhoun, 1962). Right, a simulated rat burrow environment which contains 10 sphere representing chambers and 29 tunnels.

tangent to the preexisting object at a random location, then new curved segments are added, with a basis that coincides with the top of the previous one (same centre, radius and normal versor), while the remaining parameters are randomly generated. The tunnels terminate after randomly growing in random directions for a random length if blind tunnels, when penetrating a target sphere or tunnel if internuncial tunnels, or upon reaching a predefined horizontal plane (i.e. the ground) if exit tunnels. In the last two cases, the direction of growth is biased towards the target destination, with a probability inversely proportional to the distance to the target, and we restrict the choice of the plane of the radial curvature so as to point towards the desired outcome.

4.2.2 Trajectories

In the simulations, a virtual rat explores one of the virtual burrows described above with a constant speed $v = 40cm/s$. Each time step in the simulation is taken to correspond to $10ms$ in real time. The total length of a simulation is 100 million steps (which would correspond to nearly 12 days of continuous running, to ensure that the self-organization process has approached its asymptote). To obtain smooth random trajectories, resembling those observed in experiments, the change in running direction in the chambers is sampled from a Gaussian distribution with zero mean and standard deviation $\sigma_{RD} = 0.2$ radians; in tunnels, since the size of the tunnels normally can only allow a single rat to pass, the running direction of the virtual rat is always following the tunnels. If the random trajectories lead the virtual rat to the junctions, the virtual rat changes sub-environment (from chamber to tunnel, from tunnel to chamber, or from tunnel to another tunnel). If the tunnel has a dead end, the virtual rat turns back when it reaches the end. The trajectories are limited to the lower half of the environment because of gravity.

4.2.3 Network model

The model is comprised of two layers. The input layer represents, for example, the CA1 region of the hippocampus and contains $N_{hip} = \rho S + L_t/l_c$ model place cells, which we refer to as *place units* below, where $\rho = 8000m^2$ is the density of input units in chambers, S is the total area of the chambers, L_t is the total length of the tunnels, l_c is the mean local inter distance of place units in tunnels. This guaranteed that the place units are equally distributed and cover the whole environment. The output

layer represents a population of $N_{mEC} = 100$ model mEC units, which we refer as *grid units* below.

The input to grid unit i at time t is given by

$$h_i^t = \sum_j W_{ij}^t r_j^t \tag{4.1}$$

Here we assume that grid units develop their maps from scratch, receiving spatially modulated inputs from the place units which have already developed, in line with observations in rat pups, which show that place cells mature earlier than grid cells (Langston et al., 2010; Wills et al., 2010).

Although weak spatial input is sufficient for grid pattern formation (Kropff, Treves, 2008), regularly arranged place cells are ideal for this function and reduce the averaging necessary for learning with respect to more irregular inputs. Here the activity of each place input unit in space is modeled as a Gaussian place field centered at preferred position $\vec{x}_{j0}$

$$r_j^t = \exp - \left(\frac{||\vec{x}^t - \vec{x}_{j0}||^2}{2\sigma_p^2} \right) \tag{4.2}$$

where $\vec{x}^t$ is the current location of the virtual rat. $||\cdot||$ is the shortest distance (distances in chambers are calculated along great circles, and in tunnels longitudinally, adding them up if $\vec{x}^t$ and $\vec{x}_{j0}$ are not in the same sub-environment). $\sigma_p = 5cm$ is the radius of the place fields.

4.2.3.1 Single-unit dynamics

The firing rate ψ_i^t of grid unit i is determined through a threshold-nonlinear transfer function

$$\psi_i^t = \psi_{sat} \arctan[g^t(\alpha_i^t - \mu^t)]\Theta(\alpha_i^t - \mu^t) \tag{4.3}$$

where $\psi_{sat} = 2/\pi$ normalizes the firing rate into arbitrary units. $\Theta(\cdot)$ is the Heaviside function. The variable μ^t is a threshold while α_i^t represents a time-integration of the input h_i, adapted by the dynamical threshold β_i

$$\begin{aligned} \alpha_i^t &= \alpha_i^{t-1} + b_1(h_i^{t-1} - \beta_i^{t-1} - \alpha_i^{t-1}), \\ \beta_i^t &= \beta_i^{t-1} + b_2(h_i^{t-1} - \beta_i^{t-1}) \end{aligned} \tag{4.4}$$

where β_i has slower dynamics than α_i, and b_2 is set to $b_2 = b_1/3$, $b_1 = 0.1$. These adaptive dynamics make it more difficult for a neuron to fire for a long period of time, and endow grid units with fatigue dynamics(Kropff, Treves, 2008). The gain g^t and threshold μ^t are iteratively adjusted at every time step to fix the mean activity $a = \sum_i \psi_i^t/N$ and the sparsity $s = (\sum_i \psi_i^t)^2/(N \sum_i \psi_i^{t\,2})$ within a 10% relative error bound from pre-specified values, $a_0 = 0.1$ and $s_0 = 0.3$ respectively.

4.2.3.2 Head direction modulation and collateral connections

Head direction (HD) modulation and collateral connections are important for grid alignment, as suggested by the detailed analysis in (Kropff, Treves, 2008; Si et al., 2012). The head direction in the chambers (spheres) is defined as the angle between a vector and the vector pointing toward the north pole.

With the addition of HD modulation and collateral connections, Eq.(4.1) for the inputs to grid unit i is rewritten

$$h_i^t = f_{\theta_i}(\omega_t)(\sum_j W_{ij}^{t-1} r_j^t + \rho_1^t \sum_k W_{ik}^{t-1} \psi_k^{t-\tau}) \tag{4.5}$$

where $\psi_k^{t-\tau}$ is the activity of other grid unit k reverberated by collateral connections W_{ik}^t with a delay $\tau = 25$ steps. $\rho_1^t = \varphi t/T$ when $t < T$ and φ when $t \geq T$, where $T = 5 \times 10^6$ for each simulation, φ is a set value controlling the strength of recurrent connections. Then the time-dependent strength ρ_1^t is gradually increasing from zero, in order to reduce the influence of the initial random weights.

$f_{\theta_i}(\omega_t)$ is the HD tuning function that has maximal value when the current head direction ω_t of the simulated rat is along the preferred direction θ_i.

$$f_\theta(\omega) = c + (1-c)\exp(v(cos(\theta - \omega) - 1)) \tag{4.6}$$

$c = 0.1$ and $v = 0.8$ are parameters determining the baseline activity and the width of head direction tuning.

4.2.3.3 Synaptic plasticity

All weights in the network self-organize while the virtual rat explores the environment and the updating following the Hebbian rule.

Weights between place units and grid units are changed according to

$$\Delta W_{ij}^t = \epsilon^t(\psi_i^t r_j^t - \bar{\psi}_i^{t-1}\bar{r}_j^{t-1}) \tag{4.7}$$

where $\epsilon^t = \xi(1 - 0.9t/T)$ when $t < T$ and 0.1ξ when $t \geq T$, here $T = 5 \times 10^6$, $\xi = 0.01$. $\bar{\psi}_i^t$ and $\bar{r}_j^t$ are estimated mean firing rates.

$$\begin{aligned} \bar{\psi}_i^t &= \bar{\psi}_i^{t-1} + \eta(\psi_i^t - \bar{\psi}_i^{t-1}), \\ \bar{r}_i^t &= \bar{r}_i^{t-1} + \eta(r_i^t - \bar{r}_i^{t-1}), \end{aligned} \tag{4.8}$$

and $\eta = 0.05$ is a positive averaging factor.

The collateral weights between grid units are adapted according to

$$\Delta W_{ik}^t = \zeta \psi_i^t (\psi_k^{t-\tau} - \kappa) \tag{4.9}$$

Here $\zeta = 6.6 \times 10^{-5}$ is a learning rate smaller, at least initially, than the learning rate for feed-forward weights between place units and grid units. $\kappa = 0.1$ is an inhibition factor.

All the weights in the network are initialized as random numbers $(1 - \gamma) + \gamma u$. $\gamma = 0.1$, and u is a random variable uniformly distributed in $[0, 1]$.

After initialization or weight changes, all weights are normalized to a unitary L_2 norm

$$\sum_j {W_{ij}^t}^2 = 1 \tag{4.10}$$

4.3 Results

In the simulations, grid units may have been expected to form highly regular patterns, as they do in flat 2D environments (Kropff, Treves, 2008). However, in our burrows, modelling the natural environment of real rats, the activity patterns that get established are not nearly as regular. Figure 4.2 shows the grid map of one sample unit. The lower half of the sphere, representing a chamber, was projected to a horizontal plane, while the upper half was discarded, as trajectories are limited to the lower half to model gravity. Tunnels were straightened into 1D segments. Sufficiently explored chambers show clearly identifiable fields, while those where the virtual rat spent less time show only blurred, often overlapping fields. Longer simulations make for little improvement. Tunnels, as they are 1D structures, are easier to learn and show clear fields even in shorter simulations.

The grid maps in a chamber include very few fields, as indicated in Figure 4.2 top. In fact, chamber width is at most 0.3m (reported as 298mm, with median 221mm and minimum 155mm (Calhoun, 1962)), unlike the 2m diameter of the flat circular enclosure used in the Moser lab (Hafting et al., 2005), and even considerably smaller than the small square boxes used earlier and in several later studies (e.g., $1.0 \times 1.0m$ (Fyhn et al., 2004)). Due to this reason, to be able to study the layout of the fields in a spherical chamber we have used larger diameters in our model curved environments, so they would include e.g. the 12 fields of the most regular pentagonal arrangement (Stella et al., 2013, 2020) (on the entire sphere, top and bottom, with 6 in the lower half).

For grid patterns to be stable, the feed-forward learning rate between place units and grid units has to be very small. As shown in Figure 4.2 bottom, with learning rate $\xi = 0.01$ grid units may keep shifting their fields as the simulation proceeds, so that their correlation with those at any reference time keeps changing; with learning rate $\xi = 0.001$ the stability is markedly improved, and with $\xi = 0.0001$ grid units appear to form stable maps both in chambers and in tunnels.

The gridness score has been widely used to quantify the spatial periodicity of grid patterns, but it can be applied only to patterns with six-fold symmetry. Results from simulations in curved environments show regular grid patterns with five-fold or lower symmetry for constant positive curvature, and seven-fold or higher symmetry for negative curvature (Stella et al., 2013; Urdapilleta et al., 2015). In the burrows simulated here, inter-field distances vary also within chambers (light blue distribution in Figure 4.3 top), indicating that spatial periodicity is not a property of grid cells in natural environments.

The inter field distances in tunnels (green distribution in Figure 4.3 top) have a larger peak value than in chambers. In chambers, in fact, our simulated trajectories are curved as the running direction keeps changing, unlike the trajectories in tunnels which can only follow the 1D tunnels, so the distance traveled over the adaptation time scale is longer in tunnels than in chambers. For real rats, of course, the distance traveled in each sub environment depends strongly on their prevailing speed, likely contributing to the different representation of grid cells in tunnels and chambers.

The virtual rat learns the entire environment at the same time, since the randomly generated trajectories span it all. We asked, then, whether grid units form a continuous representation of the whole environment, by checking whether the junctions connecting chambers and tunnels break the continuity. In Figure 4.3 bottom left, field B and field A are the closest fields to a junction, from the tunnel and chamber side, respectively, and x and y represent their distance from the junction, so that x = field distance $-y$. As shown in Figure 4.3 bottom right, x and y do not show the expected negative correlation (with -1 or with any other clear slope), but rather a loose relationship. This indicates that spatial representations by simulated grid units are effectively independent in distinct portions of the environment, as this is in practice partitioned up by the junctions.

Realistic simulated burrows like that in Figure 4.1 right require enormous CPU time to be explored with sufficient statistics, and even then the maps that form especially in the chambers often present rather unclear fields, as in Figure 4.2. Therefore, in the following analyses we consider a *simplified* burrow, with only three chambers

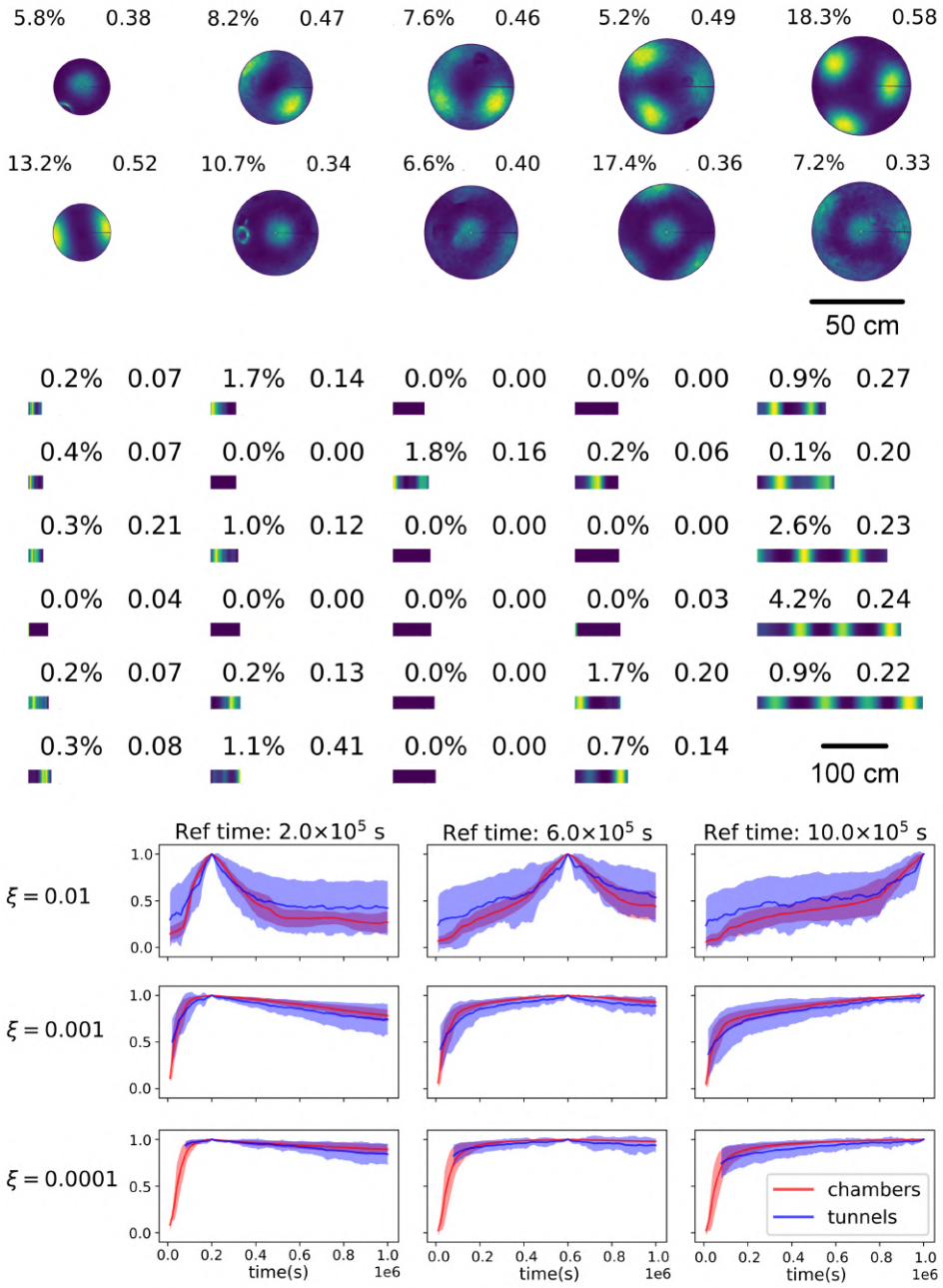

Figure 4.2: Grid maps in burrows and their stability. Top and center, the maps of one unit in chambers (the lower half of each chamber is shown), and in tunnels (straightened and taken to be 1D). Chambers (tunnels) are shown in order of radius (length), with the percent time spent in each by the virtual rat indicated top left, top right indicates the maximum firing rate (always in the range [0 ,1], given Eq.(3)). Bottom, from the first to the third row, the initial learning rate is lowered from $\xi = 0.01$ through $\xi = 0.001$ to $\xi = 0.0001$; while from the first to the third column, the reference time points are 2×10^5, 6×10^5, 10×10^5.

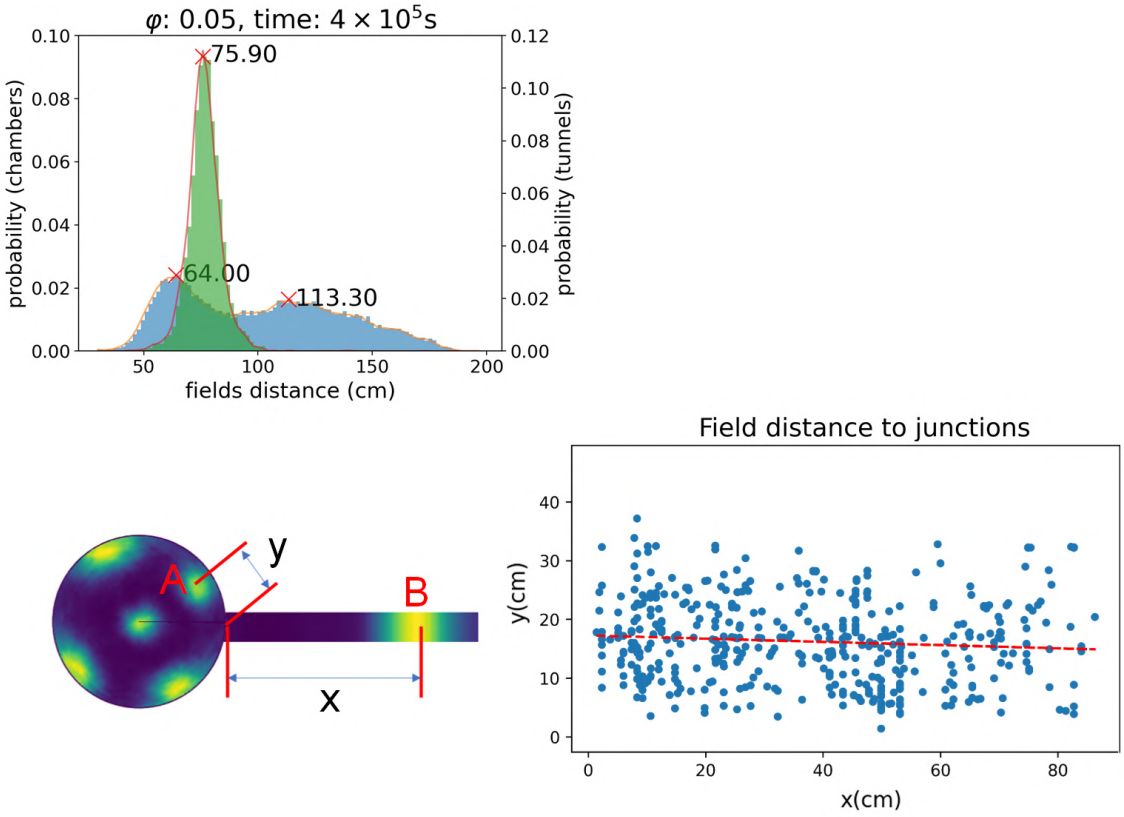

Figure 4.3: Top, inter fields distributions of fields in the same chambers and tunnels, indicating the location of the peaks. Bottom left, field A and field B are the closest fields to a junction, and y and x represent their distance to the junction from the chamber and tunnel side. Bottom right, the correlation between the x and y measures.

and three tunnels connecting them, and compare the maps emerging there with those in a square box or in/on a sphere. Since the gridness score cannot be readily applied, we use instead the distributions of inter field distance (left column of Figure 4.4) and of the angles between triplets of nearby fields (right column of Figure 4.4); such triplets are defined by mutual distance in the range of 50% to 150% of the first peak in the field distance distribution. We generated data for the square box environment setting the strength of recurrent connections at $\varphi = 0.125$, much stronger than in the sphere and burrow, where it was set at $\varphi = 0.05$, in order to have in each environment as regular grid patterns as they could be (see Figure 4.6 below). The effect of recurrent strength in different environments will be described in details later. Other parameters were kept constant.

The inter-field distance distribution in the box environment (of size $1.5 \times 1.5m^2$) has clear peaks, shown in Figure 4.4 upper left. The fourth and fifth peaks are shifted

to the left compared with those of perfectly regular six-fold grids, probably because the virtual trajectories are limited by the hard border (which reflects the trajectory as in a mirror when it hits the border). The angles have a distribution centered at 60 degrees, shown in Figure 4.4 upper right.

The spherical environment, with radius $r = 0.5m$, allows most grid units to develop 12 fields. Their distribution of field distances also has clear peaks (Figure 4.4 center left). The angle distribution is centered at 71.8 degrees (Figure 4.4 center right), just 0.2 degrees below the 72 degrees value of the perfectly regular five-fold grid pattern.

In the burrow environment, simulations have parameters consistent with those in the sphere. The field distance distribution does not have clear peaks, however (Figure 4.4 lower left). The angle distribution shows more variability than in the box and in the sphere (Figure 4.4 lower right). This suggests that the formation of regular grid patterns in natural environments, like rat burrows, is very challenging for the same system that produces them easily in laboratory conditions.

The grid maps of cells recorded at the same electrode position show generally a small correlation or rather an anti-correlation (Hafting et al., 2005), because even with similar grid spacing and orientation, a relative phase shift between cells is sufficient to remove the correlation between them. The results from simulations in the flat box environment point at the same phenomenon, with in fact most pairs of grid units ending up negatively correlated, as shown in Figure 4.5 top. Away from six-fold symmetry, however, things are a bit different. In the sphere, units can form five-fold symmetric grid patterns, when they have 12 fields, fields which *cannot* be translated on top of each other, because translations do not exist on curved surfaces. So the bulk of the units are less anti-correlated, and the peak correlation shifts to less negative. In the burrow, without regular grid patterns, map correlations show a peak located at even higher values, near zero.

Both in the box and sphere environments, the correlation between *some* units reaches to almost 1, while most pairs of units are actually anti-correlated. The distribution is much less spread out in the burrow environment where, as we said (Figure 4.5 top), most pairs of units have correlation close to zero, and the most correlated ones hardly reach above 0.6 spatial (Pearson) correlation. Despite this, the examples in Figure 4.5 bottom show that a standard K-means algorithm identifies 6 clusters of units in the burrow data, with the same or even greater ease than in the box or sphere data. It appears that the reason is that in the sphere, and even more in the box, different units map out with their fields a low-dimensional spatial continuum, so

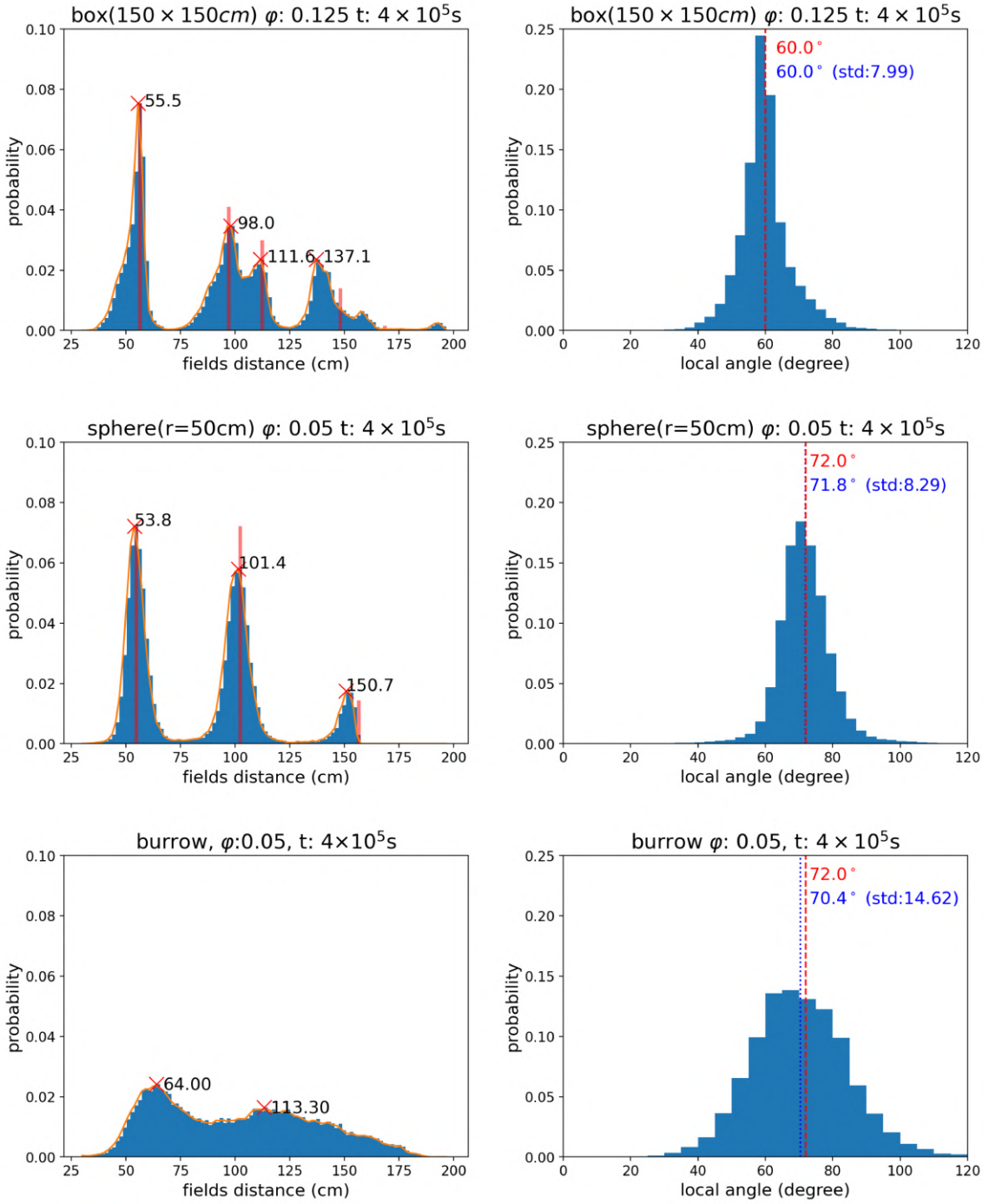

Figure 4.4: Inter field distance and angles from local triangles. Left column, distribution of inter field distance in box, spherical and burrow environments. Shown in red for the box and sphere is the distribution valid for regular grids, with the first peak aligned with that in our simulations. All peaks are indicated. Right column, the angle distribution, where again the red dotted curve refers to regular grids; the blue indicates simulation data, with standard deviation are annotated.

that breaking them into clusters is quite arbitrary – an intuitive example would be that of grid units with fields equi-spaced on a 1D ring, that would themselves describe a ring if randomly spread out, and not a clustered structure. In the multi-chamber environment of the simplified burrow, clusters apparently emerge spontaneously (see Figure 4.5 bottom).

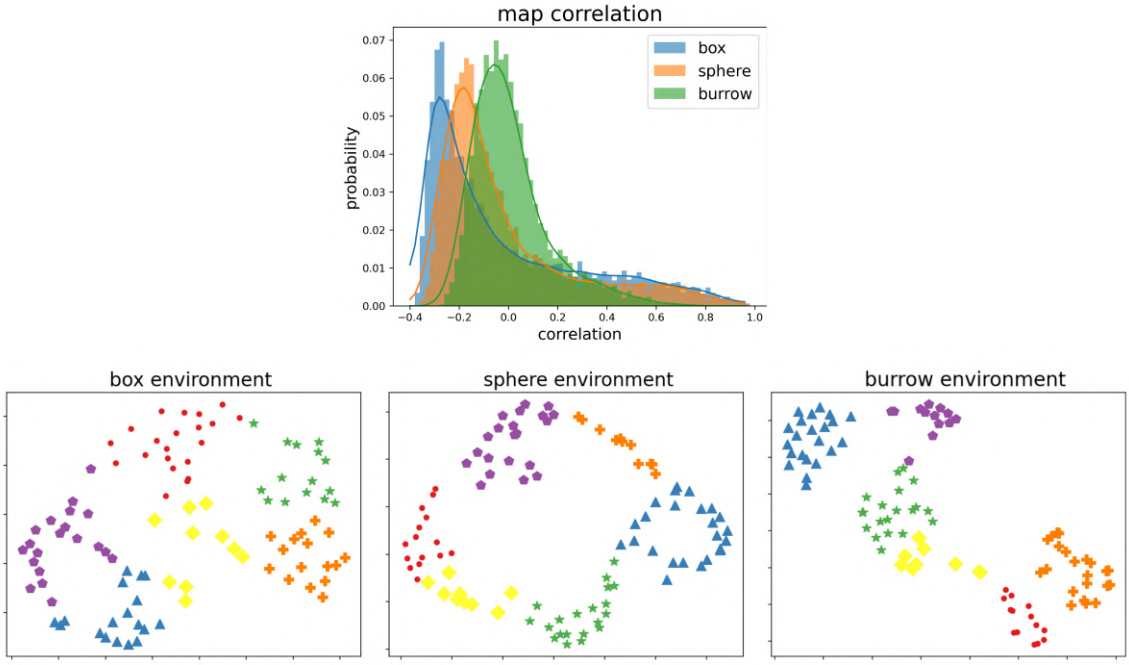

Figure 4.5: Top, map correlation between pairs of simulated units, in different environments. What is shown is the distribution of Pearson correlation values across pairs. Bottom, map clusters visualized with t-Distributed Stochastic Neighbor Embedding method (TSNE). The map distance between pair of units is defined by 1 minus their Pearson correlation, and units were clustered with a K-means algorithm into 6 clusters.

Local recurrent connections have been identified as a key element of grid pattern formation (Couey et al., 2013), in particular to align the grids in a flat environment (Si, Treves, 2013; D'Albis, Kempter, 2020; Tukker et al., 2021). We asked how the strength of recurrent connections affects the pattern formation process in our model environments. We simulated the adaptation model in flat and curved environments, and took the standard deviation of the angles from local triangles as a measure of the regularity of the grid pattern.

Considering two flat environments, a square box and a trapezoid with the same area, grid patterns show minimal standard deviation in the square box when the strength of recurrent connections takes a specific value $\varphi = 0.14$, as shown in Figure

4.6; and a larger minimum value (Figure 4.6) for somewhat weaker recurrent connections ($\varphi = 0.12$) in the trapezoid, known to distort the grid pattern of real cells (Krupic et al., 2015).

In the sphere, however, the minimum standard deviation, comparable with that in the box environment (as both allow for regular tessellation, five-fold in one case and six-fold in the other), is reached with much weaker recurrent connections, $\varphi = 0.05$, as shown in Figure 4.6. In even the simplified burrow, the standard deviation of the angle distribution is inherently higher, because of the lack of long-range order even in the absence of recurrent connections, and recurrent connections are bound to increase the irregularity further (see Figure 4.4 lower left).

In general, the strength of the recurrent connections might contribute to the rigidity of the grid pattern across environments, but also perhaps to its flexibility in the interaction with walls (Barry et al., 2007), changes in the boundary (Wernle et al., 2017) and the appearance of local cues (Ismakov et al., 2017), including goals (Boccara et al., 2019).

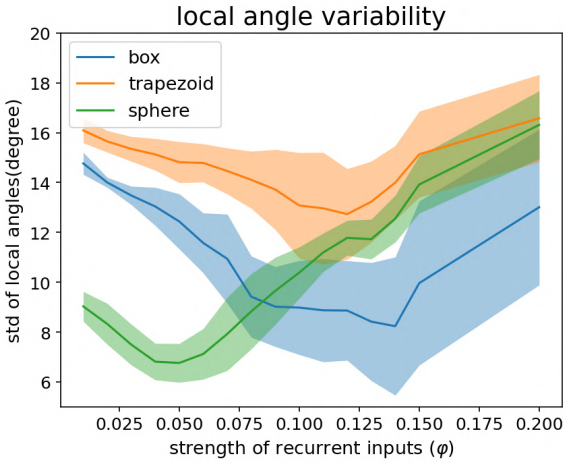

Figure 4.6: Standard deviation in local angles for the square box, trapezoid, and sphere environments varying the strength of recurrent connections. The square box environment is $150cm \times 150cm$, while the trapezoid has parallel walls $87cm$ and $174cm$ long, with symmetric $179.4cm$ side walls. The sphere has a $50cm$ radius, suited to include 12 fields per unit. The solid line is the mean value of the standard deviation, the shaded regions indicate its own standard deviation.

4.4 Discussion

The structure of the natural habitat of any species would appear to be a prime determinant of exactly how that species has adapted to live in that habitat; yet in

exploring the spatial memory and navigation abilities in rodents, and in particular the neural systems that subserve them, early experiments have focused on artificial laboratory environments, incongruent with those prevailing in the wild. The discovery of the remarkable spatial selectivity of grid cells, evident in such laboratory set-ups, has raised the issue of what grid cell firing patterns would look like, in an ecological setting.

More recent experiments have pointed at increased irregularity and plasticity of grid activity patterns, whether due to large environments (Stensola et al., 2015), non-standard shapes (Krupic et al., 2015), modulation by local cues (Ismakov et al., 2017), boundary changes (Wernle et al., 2017) or the presence of goals (Boccara et al., 2019). These observations, however, were largely framed as deviations or perturbations from the ideal notion of a regular tessellation of the environment, exhibiting long-range order *ad infinitum*, which had been evoked by the early findings.

The possibility that long-range order may not apply at all in an ecological setting was raised initially by looking at the activation patterns that emerge, with the adaptation model, in 3D (Stella, Treves, 2015) or on curved 2D surfaces (Stella et al., 2013; Urdapilleta et al., 2015), and is confirmed in a long-running experimental study in bats (Ginosar et al., 2021). While bats fly, rats are burrowing animals, and natural burrows are much more complicate structures than open arenas or other schematic laboratory settings.

In the present study, we have modeled the burrow environment based on the detailed quantitative descriptions by John Calhoun, and we have let a virtual rat randomly explore it; then using our self-organizing adaptation model we have observed grid pattern formation in model units. Grid units can attain stable representation of the whole environment, if acquiring it slowly, but less explored sub environments tend to be represented by blurred maps. The limited size of the chambers in natural burrows only allows grid units to express very few fields, challenging the very idea that grid cells may show long-range order outside the lab. One may wonder whether the reports of a six-fold symmetry in imaging data from humans, a putative signature of an underlying grid-like representation, might be due to large virtual arenas used in those studies (Doeller et al., 2010). It comes as no surprise, then, that the characteristic signature was not observed in the limited and non-flat vowel space (Kaya et al., 2020), although of course there may be many other reasons for a null result.

The continuity of spatial representations depends on the exploration. In (Carpenter et al., 2015), with a multi-compartment environment, real grid cells firing patterns could establish a single, continuous representation that spanned both compartments

after prolonged experience. In natural burrows however, tunnels are so narrow that they are effectively 1D structures, and as such they necessarily break any potential continuity in the representation of the chambers. What is left, at least when studied with the adaptation model, is effectively a representation in terms of disjoint spatial *fragments*, which coincide, in our modelling framework, with the better explored chambers.

The fragmentary nature of these spatial representations finds expression also at the level of neural populations. Compared with simulations in regular environments (in the square box, but also to some extent in the large hemi-sphere which can accommodate 6 fields), grid units simulated in burrows have more of a tendency to cluster in groups with similar fields. This might be part of the drive that leads to the observed *modularity* of grid activity (Stensola et al., 2012; Urdapilleta et al., 2017).

In flat environments recurrent connections promote regularity (and can align out-of-spatial-phase patterns). In simple environments with constant non-zero curvature, recurrent connections promote irregularity (Stella et al., 2020). In real-life environments, it is likely that they cause both irregularity and clustering into groups of units with similar selectivity, running against the principle of representing space evenly, expressed in the most idealized conceptual model by the notion of a continuous attractor.

Experiments in artificial laboratory settings, which utilize well-controlled and simplified paradigms, thus gave us the opportunity to admire a most impressive feat of the rodent nervous system, its ability to approximate a regular tiling of an infinite plane. While an exhilarating experience, this may have distracted us from understanding the characteristics of grid cells in ecological conditions, and possibly their function in an evolutionary perspective.

Chapter 5

Biased sampling and grid pattern distortion

5.1 Introduction

Grid cells, a crucial type of cell for spatial representation, provide capabilities that may increase animals' accuracy on depicting their surrounding environment by firing in multiple fields arranged in a highly organized hexagonal pattern (Fyhn et al., 2004; Hafting et al., 2005). This remarkably regular pattern was previously believed to be unaffected by the shape of the environment, leading to theories about the potential of grid cells as a universal and unchanging metric for representing spatial information (Fuhs, Touretzky, 2006; Fiete et al., 2008; Burgess, 2008).

Recent studies have provided insights into the impact of environmental features on the formation of grid cell patterns, affecting their spacing, alignment, and symmetry (Barry et al., 2007; Krupic et al., 2014, 2015; Stensola et al., 2015; Krupic et al., 2018; Boccara et al., 2019; Bellmund et al., 2020). These phenomena can be broadly categorized into two major components: anchoring to the environment and pattern distortion.

Anchoring to the environment involves connecting the spatial representation to specific local features, such as a goal (Boccara et al., 2019), or to the boundary (Stensola et al., 2015; Julian et al., 2018). Regarding the anchoring to the boundary, the analysis of grid cells recorded in square recording environments has shown that the orientation of the grid axes is not randomly distributed (Stensola et al., 2015; Julian et al., 2018). Instead, within each module of grid cells, the orientation of the grid axes tends to cluster around the cardinal axes, indicating alignment with the geometric features of the environment. Moreover, the distribution of minimal angular

deviation from the walls across the cell population shows a distinct unimodal peak centered at 7.5 degrees.

Grid pattern distortion can be induced by the shape of environments, primarily due to the influence of environmental boundaries and geometry on the spatial representation of grid cells (Krupic et al., 2014, 2015, 2018). In irregularly shaped environments, such as trapezoids or other non-rectangular geometries, the grid pattern becomes distorted, leading to alterations in the spacing, orientation, alignment and symmetry of grid fields.

These deviations in grid patterns could potentially be explained by the patterns of environment exploration.

During cognitive tasks, such as spatial exploration, animals demonstrate highly structured behavior, with spatio-temporal patterns recurring across their actions (Donnarumma et al., 2021). These behavioral patterns or motifs can reveal essential latent dimensions related to how animals interact with the external world.

In this chapter, we will begin by investigating how rats sample their environment through an analysis of their exploration behavior patterns. Subsequently, we will simulate the trajectory patterns of a virtual rat exploring a square box environment, utilizing the insights gained from these observations. Next, employing a self-organizing network model as described in (Kropff, Treves, 2008; Si, Treves, 2013), we will simulate the formation of grid patterns based on the trajectory simulations. By analyzing the orientation of the grid axes in these patterns, we have identified a trend in the change of anchoring angles relative to different exploration behaviors.

Additionally, we hypothesize that long-range correlation might partially account for the grid pattern distortion observed in irregularly shaped environments. We examined this hypothesis through the exploration pattern, which entails reducing the frequency of changes in running direction.

5.2 Network model for grid pattern formation

To simulate the formation of grid maps from disorderly encoding patterns under the influence of firing rate adaptation, a two-layer network was constructed.

The first layer of the network is composed of place units, each of which contains a single place field randomly scattered throughout the environment. The fields are distributed beyond the border to mitigate any border effects that may arise from the distribution of place cells. This layer supplies explicit location information to the subsequent layer.

The firing rate of a place unit i which has its field centered at position $\vec{x}_{i0}$ when rat is located at $\vec{x}_t$ is

$$r_i^t = \exp\left(-\frac{||\vec{x}_t - \vec{x}_{i0}||^2}{2\sigma_p^2}\right) \tag{5.1}$$

where $\sigma_p = 5cm$ is the radius of the place fields.

The second layer of the network is composed of mEC units which are expected to develop grid-like firing patterns from an initial random firing pattern. Each mEC unit receives input from the initial layer, as well as collateral connections from other mEC units. The input for mEC unit j at time t is denoted by h_j^t,

$$h_j^t = \sum_i W_{ij}^{t-1} r_i^t + \rho_1 \sum_k W_{jk}^{t-1} \psi_k^{t-\tau} \tag{5.2}$$

where W_{ij} is the weight from place unit i to mEC unit j, $\psi_k^{t-\tau}$ is the activity of mEC unit k which have been reverberated by collateral connections W_{jk}^t with a delay $\tau = 25$ steps. $\rho_1 = 0.1$ here is a strength of inter layer connections.

The firing rate ψ_j^t of mEC unit j is determined through a threshold-nonlinear transfer function

$$\psi_j^t = \psi_{sat} \arctan[g^t(\alpha_j^t - \mu^t)]\Theta(\alpha_j^t - \mu^t) \tag{5.3}$$

where $\psi_{sat} = 2/\pi$ normalizes the firing rate into arbitrary units. $\Theta(\cdot)$ is the Heaviside function which equals zero when negative. The variable μ^t is a threshold while α_i^t represents a time-integration of the input h_j, which adapted by the dynamical threshold β_j

$$\begin{aligned} \alpha_j^t &= \alpha_j^{t-1} + b_1(h_j^{t-1} - \beta_j^{t-1} - \alpha_j^{t-1}), \\ \beta_j^t &= \beta_j^{t-1} + b_2(h_j^{t-1} - \beta_j^{t-1}) \end{aligned} \tag{5.4}$$

where β_j has slower dynamics than α_j, and b_2 is set to $b_2 = b_1/3$, $b_1 = 0.1$. The adaptive dynamics referred to here make it more challenging for a MEC neuron to maintain its firing over an extended period, thus giving rise to fatigue dynamics in MEC units (Kropff, Treves, 2008). The gain g^t and threshold μ^t are iteratively adjusted at every time step to fit the mean activity $a = \sum_j \psi_j^t/N$ and the sparsity $s = (\sum_j \psi_j^t)^2/(N \sum_j \psi_j^{t\,2})$ within a 10% relative error bound from pre-specified values, here $a_0 = 0.1$ and $s_0 = 0.3$ respectively.

As the virtual rat explores the environment, all weights in the network undergo self-organization and are updated according to the Hebbian rule.

Weights between the first layer unit i and the second layer unit j are modified according to

$$\Delta W_{ij}^t = \epsilon(\psi_j^t r_i^t - \bar{\psi}_j^{t-1} \bar{r}_i^{t-1}) \tag{5.5}$$

where $\epsilon = 5 \times 10^{-3}$ is a positive learning rate. $\bar{\psi}_i^t$ and $\bar{r}_j^t$ are estimated mean firing rates and updating as follow,

$$\begin{aligned} \bar{\psi}_i^t &= \bar{\psi}_i^{t-1} + \eta(\psi_i^t - \bar{\psi}_i^{t-1}), \\ \bar{r}_i^t &= \bar{r}_i^{t-1} + \eta(r_i^t - \bar{r}_i^{t-1}), \end{aligned} \tag{5.6}$$

and $\eta = 0.05$ is a positive averaging factor.

The collateral weights between second layer mEC units j and k are adapted according to

$$\Delta W_{ik}^t = \zeta \psi_i^t (\psi_k^{t-\tau} - \kappa) \tag{5.7}$$

where $\zeta = 6.6 \times 10^{-5}$ is a learning rate much smaller than the learning rate ϵ with feed-forward weights between first layer place units and second layer mEC units. $\kappa = 0.1$ is an inhibition factor.

All the weights in the network are initialized as random numbers $(1 - \gamma) + \gamma u$. $\gamma = 0.1$, and u is a random variable uniformly distributed in $[0, 1]$.

After initialization or weight updates, all weights in the network are normalized to have a unit L_2 norm,

$$\sum_j {W_{ij}^t}^2 = 1 \tag{5.8}$$

5.3 Behavior of rats around border area

Through the analysis of behavior data from rats exploring square enclosures, we have observed several exploration patterns. Rats tend to move at a slower speed in the direction perpendicular to the walls but move faster along the walls. Furthermore, when running close to the walls, rats exhibit a preference for either clockwise or counterclockwise running along the walls.

Building upon the analysis of rat exploration behavior, we conducted a study to model the trajectory patterns of exploration. To simulate the behavior data, we developed a virtual rat tasked with exploring a 200 by 200 cm^2 square environment. At each time step, the virtual rat's running direction was subject to a random perturbation. The magnitude of this perturbation was determined by drawing from a generalized Gaussian distribution, tailored to fit the observed rat behavior data discussed above.

$$p(d) = \frac{\beta}{2\alpha\Gamma(1/\beta)} \exp((-\frac{|d|}{\alpha})^\beta) \tag{5.9}$$

where $\alpha = 0.04$ and $\beta = 0.6$ are chosen to match the real rat data. Γ denotes the gamma function, $\Gamma(n) = \int_0^\infty x^{(n-1)}e^{(-x)}dx$.

To accommodate the observed rat behavior of moving more slowly when perpendicular to the walls in the border region, we incorporated a potential function, denoted as u. This potential function u is designed in a way that its negative gradient generates a repelling force, which reduces the virtual rat's speed as it approaches the wall.

$$u(x, y) = A[\mu(r(x)) + \mu(r(y))] \tag{5.10}$$

$$\mu(r) = \begin{cases} exp(\frac{(r-r_0)^2}{2\sigma^2}) - 1 & if r < r_0 \\ 0 & otherwise \end{cases} \tag{5.11}$$

where $r_0 = 20cm$, which specifies the border region. The function u becomes zero beyond this distance. The distance to the closest wall in the x direction is given by $r(x) = \min(x - x_{min}, x_{max} - x)$, where $[x_{min}, x_{max}] = [-100cm, 100cm]$ denotes the range of positions in the x direction. This applies to the y direction. The magnitude of the potential function is $A = 100 \exp(-\frac{r_0^2}{2\sigma^2})$ in the absence of further specifications, where $\sigma = 3cm$ represents the width of the potential function.

The intended velocity components of the rat as adapted from the description above described as below,

$$\begin{aligned} \widetilde{v}_{x,t} &= v_{t-1}cos(\omega_t) - f_x(x_t) + \phi\theta(x_t) \\ \widetilde{v}_{y,t} &= v_{t-1}sin(\omega_t) - f_y(y_t) + \phi\theta(y_t) \end{aligned} \tag{5.12}$$

Here, v denotes the speed of the rat. The gradients of u are given by $f_x(x) = \frac{\partial u(x,y)}{\partial x}$ and $f_y(y) = \frac{\partial u(x,y)}{\partial y}$. In the border area, $|\theta(x)| = r_0 - r(x)$, where the value is positive or negative, depending on which border the rat is near. This provides a trend for the rat's clockwise or counterclockwise running preference. The same applies to $\theta(y_t)$.

To address the constraint of the rat moving faster along the wall, we make further adjustments to its velocity, as outlined below.

$$\begin{aligned} v_{x,t} &= \widetilde{v}_{x,t} + \epsilon[a_x(x_{t-1}, y_{t-1})vcos(\widetilde{\omega}_t) - \widetilde{v}_{x,t}] \\ v_{y,t} &= \widetilde{v}_{y,t} + \epsilon[a_y(x_{t-1}, y_{t-1})vsin(\widetilde{\omega}_t) - \widetilde{v}_{y,t}] \end{aligned} \tag{5.13}$$

where $v = 40cm/s$ is the mean speed in the center of the environment. The intended running direction is given by $\widetilde{\omega}_t = arctan(\frac{\widetilde{v}_{y,t}}{\widetilde{v}_{x,t}})$. $\epsilon = 0.1$ is an averaging

constant. The $a_x(x_{t-1}, y_{t-1})$ and $a_y(x_{t-1}, y_{t-1})$ are defined as below,

$$a_x(x,y) = \begin{cases} \frac{1+\alpha*sign(v_y)*(y_{max}-y)/r_0}{1+\psi*r_x/r_0} & if r_y < r_0, r_y < r_x \\ 1 & otherwise \end{cases}$$
$$a_y(x,y) = \begin{cases} \frac{1+\alpha*sign(v_x)*(x_{max}-x)/r_0}{1+\psi*r_y/r_0} & if r_x < r_0, r_x < r_y \\ 1 & otherwise \end{cases} \tag{5.14}$$

The velocity $v_t = \sqrt{v_{x,t}^2 + v_{y,t}^2}$ and the new position (x_t, y_t) can be calculated from above. In Figure 5.1, we compared the velocity patterns of actual rats and simulated virtual rats.

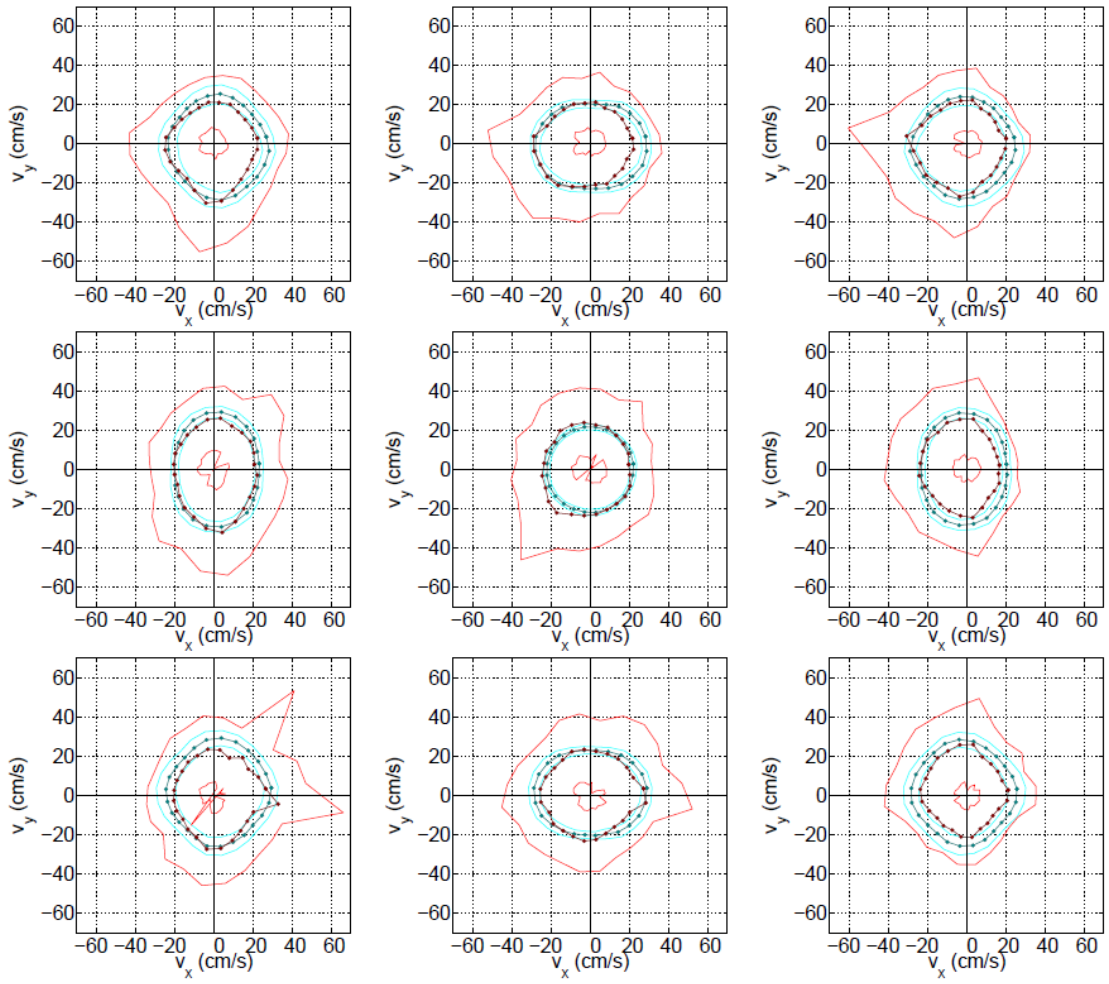

Figure 5.1: Velocity comparison with real rats and simulated rats. The comparison between the velocity of the simulated (in cyan) and the real rat (in red). The lines with markers are the mean speed, and the lighter lines show the ± standard deviations.

Based on the analysis above, the parameters ϕ in equation 5.12 and ψ from equation 5.14 play a critical role in shaping the virtual rat's trajectories. Specifically, the

parameter ϕ determines the strength of the directional bias, leading to either clockwise or counterclockwise running along the border, while ψ determines the degree of speed anisotropy in the border region.

5.4 Simulation results of the grid pattern boundary anchoring

5.4.1 Simulated trajectory analysis

In the analysis here, we examined the properties of simulated trajectories under different parameter values. Figure 5.2 illustrates a comparison of simulated trajectories in the border area for various values of ϕ and ψ. We focused on three key factors: 1) the time spent in the border relative to the center area, 2) the speed difference between the border and center areas, and 3) the preference for running direction in the border area (for simplicity, we only considered counterclockwise running). As ϕ and ψ increase, the simulated rats spend more time in the border area and exhibit higher velocities along the border. The speed anisotropy has no effect on the direction preference in the border area.

5.4.2 Grid pattern anchoring to the boundary

One hundred simulations were conducted for each combination of ϕ and ψ, each simulation consists of 200 mEC units. Simulations that failed to form coherent grid patterns were discarded (the standard deviation of the angle from the wall larger than 2 degrees). Across the range of ϕ and ψ values analyzed, we observed that the mEC units tended to form grid patterns with gridness high enough for further analysis. Examples of grid patterns from different simulations are shown in Figure 5.3.

To identify the grid axis of the mEC units, we employed the same method described in the paper by Stensola et al. (2015). Specifically, we analyzed the autocorrelation map for each grid map, from each the inner six fields were identified to obtain the axis. We used this axis as a reference for calculating the smallest angle between the grid axis and the wall for each mEC unit. The right column in Figure 5.3 presents the distribution of angles from the wall from all the simulations after discarded the simulations with standard deviation of the angle from the wall larger than 2 degrees.

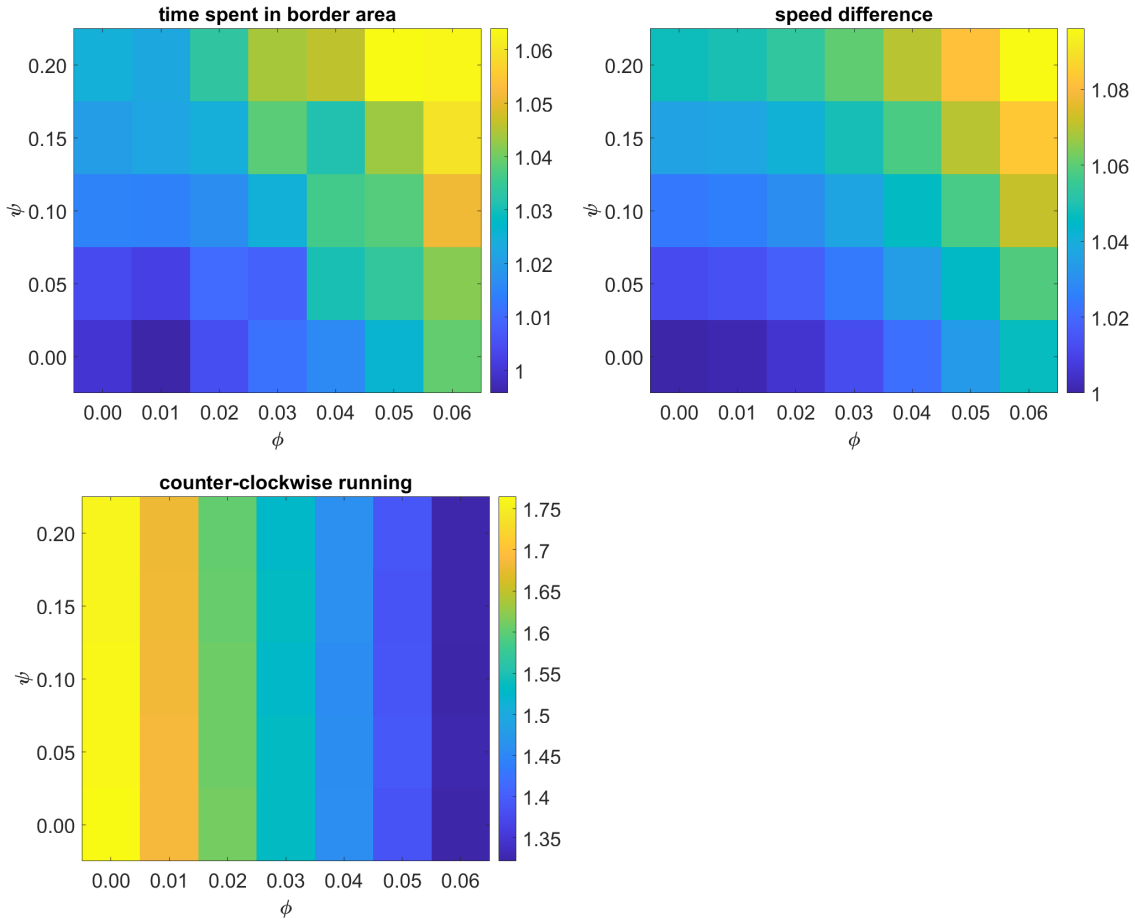

Figure 5.2: Simulated trajectories analysis. The first row left side of the figure displays the ratio of time spent in the border area relative to the time spent in the center area. We calculated this ratio by dividing the total time spent per unit area in the border region by the total time spent per unit area in the central area. Since we introduced a repelling force near the borders to simulate the observed behavior of rats running slower when perpendicular to the walls, the time simulated rats spent in the border area decreased. To account for this effect, we normalized these values under different conditions by dividing each value by the value obtained when $\phi = 0$ and $\psi = 0$. In the first row right, the ratio of speed in the border area is calculated using the same method as the time spent in the border area. In the second row left side, we measured the mean direction difference of the rat's running direction with the closest wall.

5.4.3 Boundary alignment

Results about how the grid pattern anchored to the boundary were shown in Figure 5.4.

In the absence of speed anisotropy ($\psi = 0.00$), as the preference for counter-clockwise running increases, there is a corresponding shift in the angles of the grid

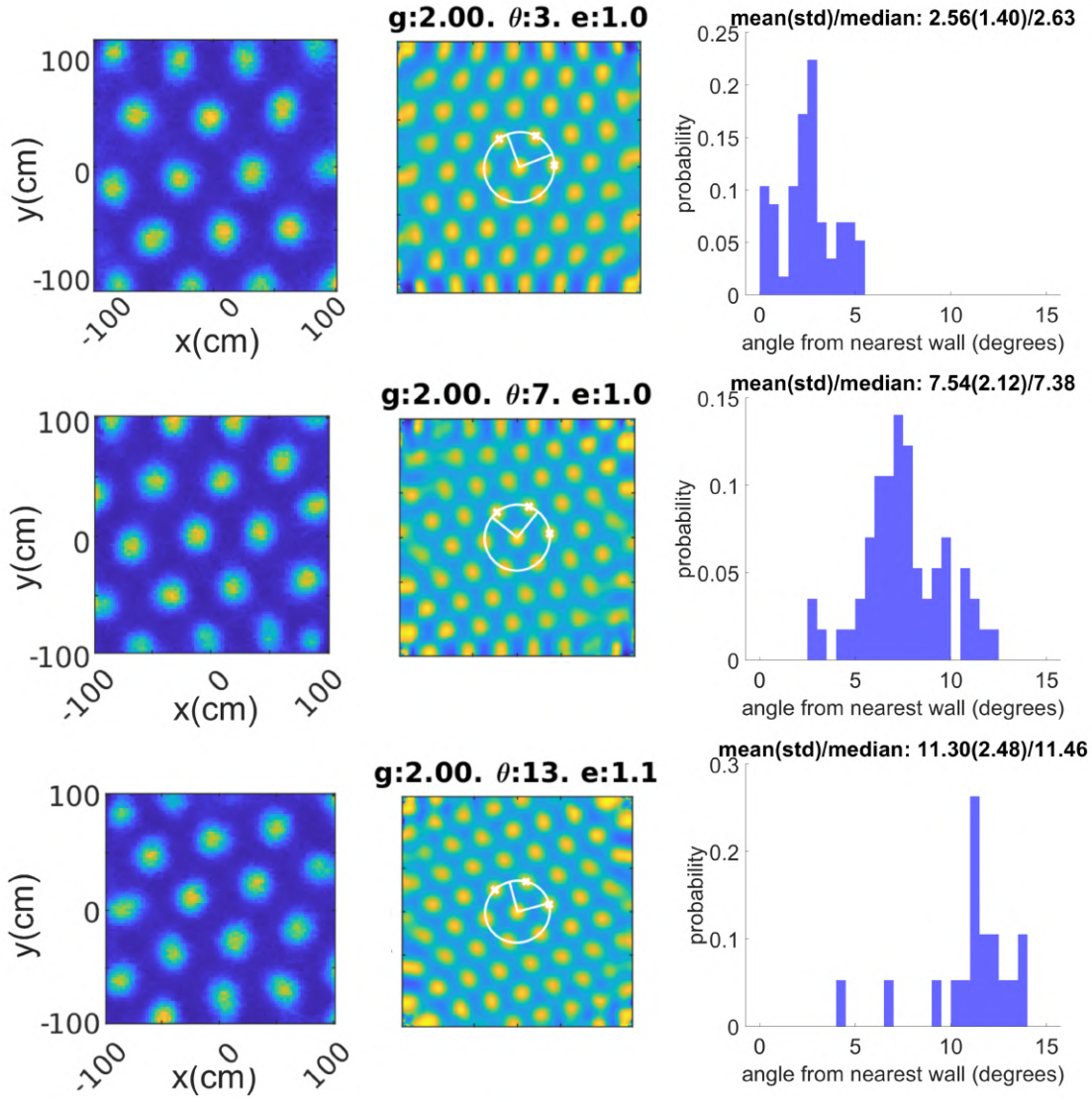

Figure 5.3: Example of simulated mEC units with different grid axis preference. The results shown in the first row were obtained when $\phi = 0$ and $\psi = 0$. The left column shows the rate map of an example single unit. The center column shows the corresponding auto-correlation map. The gridness, which ranges from 0 to 2, as well as the angle from the wall in degrees and ellipse ratio are indicated on top. The right column shows the distribution of angles from the wall from all the simulations after discarded the simulations with standard deviation of the angle from the wall larger than 2 degrees. The second row of the figure shows the results when $\phi = 0.04$ and $\psi = 0.10$, while the third row shows results when $\phi = 0.04$ and $\psi = 0.20$.

axis away from the wall from 4.26±4.11 degrees (when $\phi = 0.00$) to 2.56±1.40 degrees (when $\phi = 0.04$). Notably, the standard deviation of the anchor angle decreased from 4.11 degrees to 1.40 degrees. This reduction in variability suggests that the grid patterns become more consistent across different trials. One possible explanation for

this effect is an increase in the biased sampling of the border area, which leads to greater coordination of the grid patterns with the boundary cues.

As ψ increased to 0.10, we also observed a decrease in the standard deviation of the angles of the grid axis from the wall, from 3.50 degrees to 2.12 degrees, as ϕ increased from 0.00 to 0.04. The angle away from the wall changed from 3.35 ± 3.50 degrees (when ϕ was 0.00) to 7.54 ± 2.12 degrees (when ϕ was 0.04). These results indicate that as the preference for running along the wall increases, the alignment of the grid cells with the wall becomes more consistent and less variable across different trials.

When ψ reached 0.20, the angles of the grid axis from the wall ranged from 4.17 ± 3.96 to 11.30 ± 2.48, covering almost the entire range of 0 to 15 degrees.

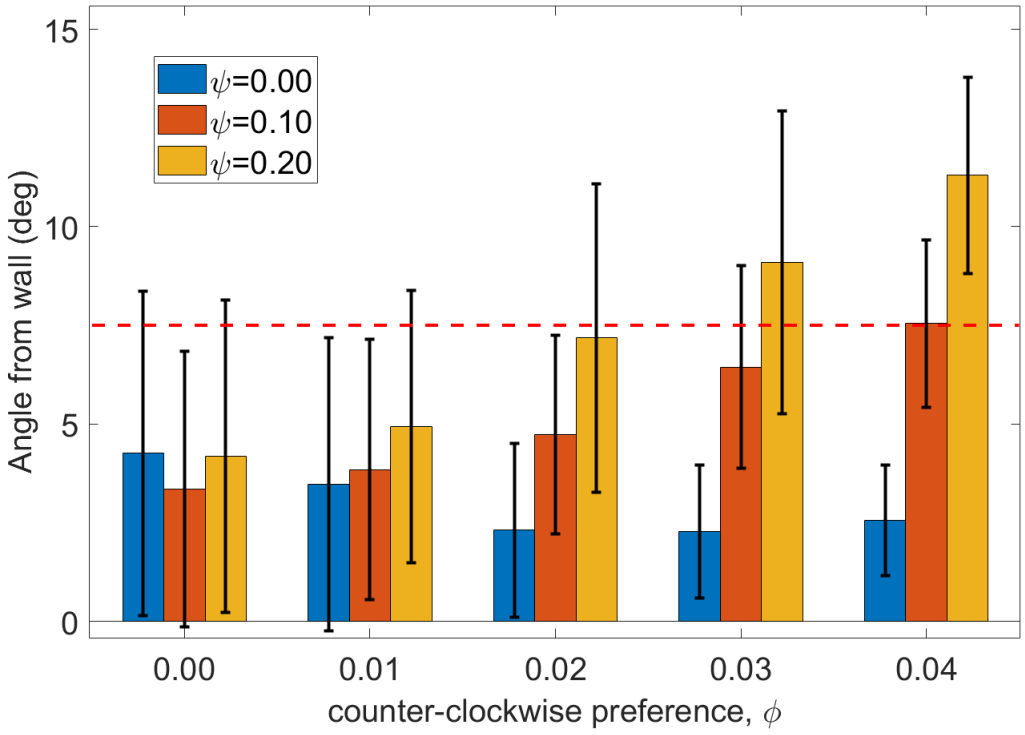

Figure 5.4: Boundary alignment of the grid patterns.

5.4.4 Elliptic deformation

According to experimental data from Stensola et al. (2015), the angle offset from the wall is consistently accompanied by an elliptic distortion of the grid pattern. This elliptic deformation is described as the deviation of the grid pattern from a circular shape, as observed in the inner six fields of the grid pattern.

In our simulation results, we also observed that grid patterns exhibit elliptic distortion. The correlation of ellipticity with the border running direction preference exploration and speed anisotropy are depicted in Figure 5.5 first and second rows. The ellipticity has a weak correlation coefficient with the angle from the wall, as illustrated in Figure 5.5 third row left, even when the angle from the wall is restricted to 6 to 9 degrees illustrated in Figure 5.5 third row right.

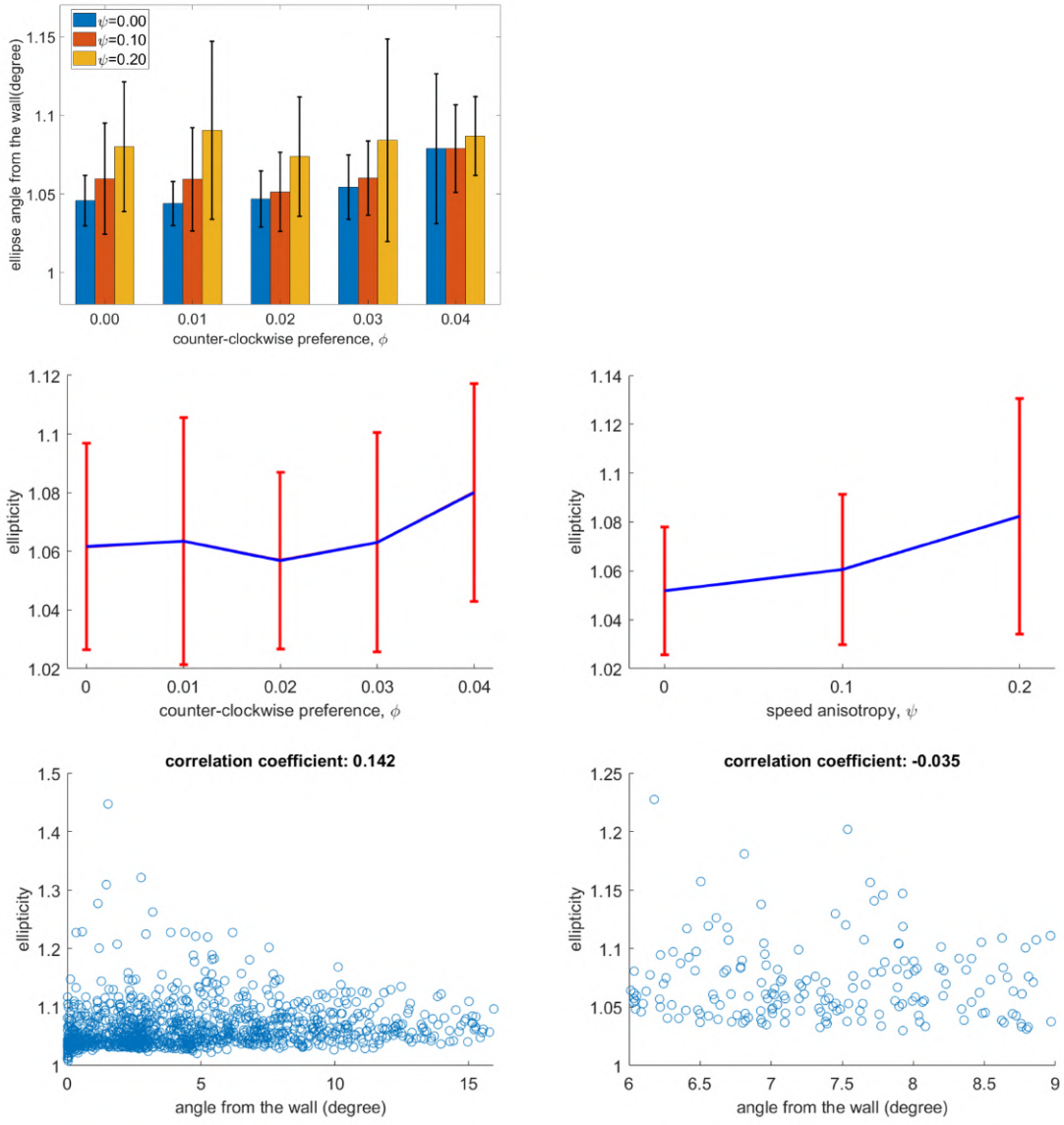

Figure 5.5: Ellipticity of grid patterns. Top and second rows, ellipticity changes with counter-clockwise preference running and speed anisotropy. Third row, a weak correlation between ellipticity and grid axis angle from the wall.

5.5 Environment geometry structure sampling

The sampling of environment geometry structure includes long-range correlations between environment structure cues. To investigate the impact of long-range correlation on the encoding pattern of grid cells, we initially reduced the direction changing of the virtual rat by keeping the direction unchanged for three consecutive steps during environment sampling. An example is depicted in Figure 5.6.

Subsequently, we incorporated a realistic animal foraging random walk, known as the Lévy flight foraging hypothesis, which exhibits exponential scaling of the step lengths (Bartumeus et al., 2005).

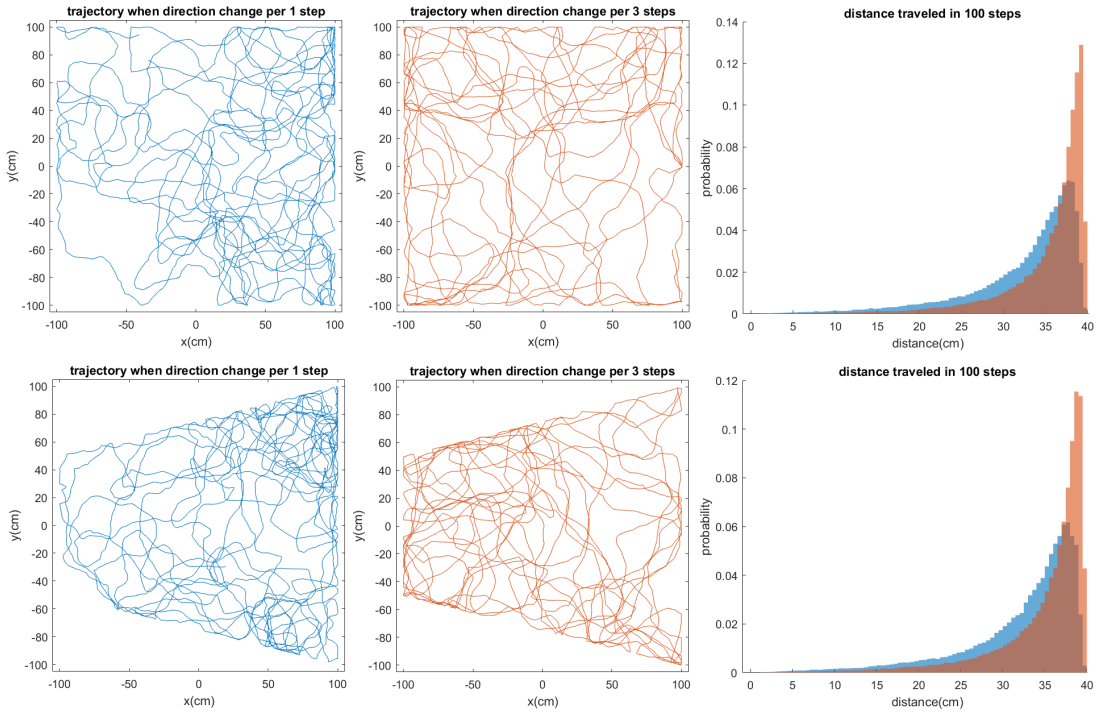

Figure 5.6: Trajectory comparison when direction changing been reduced. The first row depicts the square environment, while the second row shows the trapezoid environment. On the left side, the trajectory direction changes per one step, and in the middle, changes per three steps. On the right side, the distance traveled in 100 steps is presented for each type of environment.

Figure 5.6 demonstrates that reducing the frequency of direction changes increases the virtual rat's chances of traveling longer distances. As a consequence, there is a higher density of long-range correlations, which can be effectively captured by the self-organization model discussed earlier.

Then for the running directions, the standard deviation of local running directions

is shown in Figure 5.7. Reducing the frequency of changes in running direction makes it easier to follow a consistent running path around the corners.

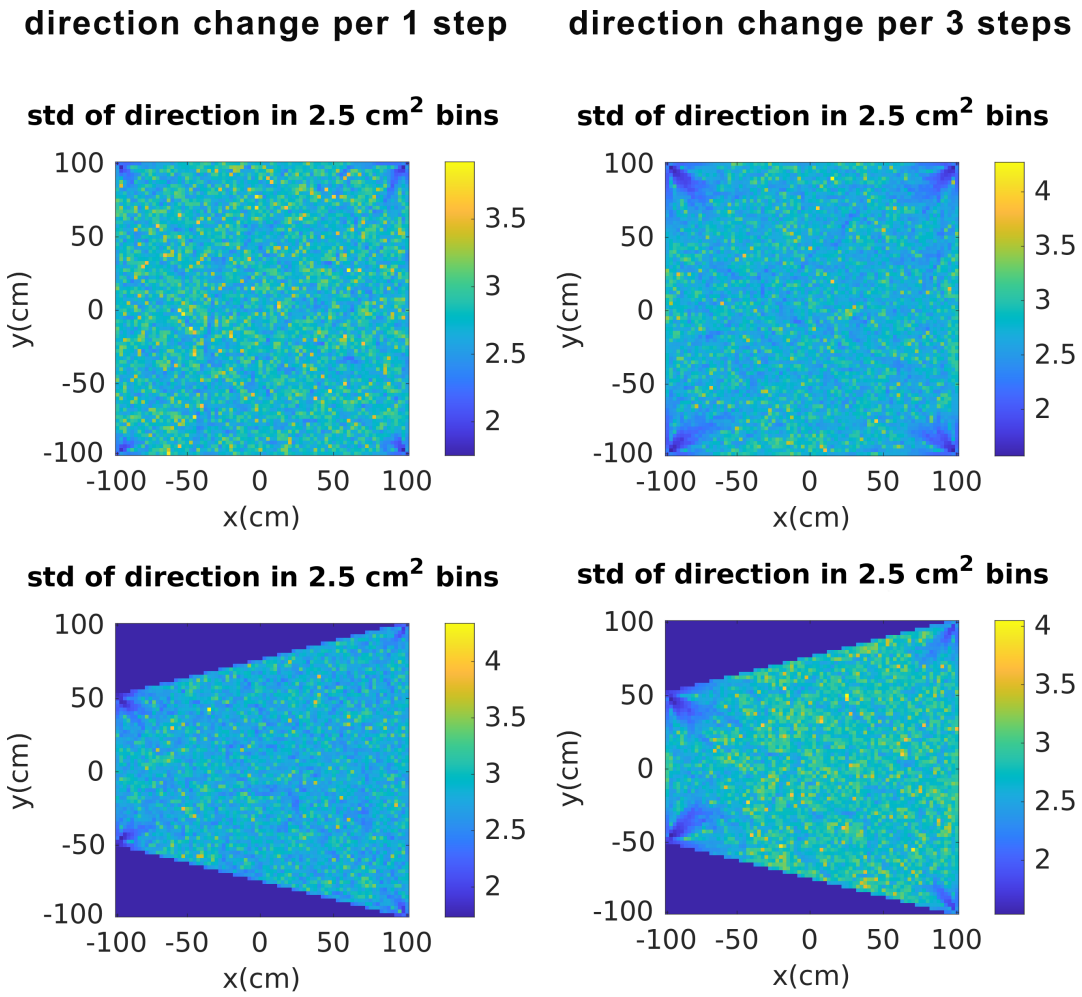

Figure 5.7: Standard deviation of local running directions. The left two plots are when the running direction changes every step, the right two plots are when the running direction changes every three steps.

By applying the environment exploration behavior described above to the self-organization model discussed earlier, we observed the emergence of grid patterns with distortion, as depicted in Figure 5.8 and Figure 5.9.

Figure 5.8 presents grid patterns when the direction changing is reduced to three steps, indicated by the red rectangle. The top two rows display three examples of grid pattern formation in a square environment. It is evident that reducing the number of direction changes to three steps does not significantly impact the regularity of the grid pattern in the square environment.

However, the lower two rows show three examples of grid pattern formation in a trapezoid environment. In this case, the regularity of the grid pattern decreases when the direction changing step is reduced to three, as observed in the trapezoid environment.

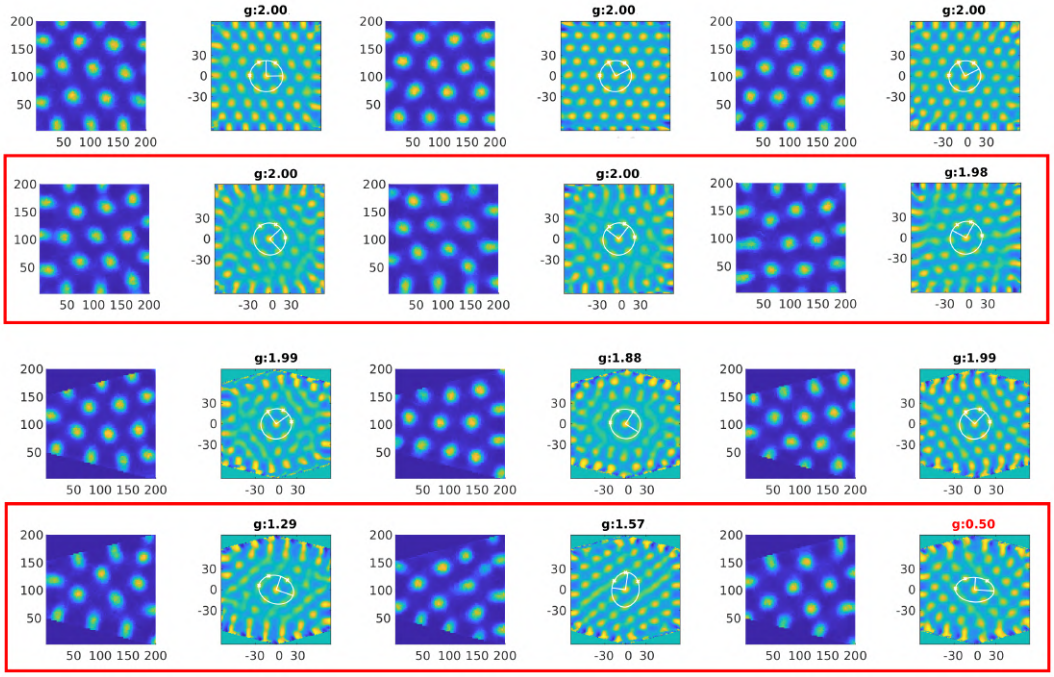

Figure 5.8: Regularity decreases when the direction remains unchanged for three steps. The top two rows represent a square environment, while the lower two rows represent a trapezoid environment. The maps framed by a rectangle depict the results obtained when the direction is held constant for three steps.

In Figure 5.8 (a), the gridness in the square environment decreases from 1.96 ± 0.14 to 1.74 ± 0.44 when each direction is held for three steps. However, in the trapezoid environment, the gridness decreases from 1.88 ± 0.34 to 1.47 ± 0.63.

To incorporate more realistic trajectories, we implemented Lévy flight foraging, which exhibits exponential scaling of the step lengths (Bartumeus et al., 2005). In this approach, the step length per direction follows $p(length) = \exp^{-\mu}$. When applying this method to the square environment, the gridness reduced from 1.97 ± 0.15 to 1.83 ± 0.35 as μ increased from 1 to 2. Similarly, in the trapezoid environment, the gridness decreased from 1.92 ± 0.28 to 1.71 ± 0.48 as μ increased from 1 to 2.

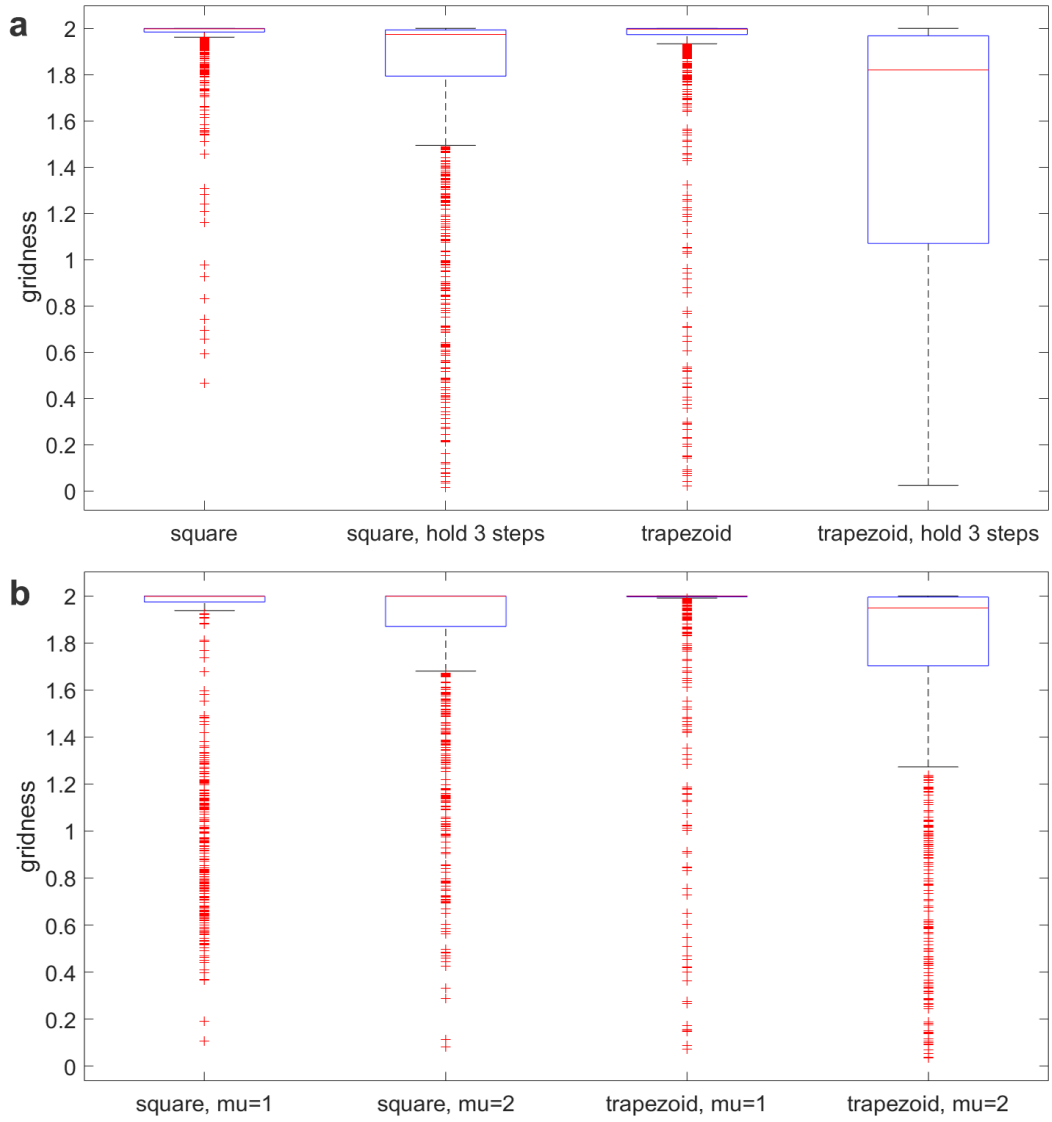

Figure 5.9: Gridness reducing when the direction remains unchanged for few steps. The top row of the figure illustrates the gridness when the direction is held for 1 or 3 steps, while the second row represents the gridness when the direction follows a Lévy flight random walk.

5.6 Discussion

The way our brain internally represents external spatial information depends on both internal and external factors such as the structural organization of the brain and the nature of the spatial information available in the environment.

Grid cells are a specific type of neuron located in the medial entorhinal cortex that displays spatially modulated firing patterns, forming a hexagonal grid that covers the

animal's environment. Unlike some other types of neurons, grid cells do not have an external corresponding information structure that could explain their encoding structure, indicating that their encoding structure may be generated endogenously.

Endogenously generated patterns possess the potential to be universal and invariant measures. Consequently, the grid cell patterns have sparked theories about their potential as a universal and invariant metric for representing spatial information (Fuhs, Touretzky, 2006; Fiete et al., 2008; Burgess, 2008).

Recent discoveries suggest that grid cells are not only involved in encoding global spatial information but also play a role in encoding local information. One notable observation regarding the anchoring of grid patterns to the environment is that the grid axis remains fixed at a 7.5-degree angle from the wall in a square space (Stensola et al., 2015; Julian et al., 2018).

By analyzing behavior data from rats exploring square enclosures, we have identified several exploration patterns. Rats tend to move at a slower speed when traveling in the direction perpendicular to the walls, but their speed increases when moving along the walls. Additionally, when running near the walls, rats exhibit a preference for either clockwise or counterclockwise movement along the walls.

We simulated a virtual rat, incorporating the exploration patterns discussed above, and used the self-organization model (Kropff, Treves, 2008; Si, Treves, 2013) to simulate the formation of grid patterns.

Upon making slight adjustments to the exploration pattern, we observed corresponding variations in the anchored grid patterns within the environment. These findings strongly support our hypothesis that the anchor pattern of grid cells is influenced by the behavioral patterns exhibited in the border area.

Furthermore, grid patterns suffer severe distortion in irregularly shaped environments (Krupic et al., 2014, 2015, 2018), such as trapezoids. By simply reducing the frequency of direction changes of the virtual rat to provide more long-range correlation to the self-organization model, the grid pattern exhibits environment shape-specific pattern distortion. Interestingly, this phenomenon still holds when employing a realistic foraging strategy known as Lévy flight.

The findings presented here suggest that the grid cell pattern is not solely determined by path integration information, which would result in a perfect hexagonal grid pattern. Instead, it also responds to biased sampling of local information and long-range correlations, potentially leading to anchoring or distortions in the grid pattern.

Chapter 6

Understand grid cell with variants

6.1 Introduction

The concept of "grid cells" was coined to describe a specific type of neuron found in the medial entorhinal cortex (mEC) of the brain (Fyhn et al., 2004; Hafting et al., 2005). These neurons exhibit a unique firing pattern in an environment that is characterized by firing fields that are evenly spaced and arranged in a hexagonal grid pattern. A prevailing perspective posits that the primary function of the grid is to establish a universal metric for space (Hafting et al., 2005; Moser, Moser, 2008; Fuhs, Touretzky, 2006; McNaughton et al., 2006).

The study of grid cells is a highly active and prominent research topic. Since their initial discovery, significant efforts have been dedicated to furthering our understanding of grid cells. It has become evident that these cells possess a range of fascinating properties that go beyond universal metrics (Stensola et al., 2012; Rowland et al., 2016). They do not strictly adhere to regularity but display some degree of deviation and variability (Barry et al., 2007; Derdikman et al., 2009; Krupic et al., 2014, 2015, 2018; Boccara et al., 2019; Gerlei et al., 2020; Ginosar et al., 2021; Grieves et al., 2021). These findings highlight the complexity and richness of functions grid cells may participate in, shedding light on the intricate workings of the brain's spatial processing system (Ginosar et al., 2023).

The accumulation of properties and discoveries associated with grid cells has resulted in disagreements and challenges when it comes to defining and comprehending the concept of "grid cells". During discussions about "grid cells," there is a higher likelihood of encountering divergent interpretations and mismatched concepts of what "grid cells" actually represent. Recent research from Marti et al. (2023) highlights the idea that even seemingly well-defined concepts can have quantifiable meaning varia-

tions. Continued and ongoing discussions regarding the definition and understanding of the concept of "grid cells" would be advantageous for advancing further research.

"Concepts" have definitions, which are statements or explanations of the meaning of a word or term. Definitions provide clarity and understanding of the intended use of the concept. They typically include information about the essential qualities, properties, or characteristics that define the term and differentiate it from other similar terms.

In this chapter, we explore the encoding properties of grid cells using a simplified self-organization model. We specifically focus on two key properties of grid cells: the number of encoding fields per grid cell and the emergence of regularity in their spatial firing patterns. Additionally, we discuss the potential functions that grid cells may play in the discussion.

6.2 Network model

To simplify the discussion, simplified self-organization models were utilized. In these simulations, a virtual rat explores a square environment measuring $150 \times 150 cm^2$ at a constant speed of $v = 40 cm/s$. Each time step in the simulation corresponds to $10 ms$ in real-time.

A two-layered network has been constructed to simulate the development of grid cell spatial firing patterns from initially disordered encoding patterns, with the influence of firing rate adaptation taken into account.

In this context, rather than referring to units in the network as place cells and grid cells, we characterize them as location-encoding units that represent various locations within the environment.

To simplify the discussion, each unit in the first layer has a Gaussian-like field that is randomly distributed throughout the environment. It is worth noting that while Gaussian-like fields are commonly used, they are not a requirement for location units in the first layer of the network (Kropff, Treves, 2008).

The first layer of the network provides explicit location information to the next layer. The firing rate of a location unit i at given time t which has its Gaussian-like field centered at position $\vec{x}_{i0}$ when rat is located at $\vec{x}_t$ is

$$r_i^t = \exp\left(-\frac{||\vec{x}_t - \vec{x}_{i0}||^2}{2\sigma_p^2}\right) \tag{6.1}$$

where $\sigma_p = 5 cm$ is the radius of the place fields.

The second layer is composed of adaptive units, they are all initialized with random firing patterns. Each adaptive unit j receives inputs from the first layer, inputs to this adaptive unit j at time t are given by h_j^t

$$h_j^t = \sum_i W_{ij}^{t-1} r_i^t \tag{6.2}$$

where W_{ij} is the weight from first layer location unit i to second layer adaptive unit j.

The firing rate ψ_j^t of adaptive unit j is determined through a threshold-nonlinear transfer function

$$\psi_j^t = \psi_{sat} \arctan[g^t(\omega_j^t - \mu^t)]\Theta(\omega_j^t - \mu^t) \tag{6.3}$$

where $\psi_{sat} = 2/\pi$ normalizes the firing rate into arbitrary units. $\Theta(\cdot)$ is the Heaviside function which equals 0 when the value is negative. The gain g^t and threshold μ^t are iteratively adjusted at every time step to fix the mean activity a and the sparsity s within a range of relative error bound from pre-specified values. The variable μ^t is a threshold.

$$a = \sum_j \frac{\psi_j^t}{N} \tag{6.4}$$

$$s = \frac{(\sum_j \psi_j^t)^2}{(N \sum_j \psi_j^{t2})} \tag{6.5}$$

In equation 6.3, depending on the specific context of the discussion, ω_j^t can be defined as h_j, α_j^t, β_j^t, or γ_j^t, which represent different types of manipulations applied to the inputs from the first layer.

$$\begin{aligned}
\gamma_j^t &= \gamma_j^{t-1} + \tau_3(h_j^{t-1} - \alpha_j^{t-1} - \beta_j^{t-1} - \gamma_j^{t-1}), \\
\beta_j^t &= \beta_j^{t-1} + \tau_2(h_j^{t-1} - \alpha_j^{t-1} - \beta_j^{t-1}), \\
\alpha_j^t &= \alpha_j^{t-1} + \tau_1(h_j^{t-1} - \alpha_j^{t-1})
\end{aligned} \tag{6.6}$$

where α_j^t is tracking the raw first layer inputs h_j^t with a slow dynamics. β_j^t is tracking the difference between h_j^t and α_j^t, γ_j^t is tracking the difference between h_j^t and $\alpha_j^t + \beta_j^t$.

Figure 6.1 illustrates an example of the different input manipulation dynamics over time when the input h^t is equal to 1. α^t gradually approaches the input h^t, while β^t increases when the difference between h^t and α^t exists and larger than β^t. Similarly to β^t, γ^t also increases but with a faster rate in the beginning when the difference exists and is larger than γ^t, and also drops more quickly as the difference

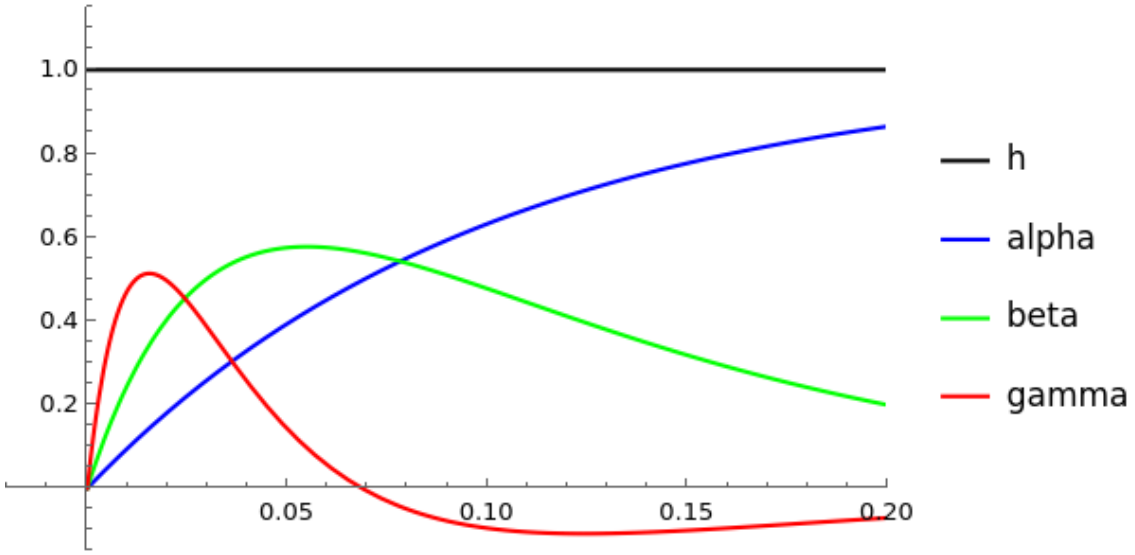

Figure 6.1: Inputs manipulation dynamics of α, β and γ. Here $\tau_1 = 0.10$, $\tau_2 = \tau_1/3$, $\tau_3 = \tau_2/3$.

becomes smaller. β^t and γ^t have a fatigue phenomenon which if input h^t keeps in a high value, β^t and γ^t drops eventually.

As the exploration of the environment, the sequence of firing in the location units of the first layer causes all the weights to self-organize. The weights updating follows the Hebbian rule.

Weights between the first layer and the second layer are updated according to

$$\Delta W_{ij}^t = \epsilon(\psi_j^t r_i^t - \bar{\psi}_j^{t-1}\bar{r}_i^{t-1}) \tag{6.7}$$

where $\epsilon = 5 \times 10^{-3}$ is a positive learning rate. $\bar{\psi}_i^t$ and $\bar{r}_j^t$ are estimated mean firing rates and updating as follow,

$$\begin{aligned} \bar{\psi}_i^t &= \bar{\psi}_i^{t-1} + \eta(\psi_i^t - \bar{\psi}_i^{t-1}), \\ \bar{r}_i^t &= \bar{r}_i^{t-1} + \eta(r_i^t - \bar{r}_i^{t-1}), \end{aligned} \tag{6.8}$$

and $\eta = 0.05$ is a positive averaging factor.

6.3 Formation of encoding fields

In this discussion, simulations were conducted to examine the behavior of adaptive units. And here the parameter ω in Equation 6.3 is equivalent to h in Equation 6.6.

We examined the response properties of adaptive units under different levels of sparsity and mean firing rates. The number of fields generated by an adaptive unit

was primarily influenced by the level of sparsity. To achieve Gaussian-like fields, the mean firing rate was set within a specific range. Conditions with mean firing rates beyond this range will be discussed later.

At low levels of sparsity and mean firing rate, some adaptive units may not develop a field as the virtual rat explores the environment, as depicted in the top row of Figure 6.2.

As the sparsity and mean firing rate increase, all units gradually become involved in encoding the environment with a high firing rate although the number of fields remains limited. In the final row of Figure 6.2, where the sparsity value is 0.20 and the mean firing rate value is 0.10, the adaptive units display multiple firing fields that are situated in close proximity to one another, thus covering a particular region of the environment. Grid cells recorded in the mEC exhibit firing patterns across multiple locations throughout the environment. This phenomenon suggests that actual grid cells possess high levels of sparsity and mean firing rate, as they can cover the entirety of the observed environment.

Once the sparsity and mean firing rate values reach a certain threshold, the adaptive units begin generating fields that effectively cover the entire environment, as depicted in Figure 6.3. Further increasing these parameters will lead to a more compact arrangement of fields. The number of encoding fields per adaptive unit in the environment is illustrated in Figure 6.4.

When the mean firing rate surpasses the required range for Gaussian-like field formation, a distinct pattern of band-like fields emerges. This phenomenon is similar to the band-like representation recorded in parasubicular and medial entorhinal cortices (Krupic et al., 2012).

Turing (1952) proposed that by introducing activators and inhibitors into a reaction-diffusion chemical system, spatial patterns can emerge via competitive interactions between these reagents. The resulting patterns can take the form of regular grids or stripes, as seen in Figure 6.5, similar to the simulation results here.

6.4 Emergence of the regularity

Based on the analysis conducted, it becomes apparent that the increase in the number of Gaussian fields generated by adaptive units leads to the emergence of the first order of regularity in the pattern. This regularity is defined by the distance between adjacent fields, as illustrated in Figure 6.6. As the number of fields continues to

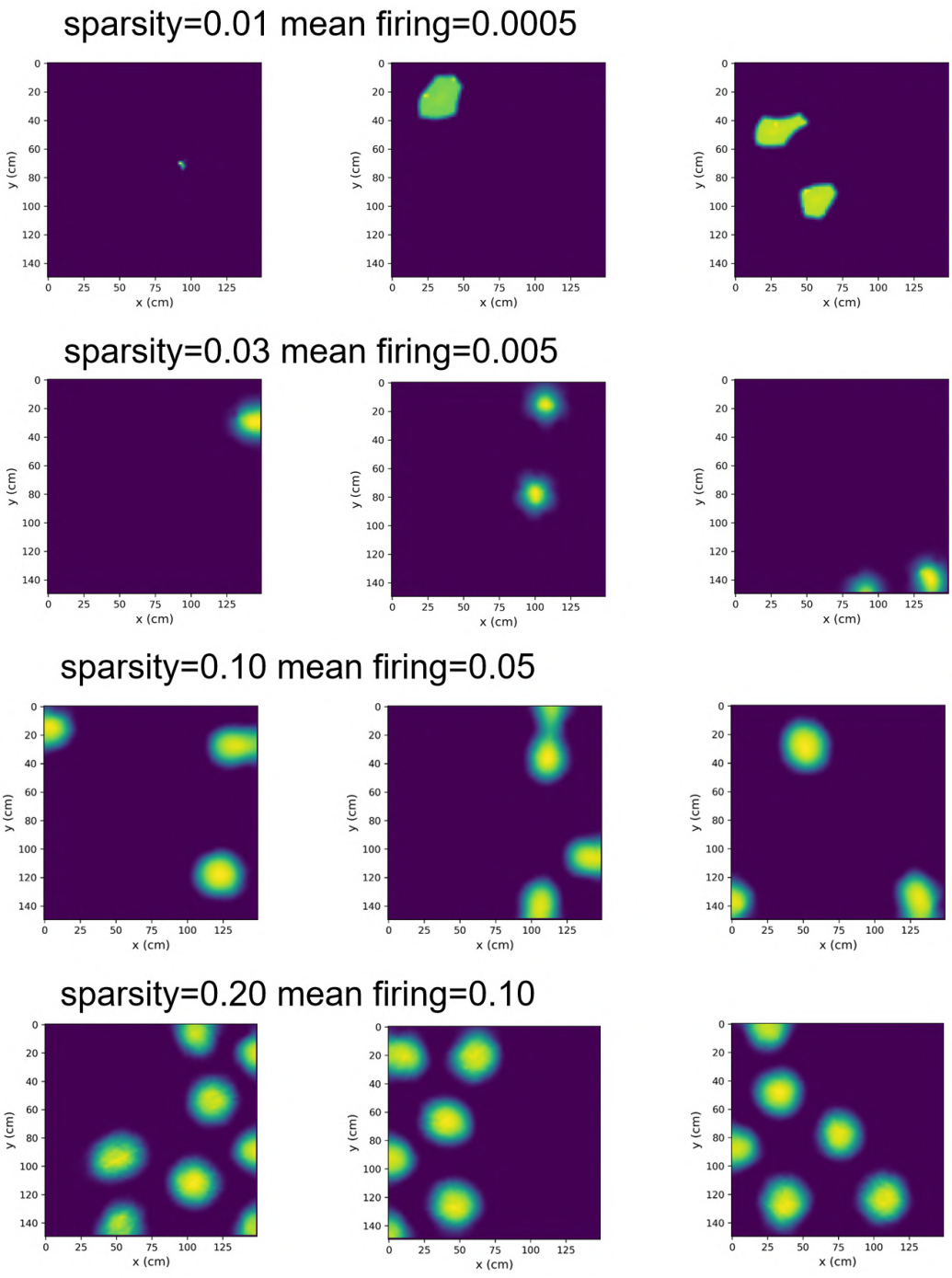

Figure 6.2: Response of adaptive units under the low value of sparsity and mean firing rate. Each row shows three examples of simulation results with 200 adaptive units. In the top row, the values of sparsity and mean firing rate are very low, leading to some adaptive units not displaying clear firing fields. As the sparsity and mean firing rate values increase, all adaptive units start to develop several firing fields.

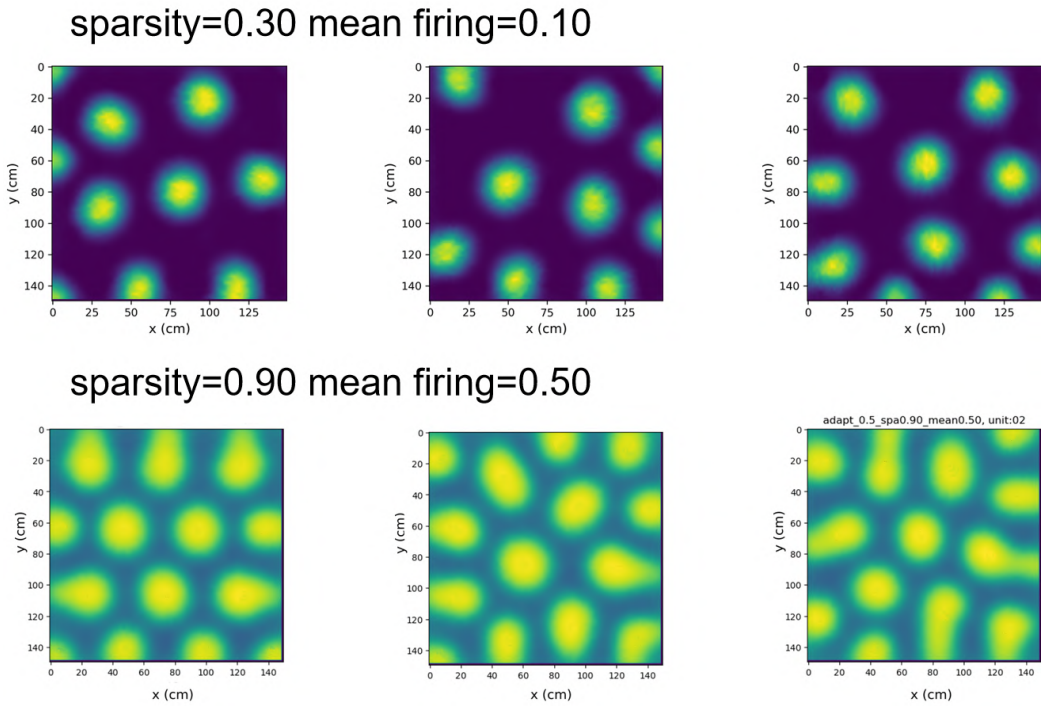

Figure 6.3: Response of adaptive units under higher sparsity and mean firing rate values. In the top row, the units have fields that cover the whole environment in a loose manner. As the sparsity and mean firing rate increase, the number of fields per unit also increases, leading to a more compact arrangement.

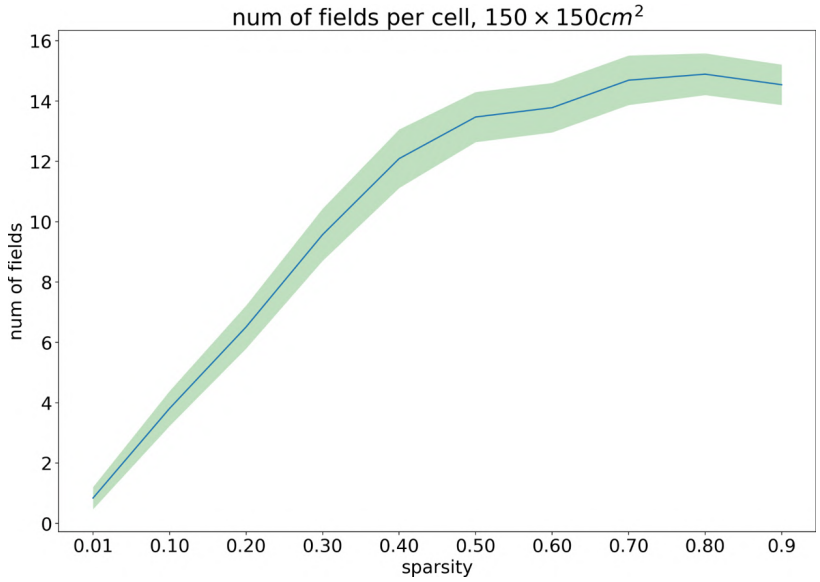

Figure 6.4: Number of fields per unit under different levels of sparsity.

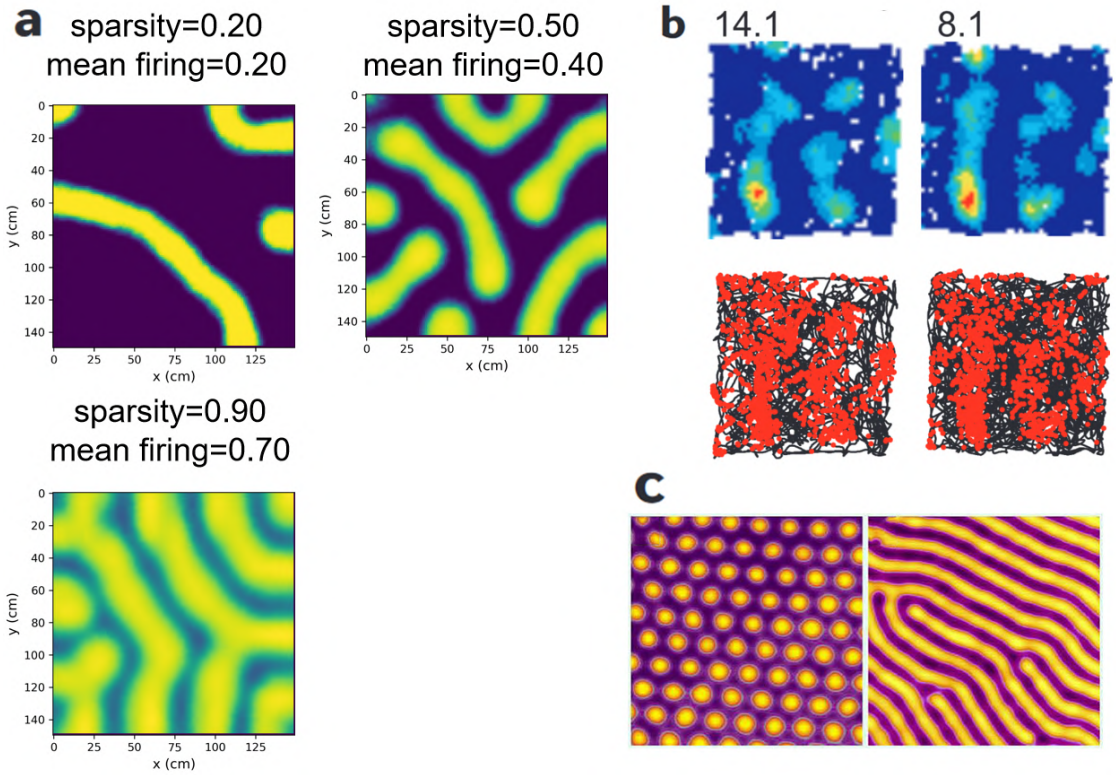

Figure 6.5: Band-like response patterns. a, band-like patterns appear in our simulation when the mean firing rate is higher than needed for Gaussian-like field formation. b, spatially periodic bands representation recorded in parasubicular and medial entorhinal cortices, adapted from (Krupic et al., 2012). c, result patterns from the reaction-diffusion chemical system with differences in the reaction parameters, adapted from (Borckmans et al., 2002).

increase, the distances between the fields become more clustered, leading to a distinct bump pattern. This bump pattern indicates the additional regularity observed between non-adjacent fields in adaptive units.

Next, we utilize various response dynamics of the input from equation 6.6 as the input of the transfer function for the second layer adaptive units. Since the environment for regular pattern formation is a two-dimensional square environment, we employ the gridness method to quantify the level of regularity (Hafting et al., 2005).

Upon comparing the regularity of different response dynamics as depicted in Figure 6.7, we observe that alpha exhibits the poorest performance, followed by the direct input, with beta performing better, and gamma providing the best performance in terms of gridness.

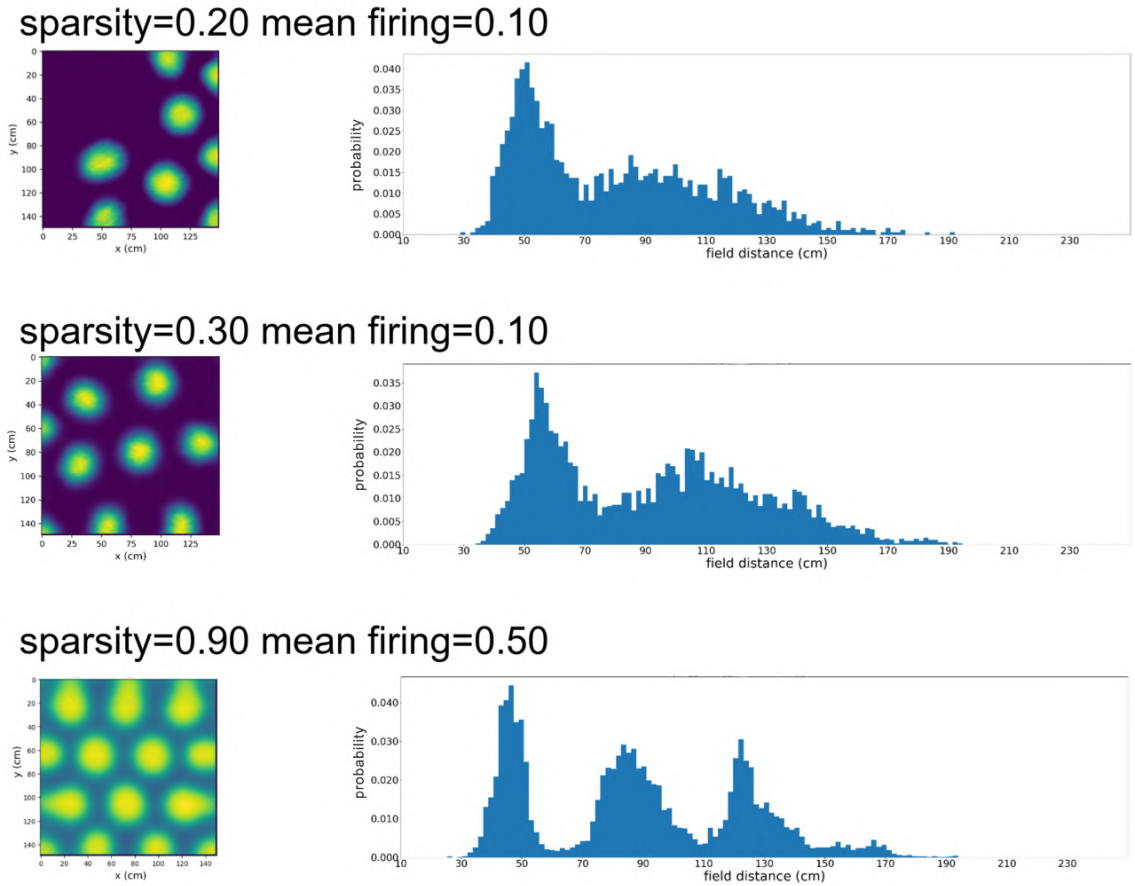

Figure 6.6: As the number of fields increases, the emergence of regularity can be observed in the patterns generated by the adaptive units. The left side of the figure displays examples of these patterns for varying levels of sparsity and mean firing rates, with the values indicated above each panel. The histograms on the left show the distribution of distances between fields in each simulation, highlighting the emergence of regularity.

6.5 Discussion

The development of a concept follows a systematic process that includes observation, experimentation, analysis, and revision. This iterative and dynamic process is guided by the accumulation of evidence and the continuous refinement of theories over time. The concept of "grid cells" is no exception and has also undergone a similar concept development journey. Recent discoveries have further propelled this ongoing journey of concept development of "grid cells" (Ginosar et al., 2023).

In this chapter, we have delved into the discussion of grid cells and explored two fundamental properties associated with them by a simplified self-organization model. The first property focuses on the formation of encoding fields, which is intricately

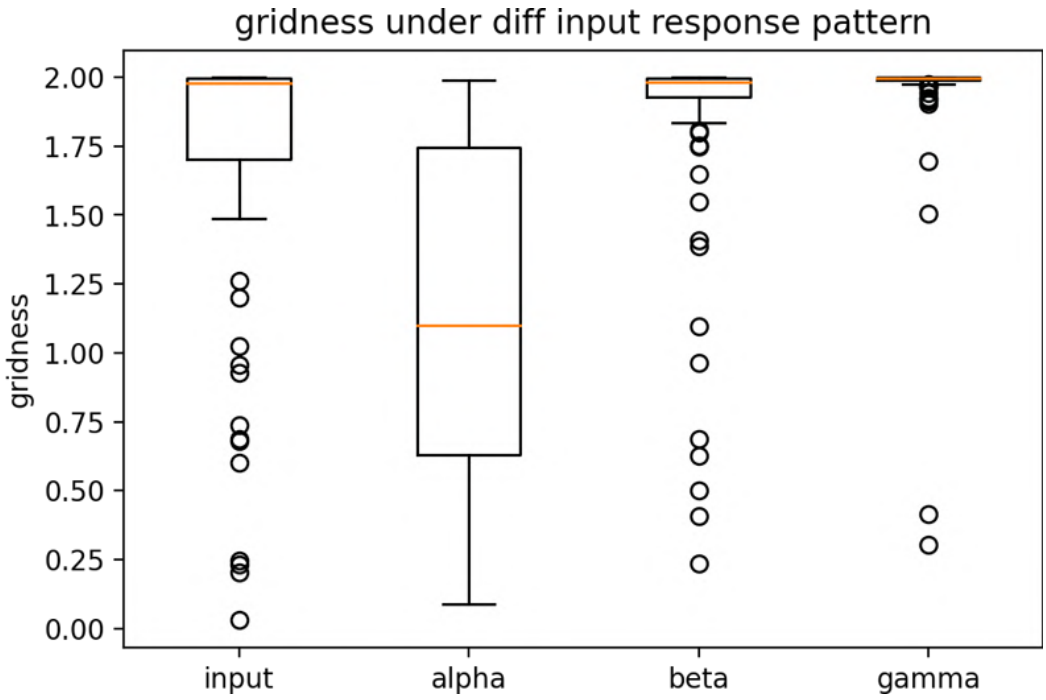

Figure 6.7: Gridness under different response dynamics of the input.

linked to the concept of neuronal sparsity.

Research on the sparsity of cell firing has revealed that it is influenced by a range of factors and mechanisms within the neural system (Olshausen, Field, 2004; Spanne, Jörntell, 2015). A general overview of some factors that can affect the sparsity of cell firing based on commonly known principles in neuroscience lies below:

Intrinsic properties of neurons: Different types of neurons may exhibit inherent differences in their firing patterns and sparsity. For example, certain inhibitory interneurons are known to contribute to sparse firing patterns.

Network connectivity: The connectivity patterns between neurons can play a role in shaping the sparsity of cell firing. Inhibitory connections, such as those mediated by parvalbumin-expressing interneurons, can regulate the activity of excitatory neurons and contribute to sparse firing patterns.

Input statistics: The statistical properties of the inputs received by neurons can influence their firing sparsity. For instance, if the inputs are highly correlated or exhibit specific patterns, it can impact the sparsity of cell firing.

Neuromodulation: Neuromodulatory systems, such as the release of neurotransmitters like dopamine or norepinephrine, can modulate the activity of neurons and affect their firing sparsity.

The difference between place cells and grid cells could be attributed to the sparsity of neuron firing.

This specific form of regularity can emerge when each unit possesses a sufficient number of encoding fields, and the inputs are suitably manipulated, along with interactions between units. In the conducted simulations, even in the absence of explicit recurrent connections between units, the interaction between units can be understood by considering the control of sparsity.

The study of regularity emergence has gained significant attention across multiple disciplines, including physics, biology, computer science, and sociology. Researchers seek to understand the underlying principles and mechanisms that give rise to these emergent regularities, as they provide valuable insights into the fundamental principles governing complex systems.

The dynamic of grid cells which appeared as some degree of deviation and variability has been discussed in the last chapter. In a nutshell, biased sampling could cause the dynamics.

In conclusion, grid cells can be understood as a type of brain information processing unit that possesses a sufficient number of encoding fields, which enables the emergence of specific regularity. Additionally, grid cells exhibit dynamics that may arise due to biased sensory inputs discussed in the last chapter.

6.5.1 Path integration

Path integration in behavioral studies refers to the mechanism by which an animal continuously updates its position and orientation in space based on self-motion cues and without relying on external landmarks. It involves integrating information from various sensory inputs, such as proprioception, vestibular cues, and motor efference, to estimate changes in position and direction relative to a starting point (Etienne, Jeffery, 2004; McNaughton et al., 2006; Savelli, Knierim, 2019).

Every representation system is integrating external information. However, a representation system equipped with a robust capacity for regular representation can notably decrease its dependence on external data. By effectively capturing and utilizing internal regularities, such a system can enhance its efficiency, accuracy, and resilience, ultimately leading to more robust and autonomous functioning.

The discussion regarding the contribution of grid cells to path integration can be described in terms of how the presence of this type of regular pattern reduces the spatial cognition system's reliance on external information. With grid cells integration speed and direction information to enable each grid cell to have the capacity to encode

plenty of fields and the regularity between them, grid cells would assist the spatial representation system grid cells to participate in a decrease in external information dependent.

Chapter 7

Infraslow Up and Down States (IsUDS) in drug-free animals

7.1 Introduction

Behavior involves a broad spectrum of timescales, spanning from tens of milliseconds to seconds, minutes, and beyond. The coordination of neural activity across such diverse scales is a compelling question in neuroscience (Mehta, 2001).

Neural oscillations are commonly invoked mechanisms to tackle this challenge. Consistently, cortical neurons show oscillations with periods ranging from $\sim$ 5ms (e.g. ripples), $\sim$ 20ms (gamma oscillations), $\sim$ 100ms (theta) and $\sim$ 1000ms (delta). Bridging across these different scales spanning three orders of magnitude is thought to occur via coupling between their amplitudes and phases. For example, theta-gamma amplitude-phase coupling is implicated in working memory (Lisman, Jensen, 2013).

This leaves open the question about how oscillations can organize neural activity across even longer time-scales of 10s and several hundred of seconds. Recent studies have highlighted the presence of infraslow oscillations (Dash, 2019; Cogno et al., 2022; Bueno-Junior et al., 2023; Väyrynen et al., 2023; Turi et al., 2023). However, the mechanisms of generation of these oscillations, their coupling to shorter timescale oscillations, and their relationship to behavior remain to be determined (Watson, 2018).

Importantly, many studies suggest that behavior modulates rhythmic dynamics –e.g. theta is larger during locomotion and delta is larger during immobility and sleep. However, in contrast to this 'outside in mechanism' an alternate possibility exists, 'an inside out mechanism' where these differential rhythms cause changes in behavior.

Hence we investigated the temporal dynamics of all the oscillations and their relationship to faster oscillations in the cortex in vivo, in freely behaving rats as well as anesthetized rats. Investigations in freely behaving, drug-free rats were done using tetrodes that provided the Local field potential (LFP) and spiking activity of many neurons. Anesthetized animal studies allowed simultaneous measurement of the LFP and membrane potential from anatomically identified neurons.

7.2 Results

As a first step, we examined the LFP recorded from the parietal cortex while the rats were resting in a box, placed in a quiet room with dim lights, without any distractors, tasks, or rewards.

Visual examination shows clear fluctuations in the magnitude of the LFP over periods of 800s of seconds. An example of LFP is shown in Figure 7.1.

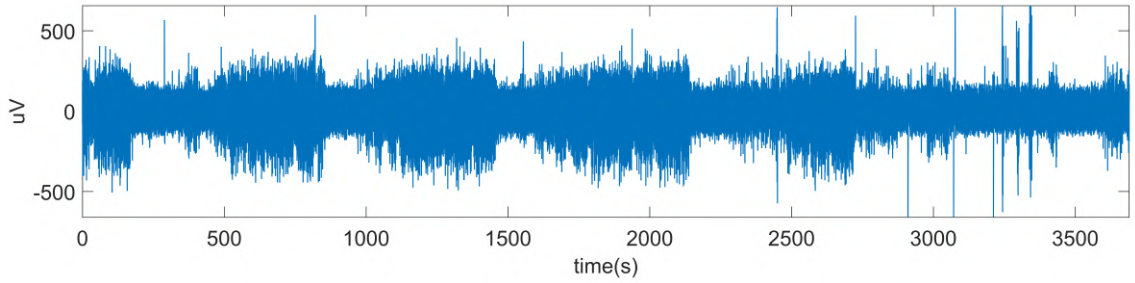

Figure 7.1: Temporal dynamics of a freely behaving rat LFP.

This can be quantified by computing the standard deviation of the LFP over periods of 10s which shown in Figure 7.2.

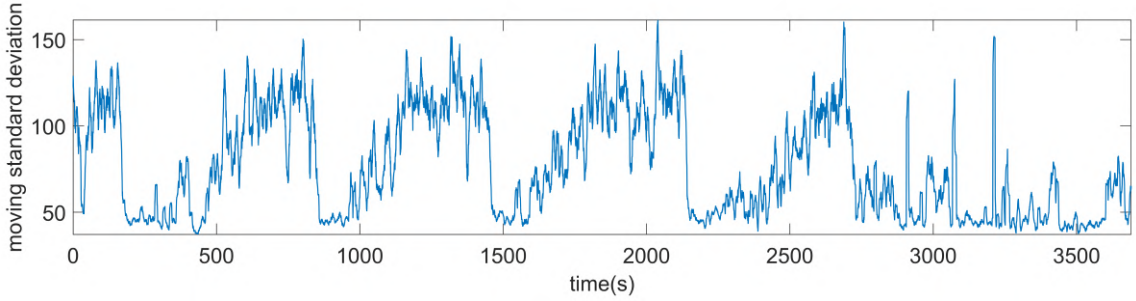

Figure 7.2: Moving standard deviation of LFP with a 10s window.

This confirms our visual impression and shows infraslow oscillations of the LFP with a period of about 800s.

To quantify this, we computed the autocorrelation function and power spectrum for both the absolute value of the LFP and the moving standard deviation of the LFP. Autocorrelation was obtained with MATLAB function autocorr from Econometrics Toolbox. Power spectrum was obtained with MATLAB function mtspectrumc from chronux toolbox (with parameter pad=2 and tapers=[3 1], http://www.chronux.org).

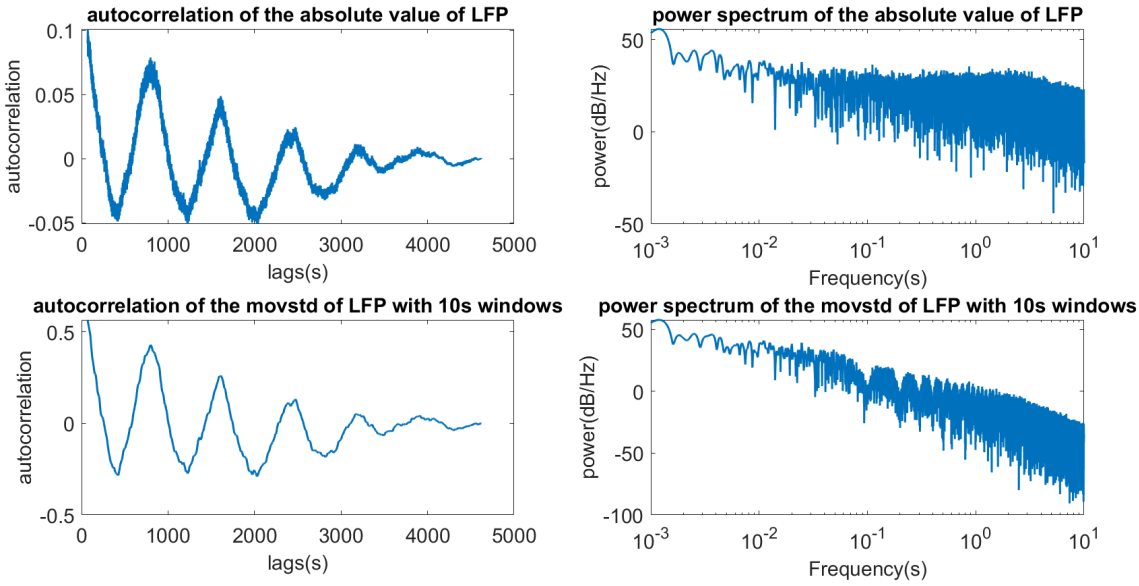

Figure 7.3: Autocorrelation function and the power spectrum of LFP. The first row is for LFP absolute value, the second row is for the moving standard deviation of LFP with a 10s window.

In Figure 7.3, the autocorrelation shows slow modulation with a period of around 800s. The power spectrum too shows a clear peak at 0.0012Hz, corresponding to a period of 800s.

Further, the infraslow oscillations were bimodal, with a relatively abrupt transition between high and low standard deviation. This was confirmed by computing the histogram of the moving standard deviation of the LFP computed over a 10s moving window, indicated in Figure 7.4.

Thus the infraslow oscillations of the LFP amplitude is not sinusoidal but bimodal, i.e. infraslow up-and-down state oscillations (IsUDS), similar to the classic, Up-and-Down states seen during slow wave sleep, also known as the delta-oscillations (Petersen et al., 2003; Torao-Angosto et al., 2021).

Further, the IsUDS transitions were asymmetric – the transition from low to high amplitude LFP was slow, but the transition out of high to low amplitude was relatively abrupt. This was confirmed by computing the transition triggered average of the LFP

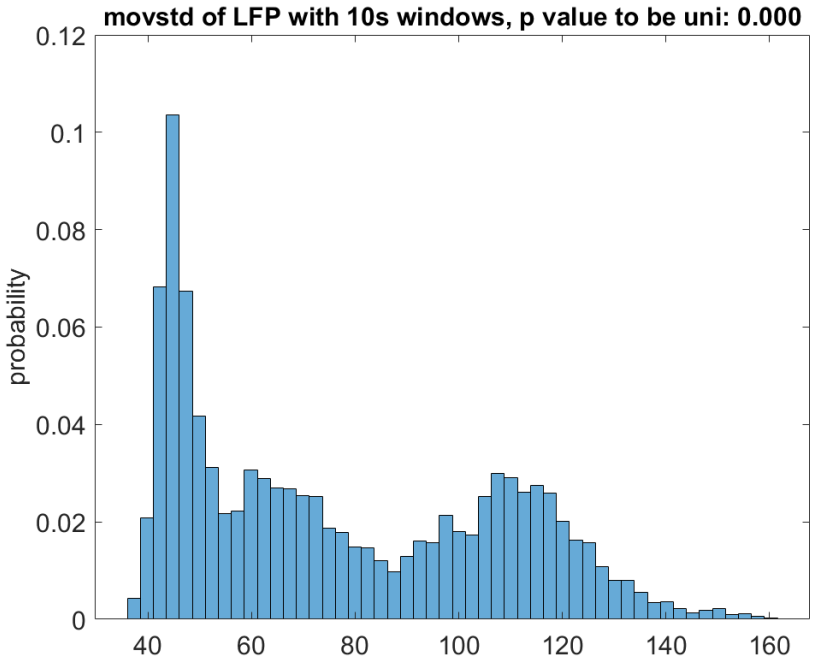

Figure 7.4: Bimodality of the moving standard deviation of LFP.

magnitude, shown in Figure 7.5. The triggered average was aligned with the beginning time point and end time point of Non-rapid eye movement sleep (NREM). NREM was identified using a threshold method, where the amplitude of the filtered signal in the delta band range (0.5-4Hz), obtained through the Hilbert transform, exceeded the mean value with one standard deviation.

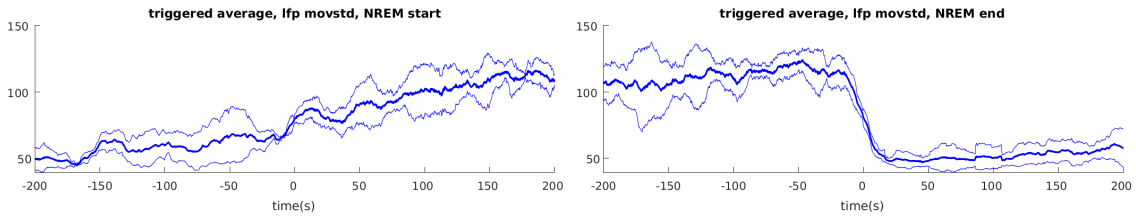

Figure 7.5: Triggered average of the moving standard deviation of LFP. Panel to the left shows low-to-high STD transition triggered average. Panel to the right shows the high-to-low amplitude transition. The mean value is shown by the solid line, standard deviation by the thin lines

To confirm the general validity of these findings we did similar analysis on a large set of data (39 LFPs from different recording sessions, with 4 rats). From these,

we extracted the magnitude and frequency of the largest peak in the low-frequency range. The lowest frequency range was restricted to corresponding to 2/duration of recording. If a clear peak was not visible in a session, that session was discarded. The power and period of the IsUDS are shown in Figure 7.6.

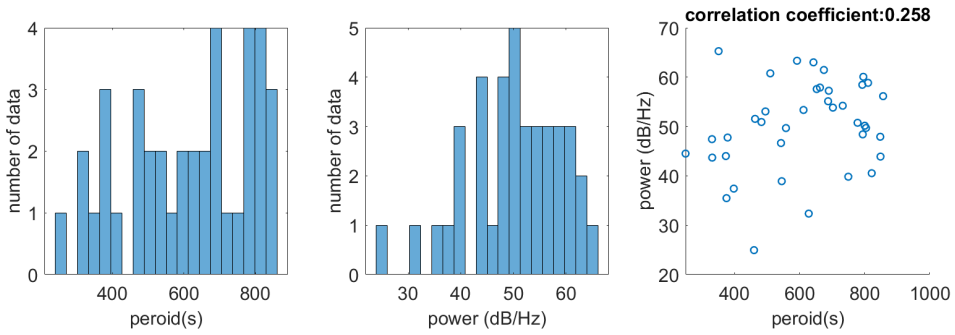

Figure 7.6: Magnitude and period of IsUDS are positively correlated. Panel to the left shows the distribution of IsUDS periods, determined from the location of the highest amplitude peak. The middle panel shows the amplitude of the IsUDS peak in the power spectrum. Panel to the right shows that the two were positively correlated with a correlation coefficient of 0.258.

Thus, data shows spontaneous IsUDS oscillations with a period of 610.64 ± 176.71 seconds, with a power of 50.16 ± 9.13 dB.

Notably, these changes occurred spontaneously, without any external events, since the rat was left undisturbed for the entire period in a 60dB sound-insulated room.

To determine the fine structure of these IsUDS we looked carefully at a segment of data with high amplitude LFP and another segment with low amplitude LFP.

Figure 7.7 shows that the high amplitude LFP contained slow wave sleep (SWS) oscillations, also known as the Up-Down State (UDS) oscillations, or delta oscillations (0.5-4Hz). This is marked by about 1s long Up states and about 100ms long down states. Down states during SWS are not stable and rather short-lived, consistent with classic data.

To confirm this, we filtered the LFP in the delta band (0.5-4Hz) and computed the amplitude of the filtered signal using Hilbert transform, shown in Figure 7.8.

This too showed clear IsUDS, similar to the standard deviation of the broadband LFP, suggesting that the 800s IsUDS oscillations of the LFP amplitude are largely driven by fluctuations in the 1s (0.5-4Hz) delta oscillation magnitude. The autocorrelation and the power spectrum of the delta oscillations showed results similar to that for the moving standard deviation of LFP, shown in Figure 7.9.

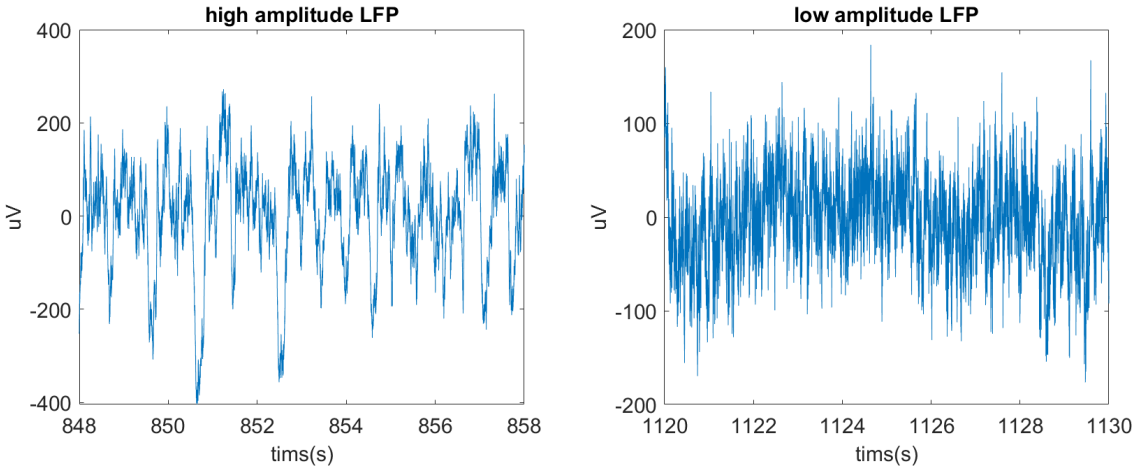

Figure 7.7: LFP segments with high (left) and low (right) amplitudes. Note the difference in y-axis time scale.

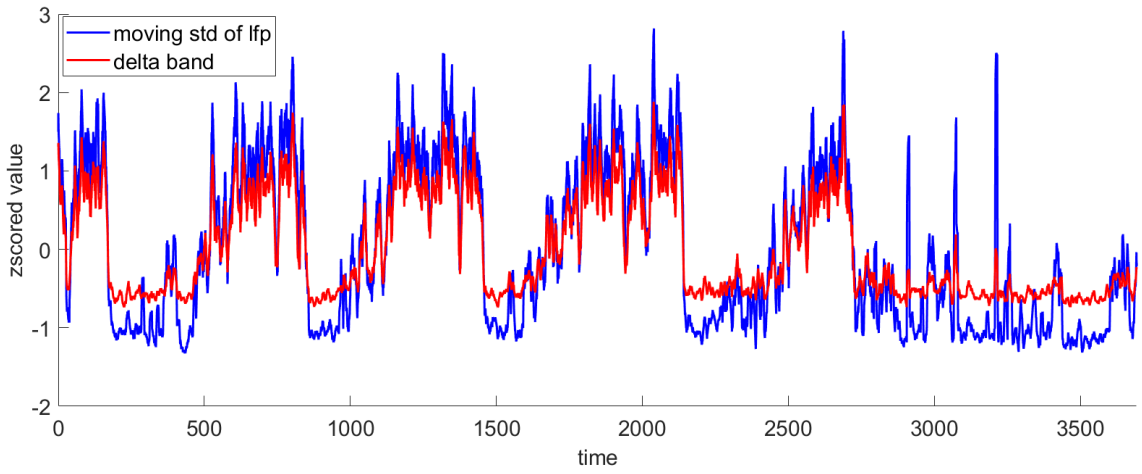

Figure 7.8: Delta band signal accounts for the most part of moving standard deviation of LFP IsUDS.

Across the ensemble of the same data mentioned above, results shown in Figure 7.9, clear peaks in the IsUDS band was found, with average period of 710.45 $\pm$ 168.23s and amplitude of 52.10 $\pm$ 8.46 dB. And the periods of IsUDS show positive correlation with maximum peak in the power spectrum with a correlation coefficient of 0.415. These results are consistent with the moving standard deviation based results confirming the hypothesis that IsUDS oscillations are largely caused by fluctuations of delta band oscillations.

The Hilbert transform magnitude of filtered LFP in delta band (0.5-4Hz) also shows clear bimodality, shown in Figure 7.10, similar to the moving standard deviation

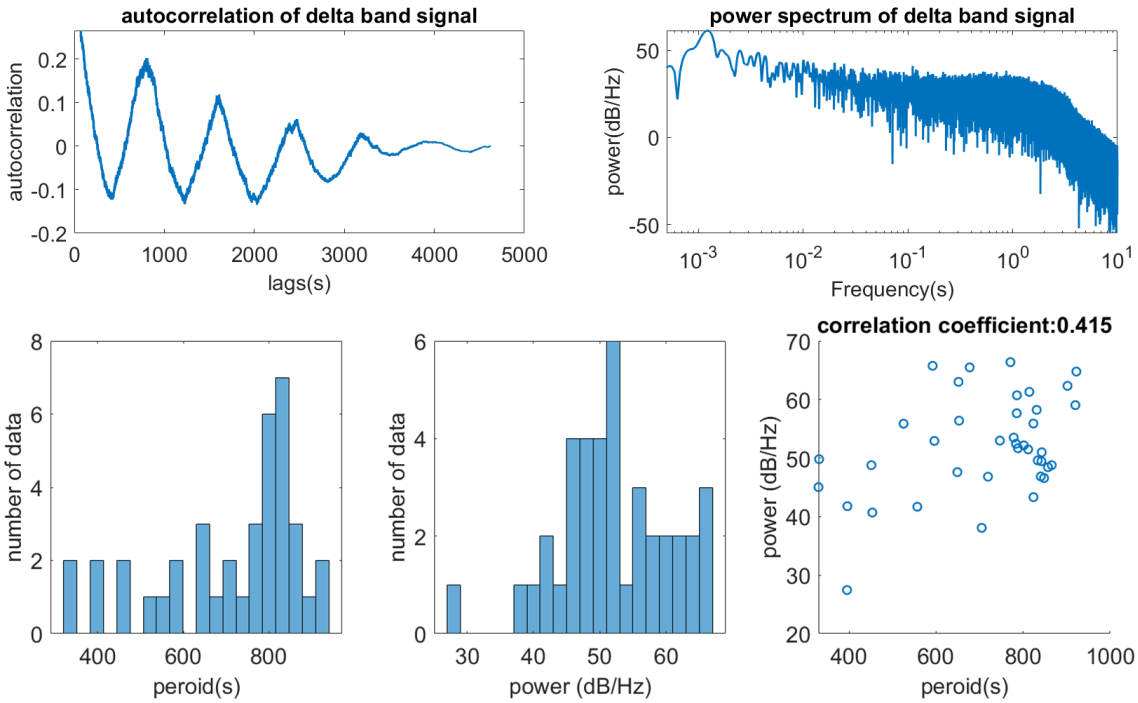

Figure 7.9: Autocorrelation and the power spectrum of the magnitude of delta band filtered LFP. First row is for the same example as described above, the second row is for the same data set as above.

of LFP. Further, the transition to the high amplitude delta band was slow, but the transition out of high to low amplitude was relatively abrupt, shown in Figure 7.11 which is similar to the moving standard deviation of LFP.

The power spectrum of the low-frequency delta band filtered LFP exhibited notable peaks at frequencies higher than the IsUDS range, as depicted in Figure 7.12. Power spectrum was obtained with MATLAB function mtspectrumc from chronux toolbox (with parameter pad=2 and tapers=[3 5], http://www.chronux.org). This observation is further supported by the moving standard deviation of the LFP.

Frequencies higher than the IsUDS range of the data set we analyzed are classified into NREM and outside NREM, as depicted in Figure 7.13. Each delta band filtered LFP was divided into segments of NREM and outside NREM, based on the previously detected NREM locations. For each segment of recordings, we extracted the frequency and power from the maximum peak of the power spectrum. The periods were restricted to correspond to 2/duration of each segment of recordings. During NREM sleep, the power of certain signals is greater compared to periods outside of NREM sleep. Additionally, the durations of NREM sleep periods tend to be longer than those occurring during non-NREM states.

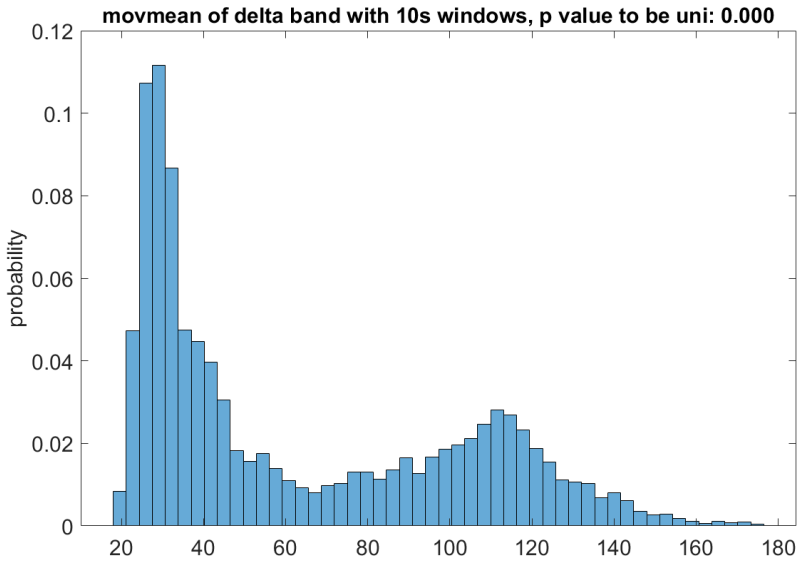

Figure 7.10: Bimodality of the moving mean with 10s window for delta band filtered LFP.

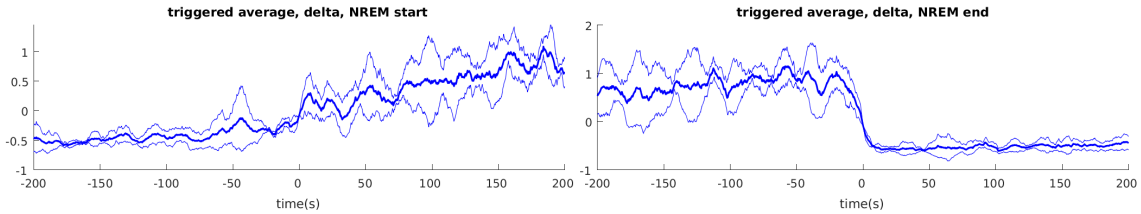

Figure 7.11: Triggered average of the moving mean with 10s window for delta band filtered LFP.

To determine the relationship between these diverse low frequency oscillations and neural spiking, we computed the cross-correlation between the delta band filtered LFP and spike times, shown in Figure 7.14. The two spike times correspond to two pyramidal neurons that display periodic correlation with IsUDS, but they occur with distinct phase shifts. These two different pyramidal neurons were recorded simultaneously on the same tetrode along with the LFP.

The correlation of another spontaneous recording of interneurons with IsUDS is shown in Figure 7.15. Periodic correlation with IsUDS is clear while with an anti-correlation at zero lag.

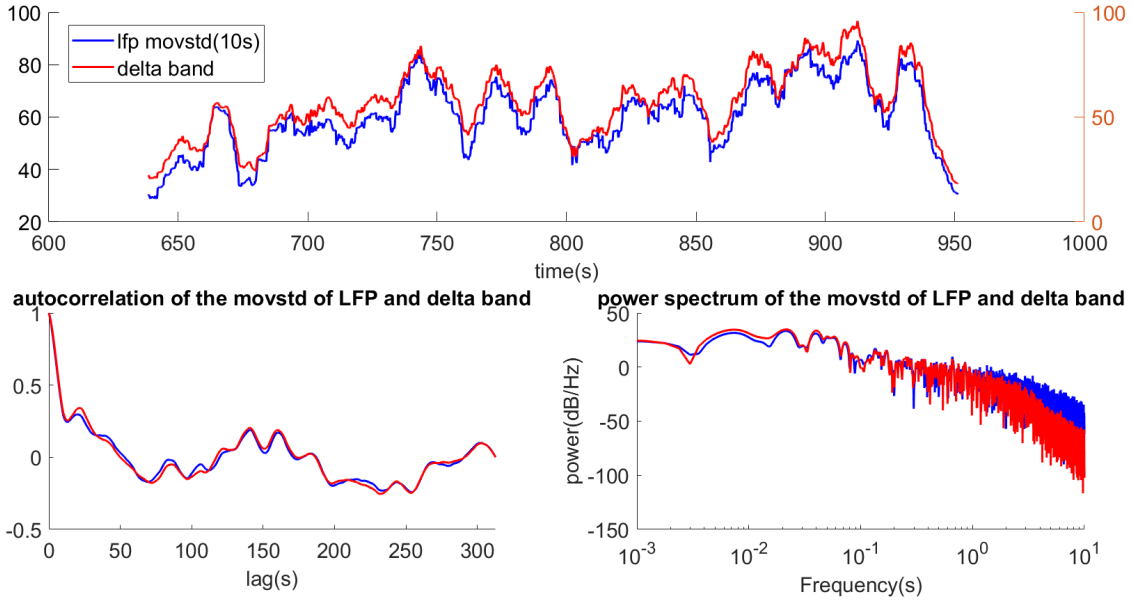

Figure 7.12: Zoomed in segment of one IsUDS period showing higher frequency modulation. This is confirmed by the zoomed in autocorrelation (bottom left) and power spectrum (bottom right) showing peaks at higher frequencies.

7.3 conclusions

Behavior spans a broad spectrum of timescales, ranging from rapid changes in the order of tens of milliseconds to more extended periods lasting seconds, minutes, and beyond. Neural oscillations serve as dynamic windows that facilitate the connection between these diverse behavioral timescales and underlying neural activity. How oscillations related to long timescales of 10s and several hundred seconds behaviors is less discussed.

In the data recorded from freely behaving rats, infraslow up-down states (IsUDS) range oscillations of approximately several hundred seconds were evident and clear.

The IsUDS of the LFP amplitude is largely driven by fluctuations in the delta oscillation magnitude.

The amplitude of IsUDS oscillations in both the moving standard deviation of LFP with a 10s window and the delta band filtered LFP smoothed with a 10s window exhibits a bimodal distribution, resembling the characteristic pattern observed in classic up-and-down states.

The transition into the high-amplitude LFP and theta band filtered LFP occurred gradually, with a slow change. However, the transition from the high amplitude to

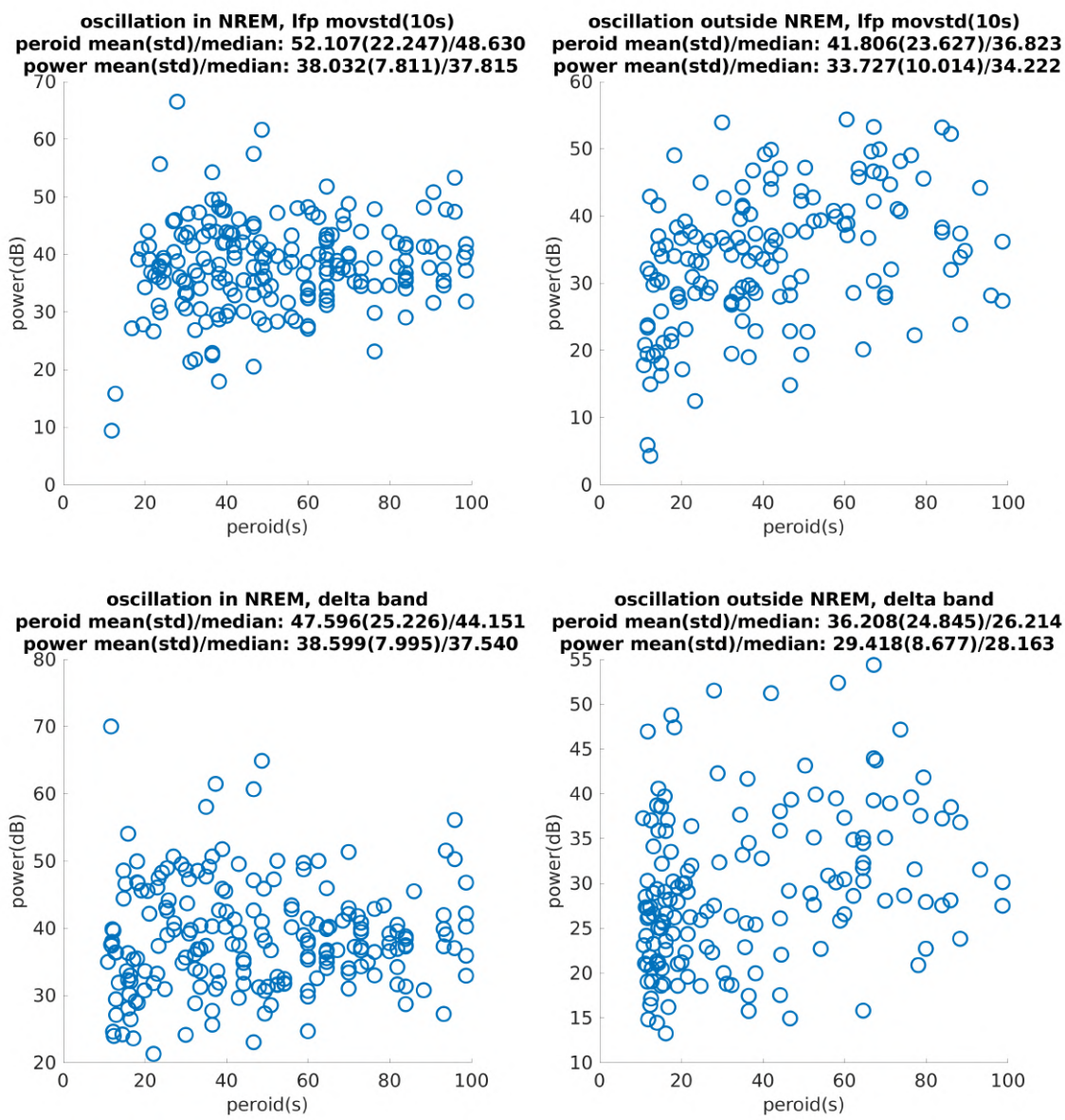

Figure 7.13: Power spectrum period and power in frequencies higher than the IsUDS range.

the low amplitude was relatively abrupt and occurred rapidly.

In addition to the IsUDS frequencies, the signal also encompasses numerous higher frequencies beyond the typical range associated with IsUDS activity.

The simultaneous firing pattern of neurons, comprising both pyramidal neurons and interneurons, displays periodic correlations with IsUDS oscillation. However, even within the same cell types, these correlations occur with diverse phase shifts.

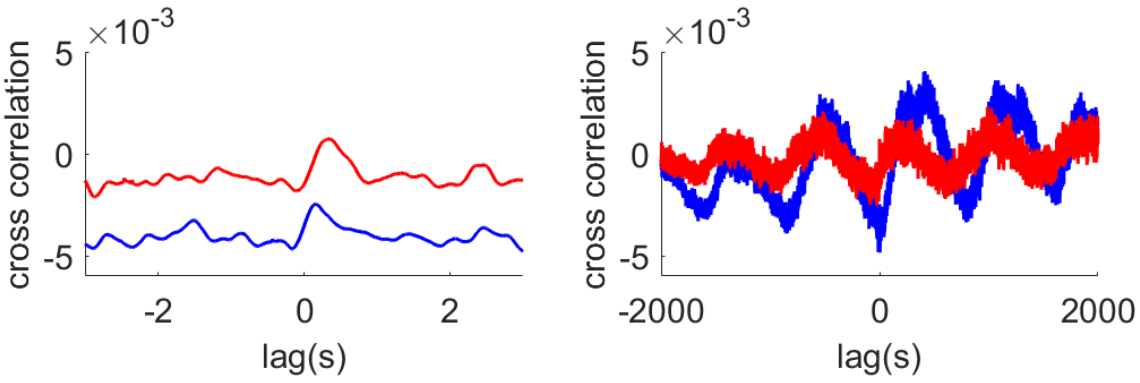

Figure 7.14: Cross correlation of IsUDS with spike train.

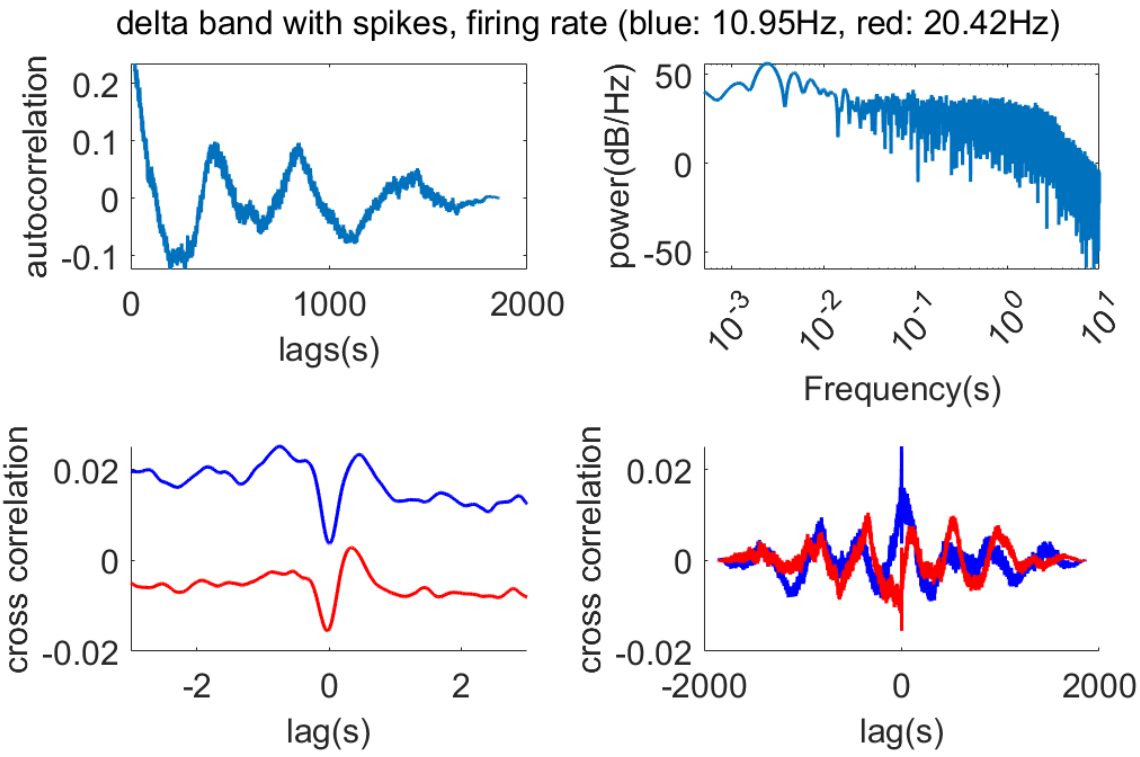

Figure 7.15: Cross correlation of IsUDS oscillation with interneuron spike train. The firing rates of the interneurons are labeled at the top. This first row indicates the autocorrelation and power spectrum of the LFP from the same tetrode.

Chapter 8

Coupling of IsUDS to faster timescale oscillations spanning four orders of magnitude

8.1 Introduction

In order to bridge the gap between different behavioral timescales, it is necessary for them to be coupled. Studies have shown that coupling between theta oscillations $\sim$ 100ms and place cells $\sim$ 1000ms are crucial for sequence learning (Mehta, 2015). Coupling between $\sim$ 100ms theta and $\sim$ 20ms gamma oscillations are crucial for working memory (Lisman, Jensen, 2013). Theta oscillations are thought to typically appear during awake states in the hippocampus whereas the slow delta oscillations are thought to appear in the cortex during sleep and theta-to-delta ratio is often used to characterize states of consciousness.

Hence here we looked at the IsUDS spectral dynamics and their coupling across four orders of magnitude.

8.2 Results

As a first step, we obtained the filtered signal in the delta band range (0.5-4Hz), theta band range (5-14Hz), slow gamma band range (15-55Hz), fast gamma band range (65-115Hz), ripple band range (125-155Hz), and spike band range (185-235Hz), shown in Figure 8.1. The frequency ranges for each band are selected to ensure that the filtered signal exhibits a relatively higher coefficient of variation.

Further, in Figure 8.2, the IsUDS for several bands were bimodal, with a relatively abrupt transition between high and low standard deviation. This was confirmed by

computing the histogram of Hilbert transform amplitude of several frequency bands and the zscore value of them.

Figure 8.2 displays the first two rows corresponding to the delta band, theta band, and slow gamma band. The first row represents histograms of the raw Hilbert transform amplitude, while the second row shows histograms of the corresponding z-scored Hilbert transform amplitude. The title of each plot indicates the p-value for testing the distribution's unimodality, obtained using the MATLAB function HartigansDipSignifTest. The bottom two rows exhibit the fast gamma band, ripple band, and spike band data, following the same methodology as described above.

Afterward, we calculated the cross-correlation between different frequency bands using the MATLAB function "crosscorr" from the Econometrics Toolbox. The outcomes of the cross-correlation analysis are depicted in Figure 8.3. Notably, several cross-correlations between different bands exhibit the IsUDS structure.

The cross-correlation between large-scale and narrow-scale signals is consistent, indicating that if the cross-correlation around zero range is negative in the large scale, it will also be negative in the narrow scale, and vice versa. The filtered LFP of high-frequency bands, such as the ripple band and spike band, exhibit a similar structure to the fast gamma band filtered LFP. Averaged cross-correlation shown in Figure 8.4 indicates the same structure.

8.3 conclusions

Filtered LFP in several frequency bands exhibits the IsUDS structure. IsUDS in multiple frequency bands displays bimodality, characterized by a distinct transition between high and low values. Additionally, different frequency bands demonstrate unique coupling structures.

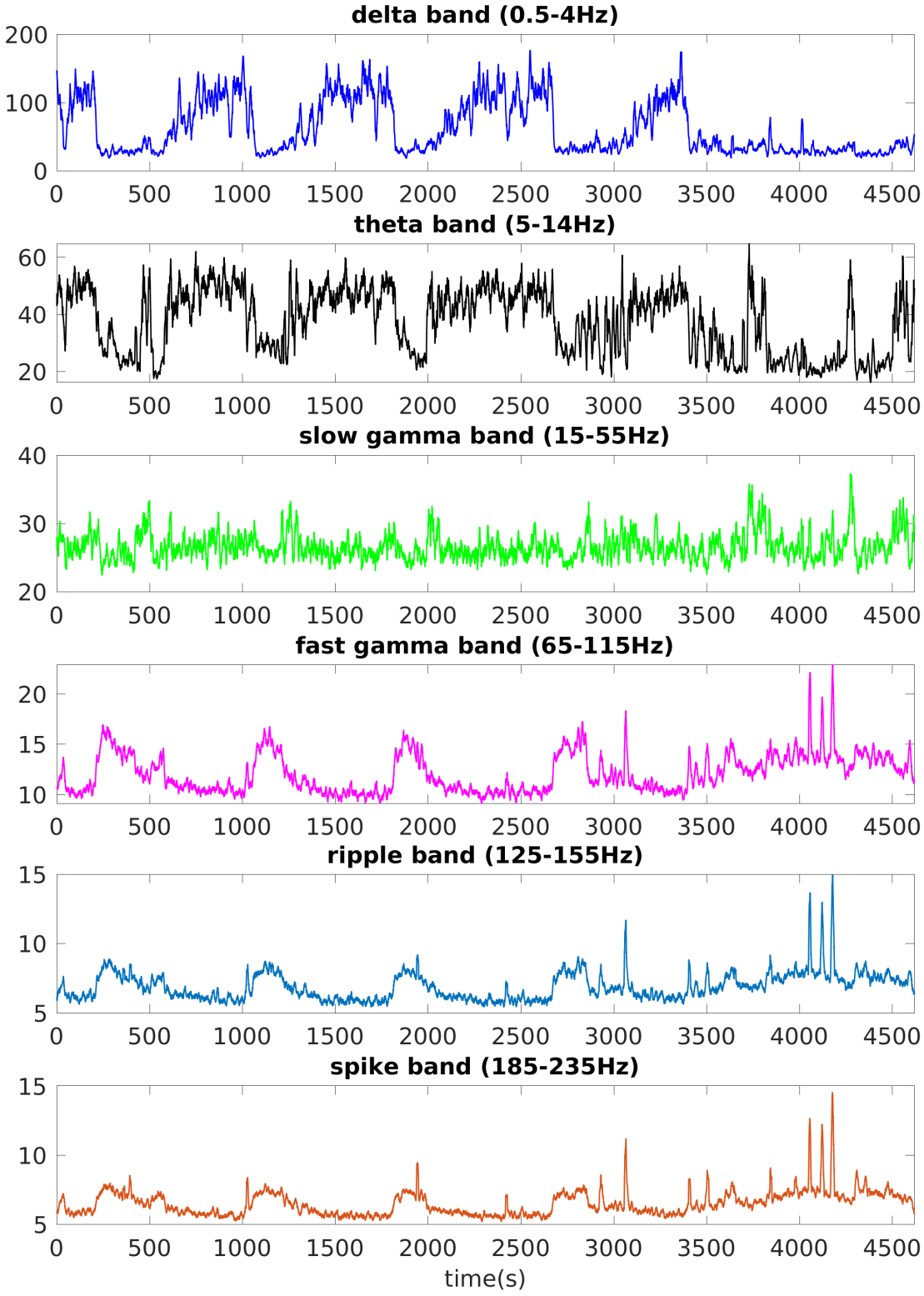

Figure 8.1: Hilbert transform amplitude of several frequency bands.

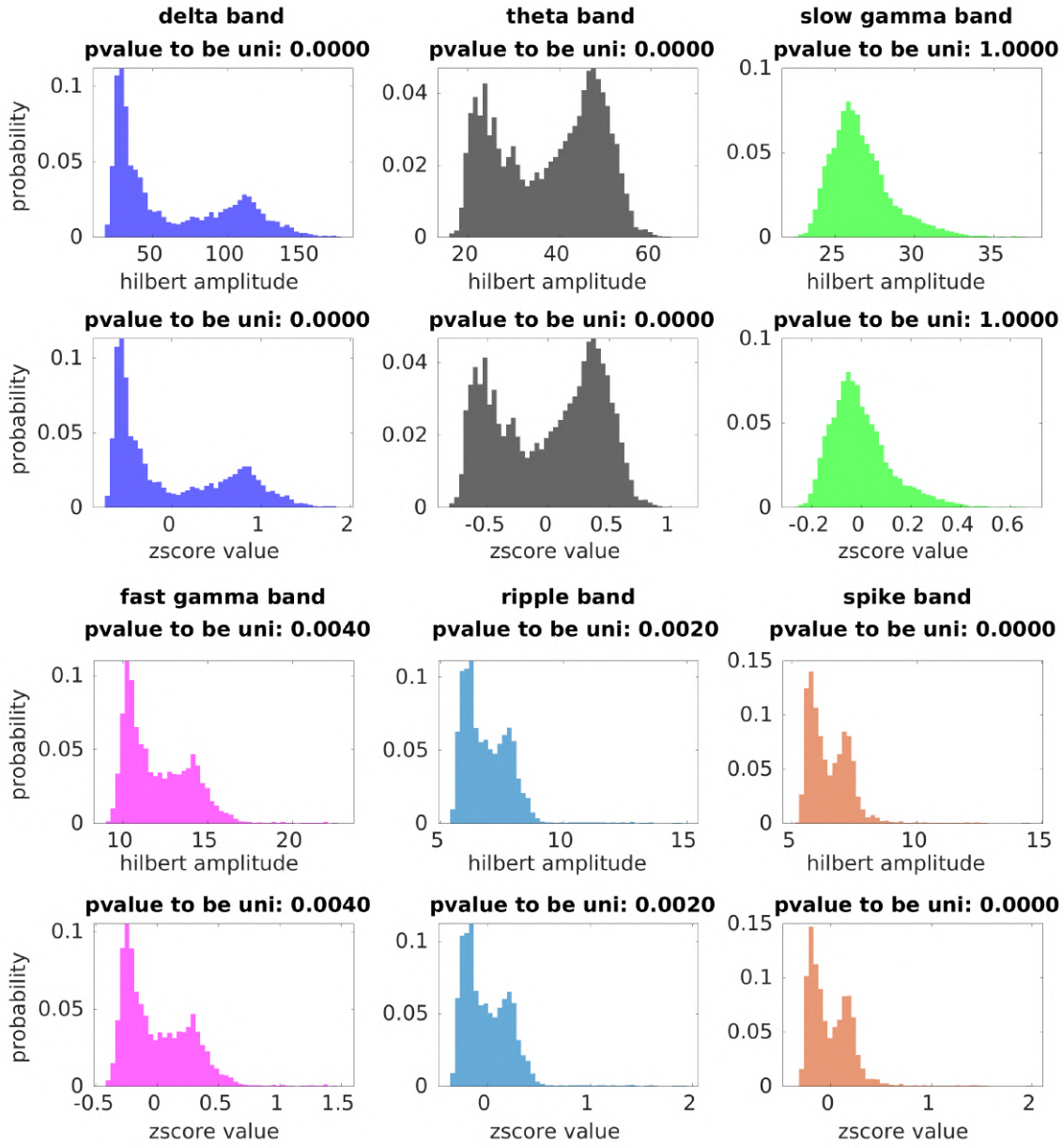

Figure 8.2: Bimodality of several frequency bands in Hilbert amplitude and zscored value.

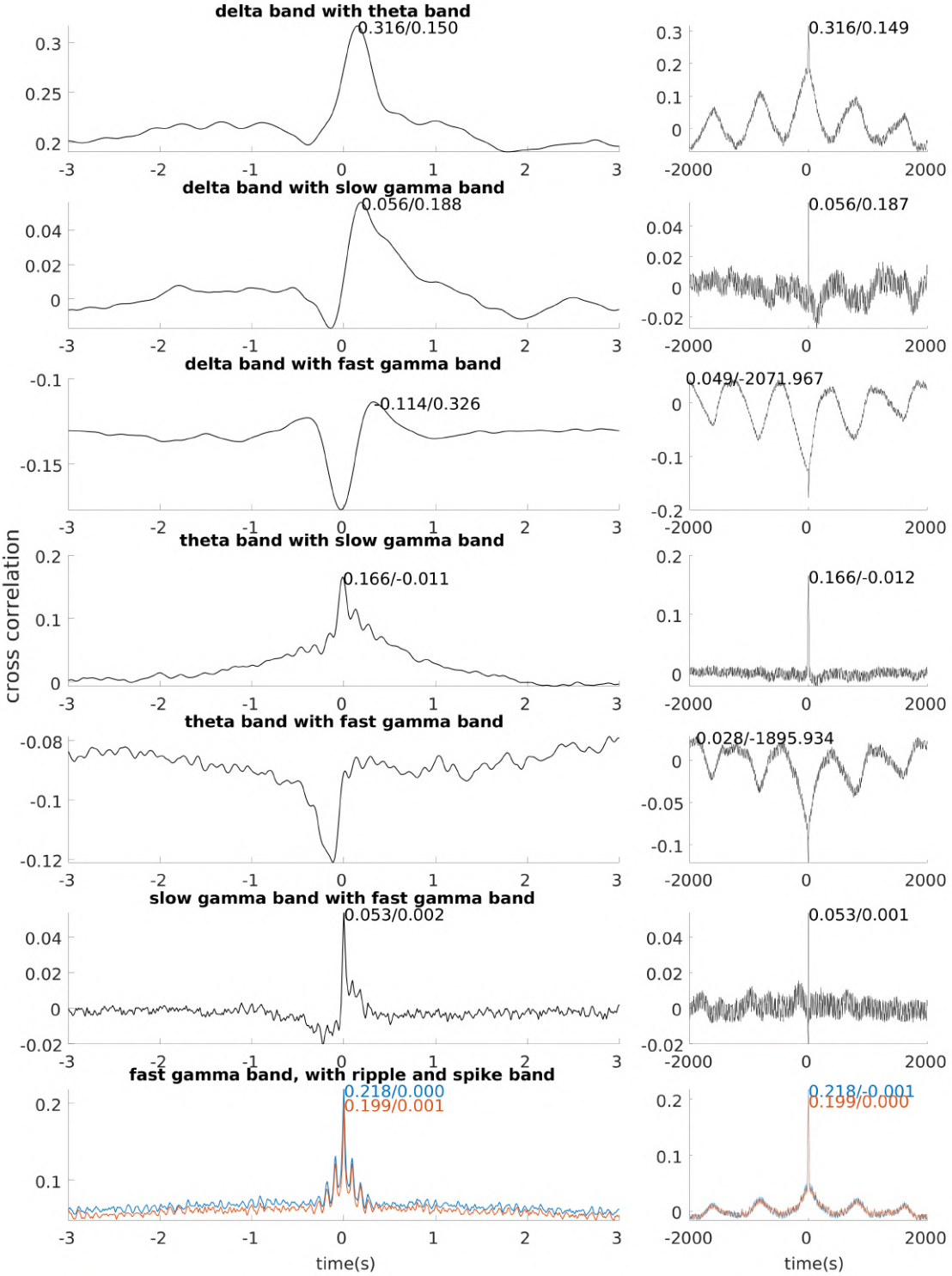

Figure 8.3: Cross-correlation of Hilbert transform amplitude for several frequency bands.

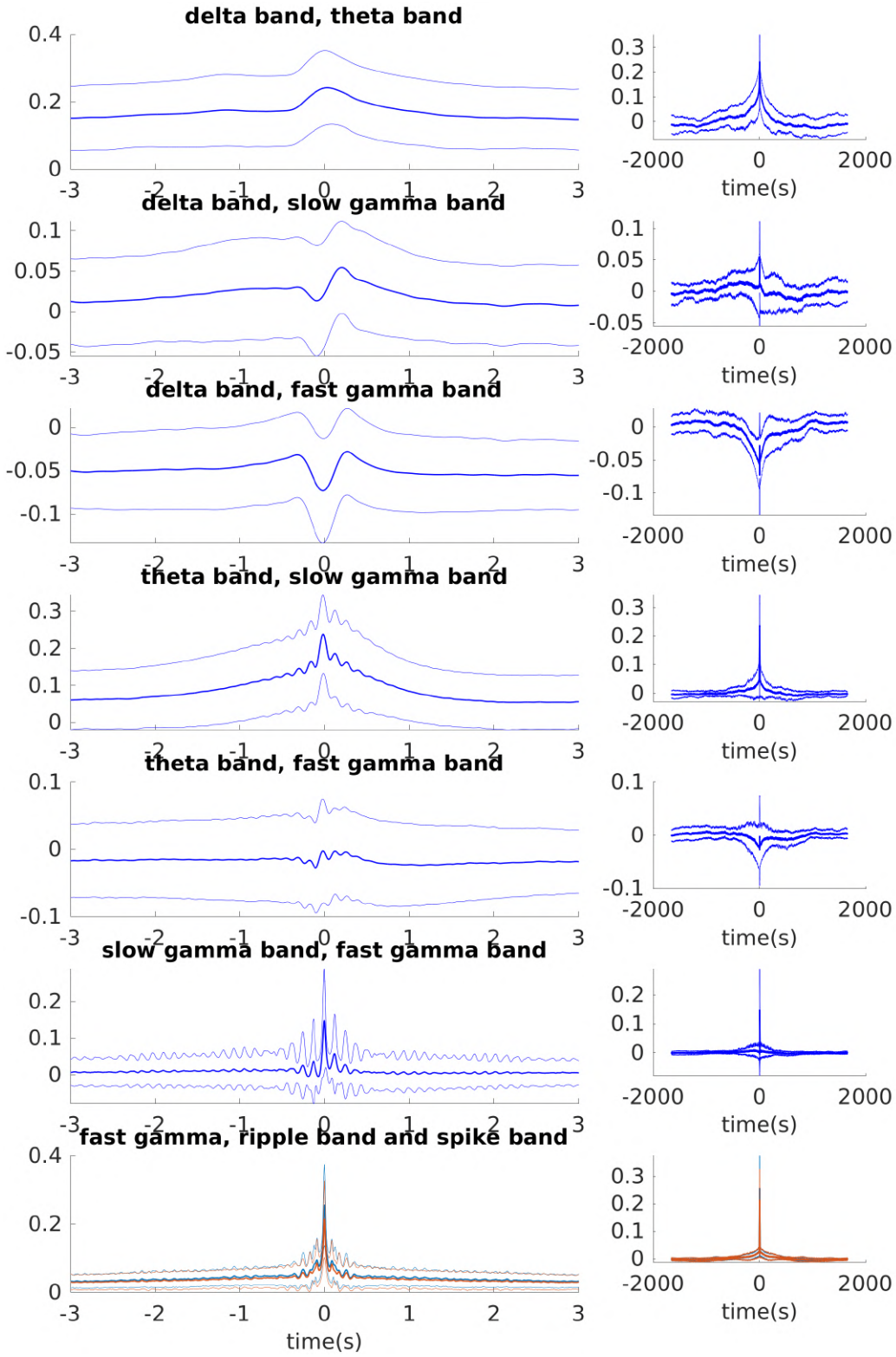

Figure 8.4: Average cross-correlation of Hilbert transform amplitude for several frequency bands.

Chapter 9

IsUDS in the membrane potential during Urethane anesthesia

9.1 Introduction

Do the Infra-slow up down states occur in all behavioral states?

To address this we investigated data from anesthetized animals. Mice were lightly anesthetized with urethane and then head fixed. Membrane potential of several individual neurons from the parietal and frontal cortices was measured using whole-cell patch clamp. Simultaneously, the LFP was measured from a nearby region to estimate the ensemble signatures of single neuron responses. Neurons were filled with biocytin and their anatomical localization and identities confirmed. Anesthesia was delivered only once at the beginning of the experiment (barring rare cases when mice started to wake up). During the electrophysiological measurements, mice were kept in a quiet room without any clear external stimuli.

9.2 Results

Classical up and down states have different dynamics in slow-wave sleep and different levels of anesthesia (Torao-Angosto et al., 2021). Here the data show clear up down states structure and with varied durations, consistent with classic findings. The Hidden Markov Model Inference method proposed by McFarland et al. (2011) was used to identify up-down states. An example dataset illustrating these dynamics is presented in Figure 9.1. Furthermore, Figure 9.2 illustrates the states duration of the up and down states for the example data. It is evident from the figure that the duration of the down states exhibits substantial variation.

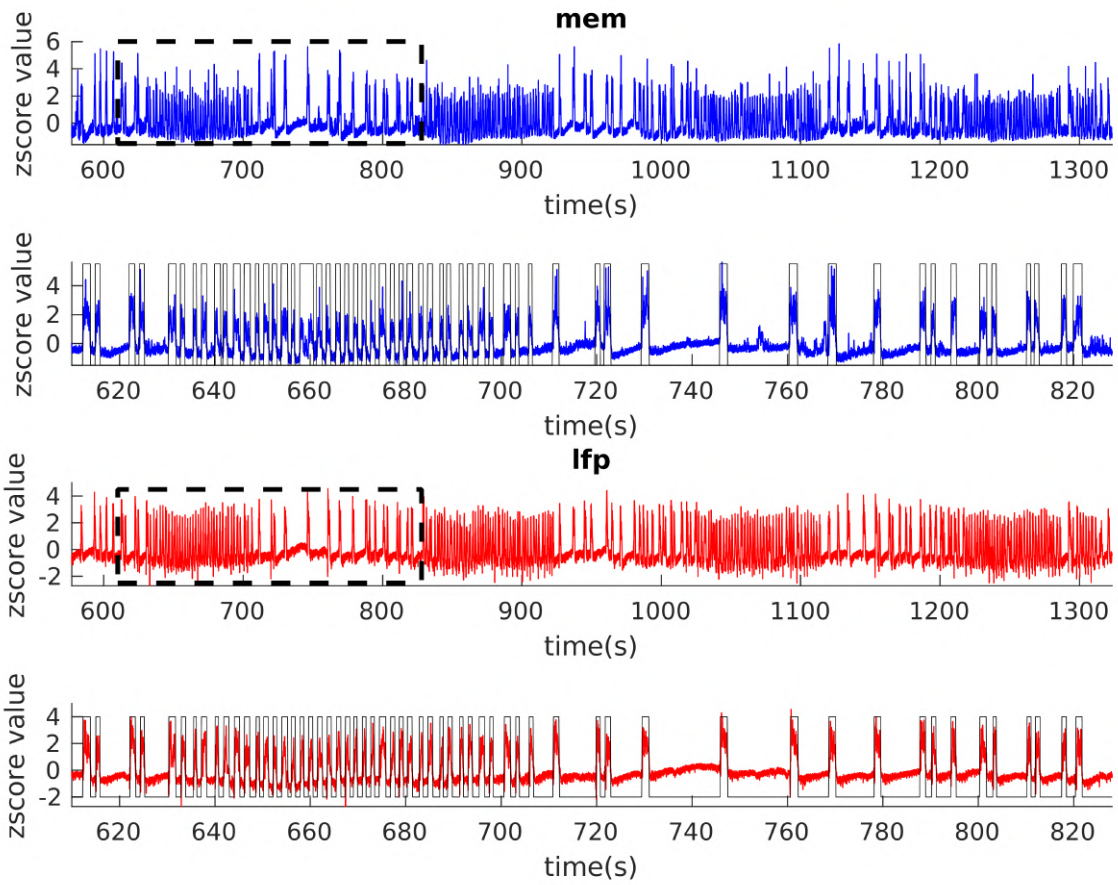

Figure 9.1: Example Membrane potential and local field potential from anesthetized animals. The top two rows represent the membrane potential data, while the second row specifically shows a portion of the data extracted from the rectangular box in the first row. The bottom two rows represent LFP. The up and down states were denoted by black lines in the second and fourth rows.

Autocorrelation and power spectrum analysis revealed the presence of IsUDS oscillations in various forms, including upper envelope, lower envelope, up state duration, down state duration, state duration, up/down duration ratio, and up/state duration ratio, results shown in Figure 9.3. Autocorrelation was obtained with MATLAB function autocorr from Econometrics Toolbox. Power spectrum was obtained with MATLAB function mtspectrumc from chronux toolbox (with parameter pad=2 and tapers=[3 1], http://www.chronux.org).

The upper envelope was derived by taking the maximum value within each up state. To obtain the lower envelope, the up states were replaced with NaN values, which were then filled using the MATLAB "fillmissing" function with the nearest available value. State duration was calculated by summing the up state duration

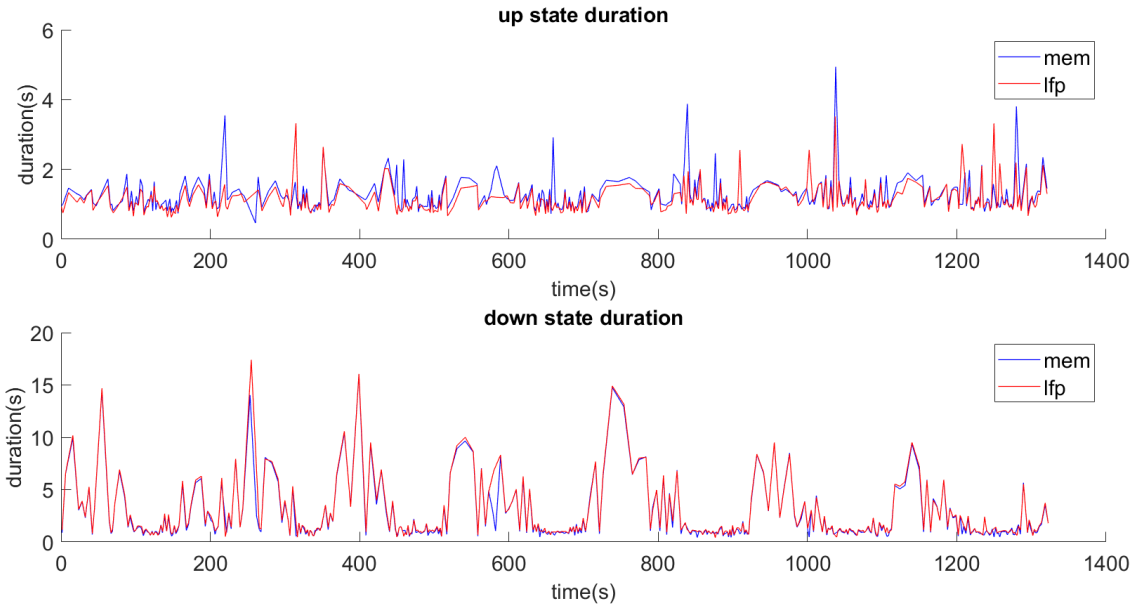

Figure 9.2: Up down states duration.

with the backward following down state duration. The up/down duration ratio was obtained by dividing the up state duration by the duration of the subsequent down state. Similarly, the up/state duration ratio was calculated by dividing the up state duration by the total state duration it belongs to.

To assess the significance of the infra-slow oscillation, we shuffled the data by shuffling the up states and down states. Up states and down states were shuffled independently, then the shuffled up and down states were regrouped together by the shuffled index such that each shuffled up state was paired with a shuffled down state. The raw LFP and MEM data, upper envelope, and lower envelope were shuffled following this shuffle of up and down states. The shuffling process was repeated 50 times per dataset.

Zscored autocorrelation and zsored power spectrum were calculated as below,

Zscored autocorrelation = (raw data autocorrelation - mean(shuffled data autocorrelation))/std(shuffled data autocorrelation)

Zscored power spectrum = (raw data power spectrum - mean(shuffled data power spectrum))/std(shuffled data power spectrum)

Zscored autocorrelation and zscored power spectrum of the data mentioned above are shown in Figure 9.4. The IsUDS manifests in various distinct forms. Clear IsUDS with around 200s period is clear in all of them. For instance, in the case of down state duration, the membrane potential in red exhibits its first peak in autocorrelation at

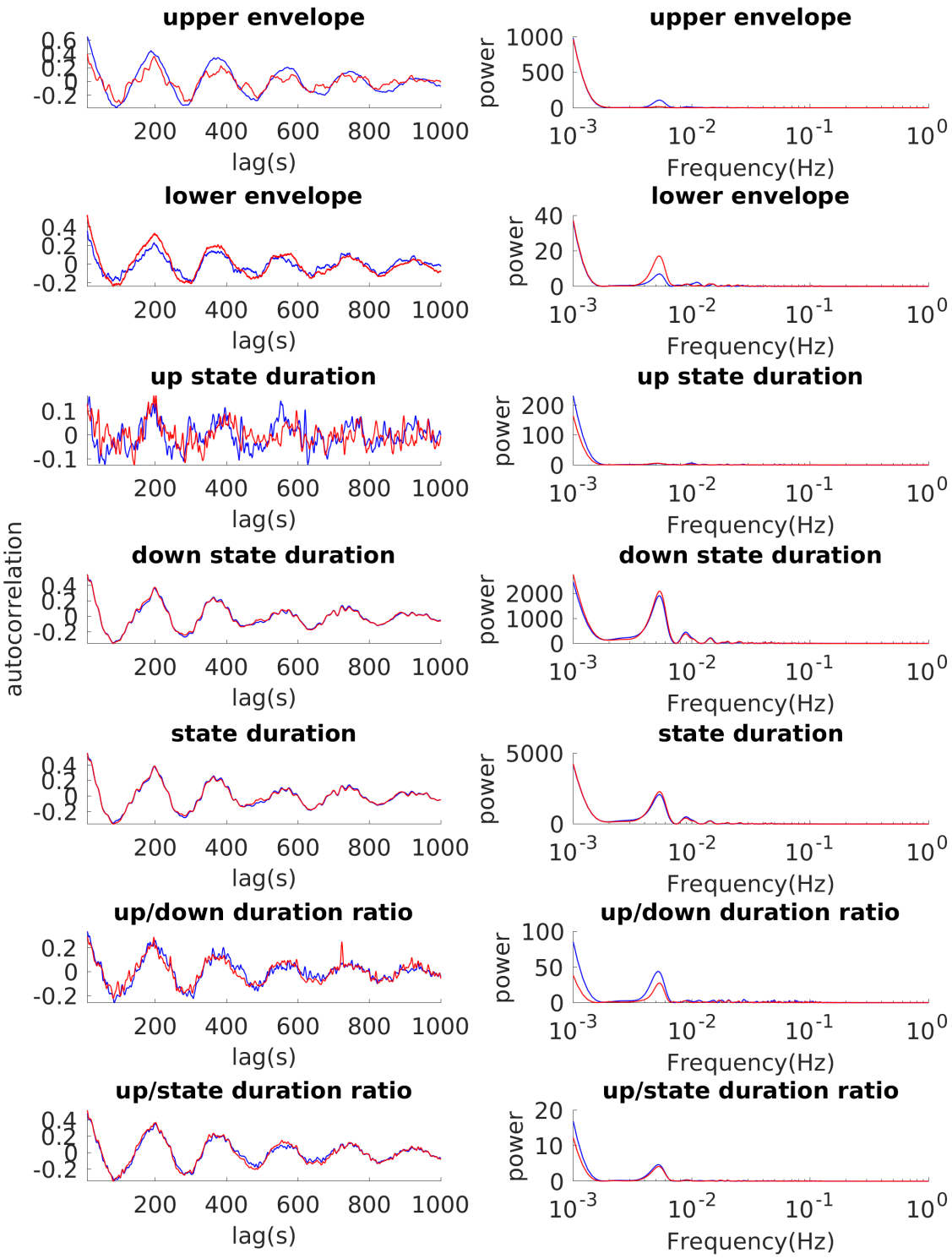

Figure 9.3: Autocorrelation and power spectrum for data from anesthetized animals.

a lag of 196.225s, which deviates by 7.81 standard deviations from the mean shuffled value. Similarly, the LFP in blue displays its first peak in autocorrelation at a lag of

198.547s, with a deviation of 6.92 standard deviations from the mean shuffled value.

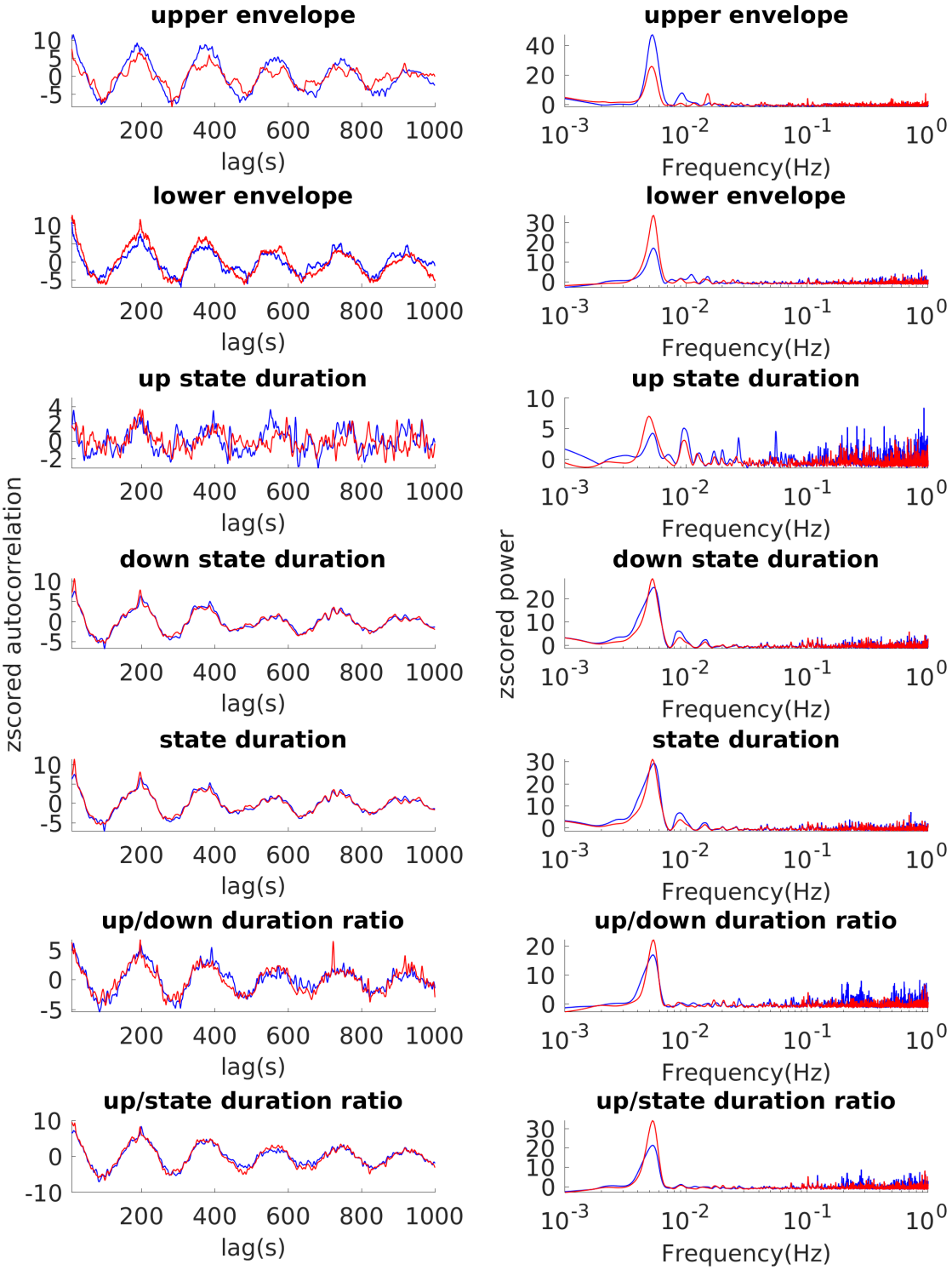

Figure 9.4: Zscored autocorrelation and power spectrum.

To confirm the widespread occurrence of IsUDS oscillations, a substantial amount

of data was analyzed. The dataset included 33 membrane potential recordings from pyramidal neurons, with 15 from the parietal cortex, 6 from the frontal cortex, and 12 from the prefrontal cortex. Additionally, there were 241 LFP recordings, all obtained from the parietal cortex.

The same method as mentioned above was applied to these datasets. The results, shown in Figure 9.5 for membrane potential and Figure 9.6 for LFP, confirm that IsUDS oscillations are a prevalent phenomenon.

Both Figure 9.5 and Figure 9.6 feature thick blue lines in the left two columns, representing the mean values, and thin blue lines indicating one standard error away from the mean value. The red lines in the figures represent the median values. The power spectrum plots in the middle column are labeled with the peak frequency and its corresponding z-scored value. The right column displays the peak value of z-scored power within the IsUDS range along with their corresponding periods.

The same cross-correlation analysis used in the last chapter for different frequency bands, as depicted in Figure 9.7 for membrane potential, indicates that all frequency bands are coupled.

9.3 Conclusion

In anesthetized animals, IsUDS manifest in several forms, encompassing upper envelope, lower envelope, up state duration, down state duration, state duration, up/down duration ratio, and up/state duration ratio.

The analysis of different frequency bands reveals that they are all interconnected and coupled together.

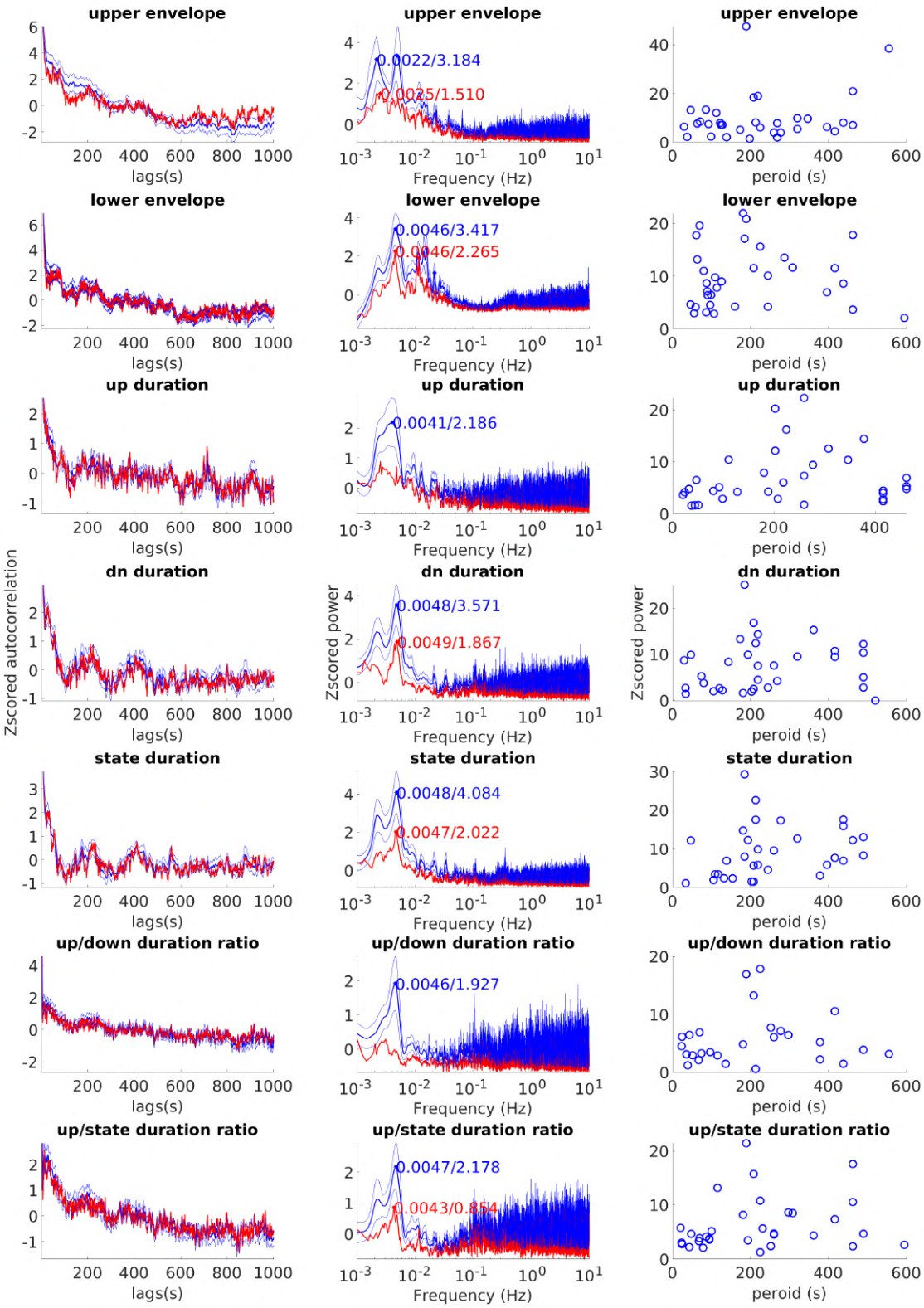

Figure 9.5: Average from 33 membrane potential recordings.

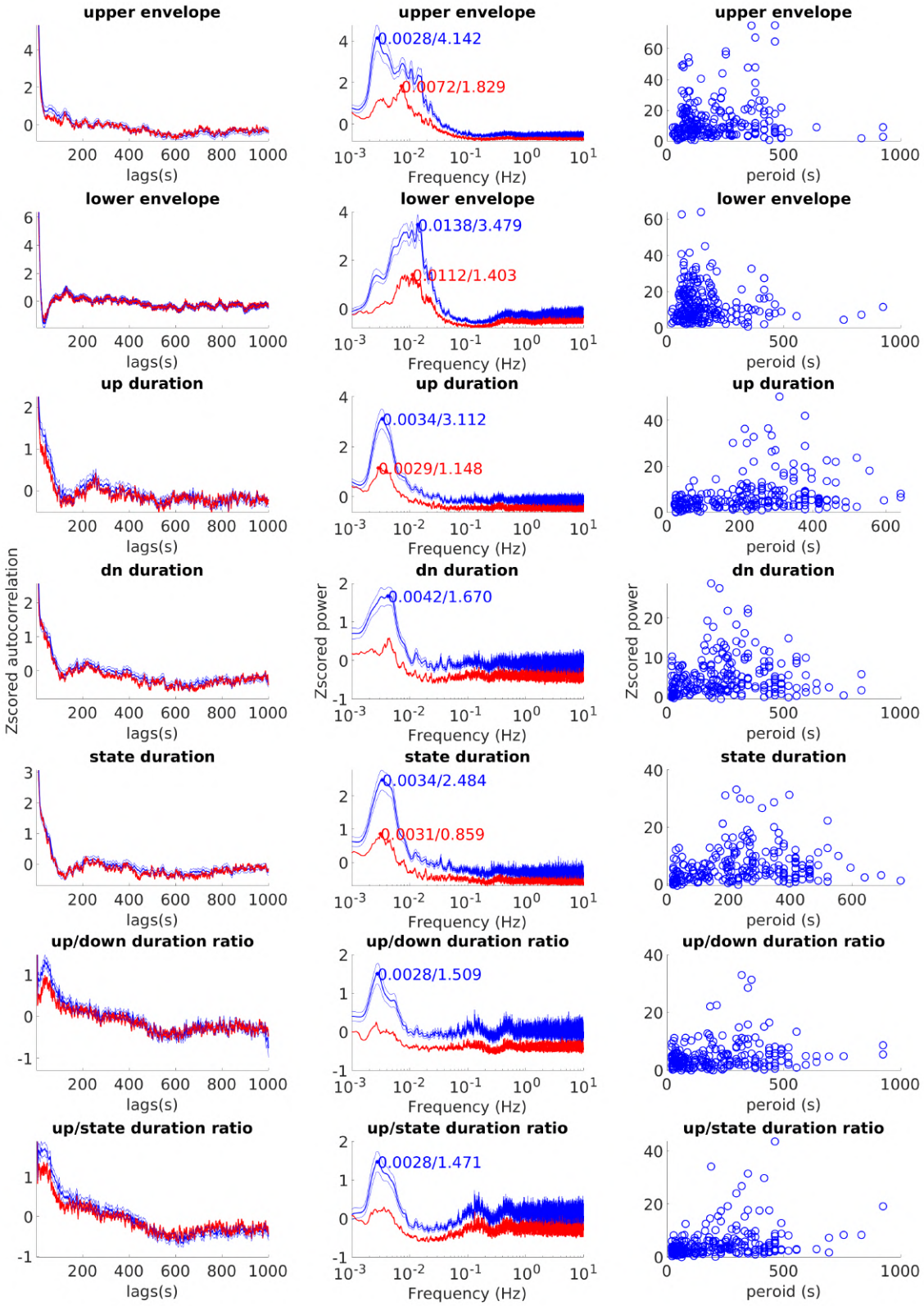

Figure 9.6: Average from 241 LFP recordings.

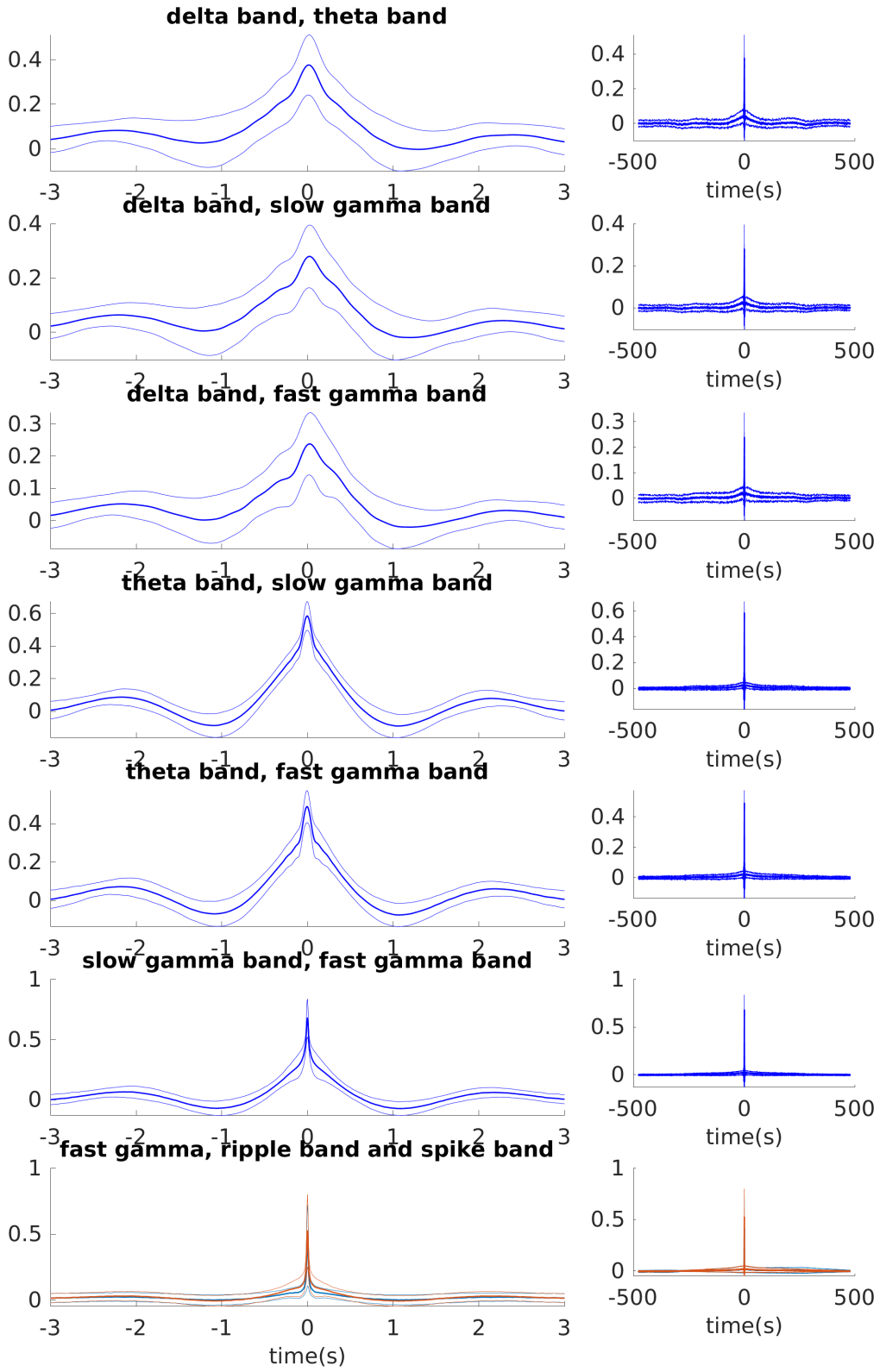

Figure 9.7: Average cross-correlation of Hilbert transform amplitude for several frequency bands.

Chapter 10

Conclusions

Brian spatial cognition is a branch of cognitive science that focuses on the acquisition, organization, and utilization of information about external spatial environments (Waller, Nadel, 2012).

Spatial information can be divided into several primitives, such as location, distance, direction, and time-related information, among others. From these foundational elements, a wide range of complex spatial concepts can be derived.

The experimental study of spatial cognition in the brain has led to the discovery that many spatial concepts are represented and processed by individual neurons or groups of neurons (Waller, Nadel, 2012; Moser et al., 2017). This has resulted in the introduction of numerous new terms, such as place cells (O'Keefe, Dostrovsky, 1971), head direction cells (Ranck, 1984), grid cells (Fyhn et al., 2004; Hafting et al., 2005), speed cells (Kropff et al., 2015), and others.

In recent research, significant progress has been made in spatial cognition research, particularly with a strong emphasis on studying the hippocampus and its related areas (Waller, Nadel, 2012; Moser et al., 2017; Hardcastle et al., 2017). The hippocampus, located deep within the brain as an allocortex region, has gained widespread attention in spatial cognition studies for two primary reasons. Firstly, it has a three-layer structure and a simplified neuron connection architecture. Secondly, it accommodates various cell types that encode spatial concepts commonly used in our everyday lives, including location, direction, speed, and time. Place cells (O'Keefe, Dostrovsky, 1971) and grid cells (Fyhn et al., 2004; Hafting et al., 2005) were first described in the hippocampus and one synaptic away from the hippocampus.

In this thesis work, the initial focus lies in investigating certain aspects of spatial information encoding exhibited by these cell types.

First (in Chapter 4), we modeled the burrow environment based on the detailed quantitative descriptions by John Calhoun (Calhoun, 1962), and we let a virtual

rat randomly explore it; then using our self-organizing adaptation model which we observed grid pattern formation in model units (Kropff, Treves, 2008; Si, Treves, 2013). Grid units can form a stable representation of the entire environment but they acquire the information slowly. Undoubtedly, less explored sub-environments perform less effectively and are often represented by vague or unclear maps. The small size of chambers in natural burrows poses a challenge, limiting grid units to express only a few fields. This challenge questions the notion that grid cells can exhibit long-range order beyond laboratory conditions. As expected, this characteristic signature was not observed in the limited and non-flat vowel space (Kaya et al., 2020). Of course, it is essential to acknowledge that there may be various other reasons for a null result.

Then in Chapter 5, we aim to establish a correlation between the anchoring of grid cells to the environment and the distortion observed in irregular environments with the patterns of environment exploration behavior. Recent discoveries suggest that grid cells are not only involved in encoding global spatial information but also play a role in encoding local information. One notable observation regarding the anchoring of grid patterns to the environment is that the grid axis remains fixed at a 7.5-degree angle from the wall in a square space (Stensola et al., 2015; Julian et al., 2018). First of all, by analyzing behavior data from rats exploring square enclosures, we have identified several exploration patterns. Rats tend to move at a slower speed when traveling in a direction perpendicular to the walls, but their speed increases when moving along the walls. Additionally, when running near the walls, rats exhibit a preference for either clockwise or counterclockwise movement along the walls. We then simulated a virtual rat, incorporating the exploration patterns discussed above, and used the self-organization model (Kropff, Treves, 2008; Si, Treves, 2013) to simulate the formation of grid patterns. Upon making slight adjustments to the exploration pattern, we observed corresponding variations in the anchored grid patterns within the environment which include the 7.5-degree boundary anchoring. Next, we delve into the issue of grid pattern distortion in irregularly shaped environments, such as trapezoids, as discussed in previous studies (Krupic et al., 2014, 2015, 2018). By merely reducing the frequency of direction changes in the virtual rat's movements to enhance long-range correlation in the self-organization model, the grid pattern shows distinctive distortion patterns based on the environment shape. Intriguingly, this phenomenon remains consistent even when employing a realistic foraging strategy known as Lévy flight.

Chapter 6, based on the facts that the accumulation of properties and discoveries related to grid cells has led to disagreements and challenges in defining and

understanding the concept of "grid cells." When discussing "grid cells," there is a higher probability of encountering divergent interpretations and mismatched concepts regarding what "grid cells" truly represent. In this regard, here in this chapter, we describe the encoding properties of grid cells with a simplified self-organization model. And the two major encoding properties of grid cells are described with simulations: the number of encoding fields per grid cell and the emergence of regularity in their spatial firing patterns. The number of encoding fields each encoding unit has is positively correlated with the sparsity of the ensemble. Regularity emerges when the units have proper sparsity, allowing them to have several fields and engage in appropriate competition with other local units.

The second part of this thesis starts from chapter 7 to chapter 9, our focus shifted to brain oscillations, which also play a significant role in representing the regularity of brain activity (Buzsáki, 2006). Specifically, we delved into the study of infra slow oscillations in freely behaving rats, as well as in anesthetized rats.

In Chapter 7, from the data recorded from freely behaving rats, infraslow up-down states (IsUDS) range oscillations of approximately several hundred seconds were evident and clear. The IsUDS of the LFP amplitude is largely driven by fluctuations in the delta oscillation magnitude. The amplitude of IsUDS in the LFP and the delta band filtered LFP display a bimodal distribution, resembling the characteristic pattern observed in classic up-and-down states. Then we refer to this infra slow oscillation as infra slow up down states (IsUDS). The transition into the high-amplitude LFP and theta band filtered LFP occurred gradually, with a slow change. However, the transition from the high amplitude to the low amplitude was relatively abrupt and occurred rapidly. In addition to the IsUDS frequencies, the signal also encompasses numerous higher frequencies beyond the typical range associated with IsUDS activity. The simultaneous firing pattern of neurons, comprising both pyramidal neurons and interneurons, displays periodic correlations with IsUDS oscillation. However, even within the same cell types, these correlations occur with diverse phase shifts.

In Chapter 8, we show that IsUDS in several frequency bands exhibit bimodality, which is characterized by a relatively abrupt transition between high and low values. Furthermore, different frequency bands display distinct coupling structures.

In Chapter 9, we conducted an analysis of infra slow oscillations in anesthetized rats. These oscillations manifest in various forms, including upper envelope, lower envelope, up state duration, down state duration, state duration, up/down duration ratio, and up/state duration ratio. Furthermore, the different frequency bands are all coupled together.

Bibliography

Aladjalova N. A. Infra-Slow Rhythmic Oscillations of The Steady Potential of the Cerebral Cortex // Nature. V 1957. 179, 4567. 957–959.

Andersen Per, Richard Morris, Amaral David, Bliss Tim, John O'Keefe . The Hippocampus Book. 2007.

Aronov Dmitriy, Nevers Rhino, Tank David W. Mapping of a Non-Spatial Dimension by the Hippocampal–Entorhinal Circuit // Nature. III 2017. 543, 7647. 719–722.

Bannerman D. M, Rawlins J. N. P, McHugh S. B, Deacon R. M. J, Yee B. K, Bast T, Zhang W. N, Pothuizen H. H. J, Feldon J. Regional Dissociations within the Hippocampus—Memory and Anxiety // Neuroscience & Biobehavioral Reviews. Festschrift in Honour of Jeffrey Gray - Issue 1: Anxiety and Neuroticism. V 2004. 28, 3. 273–283.

Barry Caswell, Hayman Robin, Burgess Neil, Jeffery Kathryn J. Experience-Dependent Rescaling of Entorhinal Grids // Nature Neuroscience. VI 2007. 10, 6. 682–684.

Bartumeus Frederic, Da Luz M. G. E., Viswanathan G. M., Catalan J. Animal Search Strategies: A Quantitative Random-Walk Analysis // Ecology. 2005. 86, 11. 3078–3087.

Bellmund Jacob L. S., Gärdenfors Peter, Moser Edvard I., Doeller Christian F. Navigating Cognition: Spatial Codes for Human Thinking // Science. XI 2018. 362, 6415. eaat6766.

Bellmund Jacob L. S., de Cothi William, Ruiter Tom A., Nau Matthias, Barry Caswell, Doeller Christian F. Deforming the Metric of Cognitive Maps Distorts Memory // Nature Human Behaviour. II 2020. 4, 2. 177–188.

Boccara Charlotte N., Nardin Michele, Stella Federico, O'Neill Joseph, Csicsvari Jozsef. The Entorhinal Cognitive Map Is Attracted to Goals // Science. III 2019. 363, 6434. 1443–1447.

Borckmans P., Dewel G., De Wit A., Dulos E., Boissonade J., Gauffre F., De Kepper P. Diffusive Instabilities and Chemical Reactions // International Journal of Bifurcation and Chaos. XI 2002. 12, 11. 2307–2332.

Bostock E., Muller R. U., Kubie J. L. Experience-Dependent Modifications of Hippocampal Place Cell Firing // Hippocampus. IV 1991. 1, 2. 193–205.

Bueno-Junior Lezio S., Ruckstuhl Maxwell S., Lim Miranda M., Watson Brendon O. The Temporal Structure of REM Sleep Shows Minute-Scale Fluctuations across Brain and Body in Mice and Humans // Proceedings of the National Academy of Sciences. V 2023. 120, 18. e2213438120.

Burak Yoram, Fiete Ila R. Accurate Path Integration in Continuous Attractor Network Models of Grid Cells // PLOS Comput Biol. II 2009. 5, 2. e1000291.

Burgess Neil. Grid Cells and Theta as Oscillatory Interference: Theory and Predictions // Hippocampus. 2008. 18, 12. 1157–1174.

Burgess Neil, Barry Caswell. An Oscillatory Interference Model of Grid Cell Firing // Hippocampus. 2007. 17, 9. 801–812.

Busch Niko A., Dubois Julien, VanRullen Rufin. The Phase of Ongoing EEG Oscillations Predicts Visual Perception // Journal of Neuroscience. VI 2009. 29, 24. 7869–7876.

Buzsáki György. Rhythms of the Brain. xv. New York, NY, US: Oxford University Press, 2006.

Buzsáki György, Draguhn Andreas. Neuronal Oscillations in Cortical Networks // Science. VI 2004. 304, 5679. 1926–1929.

Buzsáki György, Tingley David. Space and Time: The Hippocampus as a Sequence Generator // Trends in Cognitive Sciences. X 2018. 22, 10. 853–869.

Calhoun John B. The Ecology and sociology of the Norway Rat. 1962.

Carpenter Francis, Manson Daniel, Jeffery Kate, Burgess Neil, Barry Caswell. Grid Cells Form a Global Representation of Connected Environments // Current Biology. V 2015. 25, 9. 1176–1182.

Castro Luísa, Aguiar Paulo. A Feedforward Model for the Formation of a Grid Field Where Spatial Information Is Provided Solely from Place Cells // Biological Cybernetics. IV 2014. 108, 2. 133–143.

Cogno Soledad Gonzalo, Obenhaus Horst A., Jacobsen Ragnhild Irene, Donato Flavio, Moser May-Britt, Moser Edvard I. Minute-Scale Oscillatory Sequences in Medial Entorhinal Cortex. V 2022. 2022.05.02.490273.

Cole Scott R., Voytek Bradley. Brain Oscillations and the Importance of Waveform Shape // Trends in Cognitive Sciences. II 2017. 21, 2. 137–149.

Couey Jonathan J., Witoelar Aree, Zhang Sheng-Jia, Zheng Kang, Ye Jing, Dunn Benjamin, Czajkowski Rafal, Moser May-Britt, Moser Edvard I., Roudi Yasser, Witter Menno P. Recurrent Inhibitory Circuitry as a Mechanism for Grid Formation // Nature Neuroscience. III 2013. 16, 3. 318–324.

D'Albis Tiziano, Kempter Richard. Recurrent Amplification of Grid-Cell Activity // Hippocampus. 2020. 30, 12. 1268–1297.

Dash Michael B. Infraslow Coordination of Slow Wave Activity through Altered Neuronal Synchrony // Sleep. XII 2019. 42, 12. zsz170.

Davidson Thomas J., Kloosterman Fabian, Wilson Matthew A. Hippocampal Replay of Extended Experience // Neuron. VIII 2009. 63, 4. 497–507.

Derdikman Dori, Whitlock Jonathan R., Tsao Albert, Fyhn Marianne, Hafting Torkel, Moser May-Britt, Moser Edvard I. Fragmentation of Grid Cell Maps in a Multicompartment Environment // Nature Neuroscience. X 2009. 12, 10. 1325–1332.

DiTullio Ronald W., Balasubramanian Vijay. Dynamical Self-Organization and Efficient Representation of Space by Grid Cells // Current Opinion in Neurobiology. Computational Neuroscience. X 2021. 70. 206–213.

Diba Kamran, Buzsáki György. Forward and Reverse Hippocampal Place-Cell Sequences during Ripples // Nature Neuroscience. X 2007. 10, 10. 1241–1242.

Diehl Geoffrey W., Hon Olivia J., Leutgeb Stefan, Leutgeb Jill K. Grid and Nongrid Cells in Medial Entorhinal Cortex Represent Spatial Location and Environmental Features with Complementary Coding Schemes // Neuron. IV 2017. 94, 1. 83–92.e6.

Doeller Christian F., Barry Caswell, Burgess Neil. Evidence for Grid Cells in a Human Memory Network // Nature. II 2010. 463, 7281. 657–661.

Donnarumma Francesco, Prevete Roberto, Maisto Domenico, Fuscone Simone, Irvine Emily M., van der Meer Matthijs A. A., Kemere Caleb, Pezzulo Giovanni. A Framework to Identify Structured Behavioral Patterns within Rodent Spatial Trajectories // Scientific Reports. I 2021. 11, 1. 468.

Eichenbaum H., Kuperstein M., Fagan A., Nagode J. Cue-Sampling and Goal-Approach Correlates of Hippocampal Unit Activity in Rats Performing an Odor-Discrimination Task // Journal of Neuroscience. III 1987. 7, 3. 716–732.

Etienne Ariane S., Jeffery Kathryn J. Path Integration in Mammals // Hippocampus. I 2004. 14, 2. 180–192.

Felleman Daniel J., Van Essen David C. Distributed Hierarchical Processing in the Primate Cerebral Cortex // Cerebral Cortex. I 1991. 1, 1. 1–47.

Fenton André A., Kao Hsin-Yi, Neymotin Samuel A., Olypher Andrey, Vayntrub Yevgeniy, Lytton William W., Ludvig Nandor. Unmasking the CA1 Ensemble Place Code by Exposures to Small and Large Environments: More Place Cells and Multiple, Irregularly Arranged, and Expanded Place Fields in the Larger Space // The Journal of Neuroscience. X 2008. 28, 44. 11250–11262.

Fiete Ila R., Burak Yoram, Brookings Ted. What Grid Cells Convey about Rat Location // Journal of Neuroscience. VII 2008. 28, 27. 6858–6871.

Foster David J., Wilson Matthew A. Reverse Replay of Behavioural Sequences in Hippocampal Place Cells during the Awake State // Nature. III 2006. 440, 7084. 680–683.

Frank Loren M., Stanley Garrett B., Brown Emery N. Hippocampal Plasticity across Multiple Days of Exposure to Novel Environments // The Journal of Neuroscience: The Official Journal of the Society for Neuroscience. IX 2004. 24, 35. 7681–7689.

Fries Pascal. Rhythms for Cognition: Communication through Coherence // Neuron. X 2015. 88, 1. 220–235.

Fuhs Mark C., Touretzky David S. A Spin Glass Model of Path Integration in Rat Medial Entorhinal Cortex // The Journal of Neuroscience: The Official Journal of the Society for Neuroscience. IV 2006. 26, 16. 4266–4276.

Fyhn Marianne, Hafting Torkel, Treves Alessandro, Moser May-Britt, Moser Edvard I. Hippocampal Remapping and Grid Realignment in Entorhinal Cortex // Nature. III 2007. 446, 7132. 190–194.

Fyhn Marianne, Hafting Torkel, Witter Menno P., Moser Edvard I., Moser May-Britt. Grid Cells in Mice // Hippocampus. XII 2008. 18, 12. 1230–1238.

Fyhn Marianne, Molden Sturla, Witter Menno P., Moser Edvard I., Moser May-Britt. Spatial Representation in the Entorhinal Cortex // Science. VIII 2004. 305, 5688. 1258–1264.

Gerlei Klara, Passlack Jessica, Hawes Ian, Vandrey Brianna, Stevens Holly, Papastathopoulos Ioannis, Nolan Matthew F. Grid Cells Are Modulated by Local Head Direction // Nature Communications. VIII 2020. 11, 1. 4228.

Ginosar Gily, Aljadeff Johnatan, Burak Yoram, Sompolinsky Haim, Las Liora, Ulanovsky Nachum. Locally Ordered Representation of 3D Space in the Entorhinal Cortex // Nature. VIII 2021. 596. 404–409.

Ginosar Gily, Aljadeff Johnatan, Las Liora, Derdikman Dori, Ulanovsky Nachum. Are Grid Cells Used for Navigation? On Local Metrics, Subjective Spaces, and Black Holes // Neuron. IV 2023. 0, 0.

Giocomo Lisa M., Hussaini Syed A., Zheng Fan, Kandel Eric R., Moser May-Britt, Moser Edvard I. Grid Cells Use HCN1 Channels for Spatial Scaling // Cell. XI 2011a. 147, 5. 1159–1170.

Giocomo Lisa M., Moser May-Britt, Moser Edvard I. Computational Models of Grid Cells // Neuron. VIII 2011b. 71, 4. 589–603.

Giocomo Lisa M., Zilli Eric A., Fransén Erik, Hasselmo Michael E. Temporal Frequency of Subthreshold Oscillations Scales with Entorhinal Grid Cell Field Spacing // Science (New York, N.Y.). III 2007. 315, 5819. 1719–1722.

Gofman Xenia, Tocker Gilad, Weiss Shahaf, Boccara Charlotte N., Lu Li, Moser May-Britt, Moser Edvard I., Morris Genela, Derdikman Dori. Dissociation between

Postrhinal Cortex and Downstream Parahippocampal Regions in the Representation of Egocentric Boundaries // Current Biology. VIII 2019. 29, 16. 2751–2757.e4.

Gothard Katalin M., Hoffman Kari L., Battaglia Francesco P., McNaughton Bruce L. Dentate Gyrus and CA1 Ensemble Activity during Spatial Reference Frame Shifts in the Presence and Absence of Visual Input // Journal of Neuroscience. IX 2001. 21, 18. 7284–7292.

Grieves Roddy M., Jedidi-Ayoub Selim, Mishchanchuk Karyna, Liu Anyi, Renaudineau Sophie, Duvelle Éléonore, Jeffery Kate J. Irregular Distribution of Grid Cell Firing Fields in Rats Exploring a 3D Volumetric Space // Nature Neuroscience. XI 2021. 24, 11. 1567–1573.

Grieves Roddy M., Jedidi-Ayoub Selim, Mishchanchuk Karyna, Liu Anyi, Renaudineau Sophie, Jeffery Kate J. The Place-Cell Representation of Volumetric Space in Rats // Nature Communications. II 2020. 11, 1. 789.

Grossberg Stephen, Pilly Praveen K. How Entorhinal Grid Cells May Learn Multiple Spatial Scales from a Dorsoventral Gradient of Cell Response Rates in a Self-organizing Map // PLoS Computational Biology. X 2012. 8, 10.

Gupta Anoopum S., van der Meer Matthijs A. A., Touretzky David S., Redish A. David. Hippocampal Replay Is Not a Simple Function of Experience // Neuron. III 2010. 65, 5. 695–705.

Hafting Torkel, Fyhn Marianne, Bonnevie Tora, Moser May-Britt, Moser Edvard I. Hippocampus-Independent Phase Precession in Entorhinal Grid Cells // Nature. VI 2008. 453, 7199. 1248–1252.

Hafting Torkel, Fyhn Marianne, Molden Sturla, Moser May-Britt, Moser Edvard I. Microstructure of a Spatial Map in the Entorhinal Cortex // Nature. VIII 2005. 436, 7052. 801–806.

Hampson Robert E., Heyser Charles J., Deadwyler Sam A. Hippocampal Cell Firing Correlates of Delayed-Match-to-Sample Performance in the Rat // Behavioral Neuroscience. 1993. 107, 5. 715–739.

Hardcastle Kiah, Ganguli Surya, Giocomo Lisa M. Cell Types for Our Sense of Location: Where We Are and Where We Are Going // Nature Neuroscience. XI 2017. 20, 11. 1474–1482.

Harland Bruce, Contreras Marco, Souder Madeline, Fellous Jean-Marc. Dorsal CA1 Hippocampal Place Cells Form a Multi-Scale Representation of Megaspace // Current Biology. V 2021. 31, 10. 2178–2190.e6.

Hasselmo Michael E., Brandon Mark P. Linking Cellular Mechanisms to Behavior: Entorhinal Persistent Spiking and Membrane Potential Oscillations May Underlie Path Integration, Grid Cell Firing, and Episodic Memory // Neural Plasticity. VII 2008. 2008. e658323.

Hasselmo Michael E., Giocomo Lisa M., Zilli Eric A. Grid Cell Firing May Arise from Interference of Theta Frequency Membrane Potential Oscillations in Single Neurons // Hippocampus. 2007. 17, 12. 1252–1271.

Herzog Linnea E., Pascual Leila May, Scott Seneca J., Mathieson Elon R., Katz Donald B., Jadhav Shantanu P. Interaction of Taste and Place Coding in the Hippocampus // Journal of Neuroscience. IV 2019. 39, 16. 3057–3069.

Hinman James R., Chapman G. William, Hasselmo Michael E. Neuronal Representation of Environmental Boundaries in Egocentric Coordinates // Nature Communications. VI 2019. 10, 1. 2772.

Hubel D. H., Wiesel T. N. Receptive Fields of Single Neurones in the Cat's Striate Cortex // The Journal of Physiology. X 1959. 148, 3. 574–591.

Hubel David H, Wiesel Torsten N. Early Exploration of the Visual Cortex // Neuron. III 1998. 20, 3. 401–412.

Ismakov Revekka, Barak Omri, Jeffery Kate, Derdikman Dori. Grid Cells Encode Local Positional Information // Current Biology. VIII 2017. 27, 15. 2337–2343.e3.

Jacobs Joshua, Weidemann Christoph T., Miller Jonathan F., Solway Alec, Burke John F., Wei Xue-Xin, Suthana Nanthia, Sperling Michael R., Sharan Ashwini D., Fried Itzhak, Kahana Michael J. Direct Recordings of Grid-like Neuronal Activity in Human Spatial Navigation // Nature Neuroscience. IX 2013. 16, 9. 1188–1190.

Jensen Ole, Kaiser Jochen, Lachaux Jean-Philippe. Human Gamma-Frequency Oscillations Associated with Attention and Memory // Trends in Neurosciences. VII 2007. 30, 7. 317–324.

Julian Joshua B., Keinath Alexandra T., Frazzetta Giulia, Epstein Russell A. Human Entorhinal Cortex Represents Visual Space Using a Boundary-Anchored Grid // Nature Neuroscience. I 2018. 21, 2. 191–194.

Jung M. W., Wiener S. I., McNaughton B. L. Comparison of Spatial Firing Characteristics of Units in Dorsal and Ventral Hippocampus of the Rat // Journal of Neuroscience. XII 1994. 14, 12. 7347–7356.

Karlsson Mattias P., Frank Loren M. Awake Replay of Remote Experiences in the Hippocampus // Nature Neuroscience. VII 2009. 12, 7. 913–918.

Karsenti Eric. Self-Organization in Cell Biology: A Brief History // Nature Reviews Molecular Cell Biology. III 2008. 9, 3. 255–262.

Kaya Zeynep, Soltanipour Mohammadreza, Treves Alessandro. Non-Hexagonal Neural Dynamics in Vowel Space // AIMS Neuroscience. 2020. 7, neurosci-07-03-015. 275–298.

Kentros Clifford, Hargreaves Eric, Hawkins Robert D., Kandel Eric R., Shapiro Matthew, Muller Robert V. Abolition of Long-Term Stability of New Hippocampal Place Cell Maps by NMDA Receptor Blockade // Science. VI 1998. 280, 5372. 2121–2126.

Killian Nathaniel J., Jutras Michael J., Buffalo Elizabeth A. A Map of Visual Space in the Primate Entorhinal Cortex // Nature. XI 2012. 491, 7426. 761–764.

Kjelstrup Kirsten Brun, Solstad Trygve, Brun Vegard Heimly, Hafting Torkel, Leutgeb Stefan, Winter Menno P., Moser Edvard I., Moser May-Britt. Finite Scale of Spatial Representation in the Hippocampus // Science. 2008. 321, 5885. 140–143.

Kloosterman Fabian, Van Haeften Theo, Witter Menno P., Lopes Da Silva Fernando H. Electrophysiological Characterization of Interlaminar Entorhinal Connections: An Essential Link for Re-Entrance in the Hippocampal-Entorhinal System // The European Journal of Neuroscience. XII 2003. 18, 11. 3037–3052.

Kloosterman Fabian, van Haeften Theo, Lopes da Silva Fernando H. Two Reentrant Pathways in the Hippocampal-Entorhinal System // Hippocampus. 2004. 14, 8. 1026–1039.

Knierim James J., McNaughton Bruce L. Hippocampal Place-Cell Firing During Movement in Three-Dimensional Space // Journal of Neurophysiology. I 2001. 85, 1. 105–116.

Kropff Emilio, Carmichael James E., Moser May-Britt, Moser Edvard I. Speed Cells in the Medial Entorhinal Cortex // Nature. VII 2015. 523, 7561. 419–424.

Kropff Emilio, Treves Alessandro. The Emergence of Grid Cells: Intelligent Design or Just Adaptation? // Hippocampus. XII 2008. 18, 12. 1256–1269.

Krupic Julija, Bauza Marius, Burton Stephen, Barry Caswell, O'Keefe John. Grid Cell Symmetry Is Shaped by Environmental Geometry // Nature. II 2015. 518, 7538. 232–235.

Krupic Julija, Bauza Marius, Burton Stephen, Lever Colin, O'Keefe John. How Environment Geometry Affects Grid Cell Symmetry and What We Can Learn from It // Philosophical Transactions of the Royal Society B: Biological Sciences. II 2014. 369, 1635. 20130188.

Krupic Julija, Bauza Marius, Burton Stephen, O'Keefe John. Local Transformations of the Hippocampal Cognitive Map // Science. III 2018. 359, 6380. 1143–1146.

Krupic Julija, Burgess Neil, O'Keefe John. Neural Representations of Location Composed of Spatially Periodic Bands // Science. VIII 2012. 337, 6096. 853–857.

Kubie J. L., Muller R. U. Multiple Representations in the Hippocampus // Hippocampus. VII 1991. 1, 3. 240–242.

Langston Rosamund F., Ainge James A., Couey Jonathan J., Canto Cathrin B., Bjerknes Tale L., Witter Menno P., Moser Edvard I., Moser May-Britt. Development of the Spatial Representation System in the Rat // Science. VI 2010. 328, 5985. 1576–1580.

Lansink Carien S., Goltstein Pieter M., Lankelma Jan V., McNaughton Bruce L., Pennartz Cyriel M. A. Hippocampus Leads Ventral Striatum in Replay of Place-Reward Information // PLOS Biology. VIII 2009. 7, 8. e1000173.

Latuske Patrick, Kornienko Olga, Kohler Laura, Allen Kevin. Hippocampal Remapping and Its Entorhinal Origin // Frontiers in Behavioral Neuroscience. 2018. 11.

Lega Bradley C., Jacobs Joshua, Kahana Michael. Human Hippocampal Theta Oscillations and the Formation of Episodic Memories // Hippocampus. 2012. 22, 4. 748–761.

Leutgeb Jill K., Leutgeb Stefan, Moser May-Britt, Moser Edvard I. Pattern Separation in the Dentate Gyrus and CA3 of the Hippocampus // Science. II 2007. 315, 5814. 961–966.

Lever Colin, Burton Stephen, Jeewajee Ali, O'Keefe John, Burgess Neil. Boundary Vector Cells in the Subiculum of the Hippocampal Formation // Journal of Neuroscience. VIII 2009. 29, 31. 9771–9777.

Lisman John E., Jensen Ole. The Theta-Gamma Neural Code // Neuron. III 2013. 77, 6. 1002–1016.

Long Xiaoyang, Deng Bin, Cai Jing, Chen Zhe Sage, Zhang Sheng-Jia. A Compact Spatial Map in V2 Visual Cortex. II 2021. 2021.02.11.430687.

Long Xiaoyang, Zhang Sheng-Jia. A Novel Somatosensory Spatial Navigation System Outside the Hippocampal Formation // Cell Research. VI 2021. 31, 6. 649–663.

MacDonald Christopher J., Lepage Kyle Q., Eden Uri T., Eichenbaum Howard. Hippocampal "Time Cells" Bridge the Gap in Memory for Discontiguous Events // Neuron. VIII 2011. 71, 4. 737–749.

Marr D., Brindley Giles Skey. Simple Memory: A Theory for Archicortex // Philosophical Transactions of the Royal Society of London. B, Biological Sciences. VII 1971. 262, 841. 23–81.

Marti Louis, Wu Shengyi, Piantadosi Steven T., Kidd Celeste. Latent Diversity in Human Concepts // Open Mind. III 2023. 7. 79–92.

Maurer Andrew P., VanRhoads Shea R., Sutherland Gary R., Lipa Peter, McNaughton Bruce L. Self-Motion and the Origin of Differential Spatial Scaling along the Septo-Temporal Axis of the Hippocampus // Hippocampus. I 2005. 15, 7. 841–852.

McFarland James M., Hahn Thomas T. G., Mehta Mayank R. Explicit-Duration Hidden Markov Model Inference of UP-DOWN States from Continuous Signals // PLOS ONE. VI 2011. 6, 6. e21606.

McNaughton Bruce L., Battaglia Francesco P., Jensen Ole, Moser Edvard I., Moser May-Britt. Path Integration and the Neural Basis of the 'Cognitive Map' // Nature Reviews Neuroscience. VIII 2006. 7, 8. 663–678.

Mehta Mayank R. Neuronal Dynamics of Predictive Coding // The Neuroscientist. XII 2001. 7, 6. 490–495.

Mehta Mayank R. From Synaptic Plasticity to Spatial Maps and Sequence Learning // Hippocampus. 2015. 25, 6. 756–762.

Mhatre Himanshu, Gorchetchnikov Anatoli, Grossberg Stephen. Grid Cell Hexagonal Patterns Formed by Fast Self-Organized Learning within Entorhinal Cortex // Hippocampus. II 2012. 22, 2. 320–334.

Moser Edvard I., Moser May-Britt. A Metric for Space // Hippocampus. XII 2008. 18, 12. 1142–1156.

Moser Edvard I., Moser May-Britt. Grid Cells and Neural Coding in High-End Cortices // Neuron. X 2013. 80, 3. 765–774.

Moser Edvard I., Moser May-Britt, McNaughton Bruce L. Spatial Representation in the Hippocampal Formation: A History // Nature Neuroscience. X 2017. 20, 11. 1448–1464.

Moser Edvard I., Moser May-Britt, Roudi Yasser. Network Mechanisms of Grid Cells // Phil. Trans. R. Soc. B. II 2014a. 369, 1635. 20120511.

Moser Edvard I., Roudi Yasser, Witter Menno P., Kentros Clifford, Bonhoeffer Tobias, Moser May-Britt. Grid Cells and Cortical Representation // Nature Reviews Neuroscience. VII 2014b. 15, 7. 466–481.

Muller R. U., Kubie J. L., Ranck J. B. Spatial Firing Patterns of Hippocampal Complex-Spike Cells in a Fixed Environment // Journal of Neuroscience. VII 1987. 7, 7. 1935–1950.

O'Keefe J. Place Units in the Hippocampus of the Freely Moving Rat // Experimental Neurology. IV 1976. 51, 1. 78–109.

O'Keefe J., Dostrovsky J. The Hippocampus as a Spatial Map. Preliminary Evidence from Unit Activity in the Freely-Moving Rat. // Brain Res. XI 1971. 34, 1. 171–175.

O'Keefe J., Recce M. L. Phase Relationship between Hippocampal Place Units and the EEG Theta Rhythm // Hippocampus. VII 1993. 3, 3. 317–330.

O'Keefe John, Burgess Neil. Dual Phase and Rate Coding in Hippocampal Place Cells: Theoretical Significance and Relationship to Entorhinal Grid Cells // Hippocampus. 2005. 15, 7. 853–866.

O'Keefe John, Nadel Lynn. The Hippocampus as a Cognitive Map. XII 1979.

Olshausen Bruno A, Field David J. Sparse Coding of Sensory Inputs // Current Opinion in Neurobiology. VIII 2004. 14, 4. 481–487.

Park EunHye, Dvorak Dino, Fenton André A. Ensemble Place Codes in Hippocampus: CA1, CA3, and Dentate Gyrus Place Cells Have Multiple Place Fields in Large Environments // PLOS ONE. VII 2011. 6, 7. e22349.

Petersen Carl C. H., Hahn Thomas T. G., Mehta Mayank, Grinvald Amiram, Sakmann Bert. Interaction of Sensory Responses with Spontaneous Depolarization in Layer 2/3 Barrel Cortex // Proceedings of the National Academy of Sciences. XI 2003. 100, 23. 13638–13643.

Pilly Praveen K., Grossberg Stephen. Spiking Neurons in a Hierarchical Self-Organizing Map Model Can Learn to Develop Spatial and Temporal Properties of Entorhinal Grid Cells and Hippocampal Place Cells // PLoS ONE. IV 2013. 8, 4. e60599.

Ranck JB. Head-Direction Cells in the Deep Cell Layers of Dorsal Presubiculum in Freely Moving Rats // Society for Neuroscience Abstracts. 1984. 10.

Rich P. Dylan, Liaw Hua-Peng, Lee Albert K. Large Environments Reveal the Statistical Structure Governing Hippocampal Representations // Science. VIII 2014. 345, 6198. 814–817.

Rowland David C., Roudi Yasser, Moser May-Britt, Moser Edvard I. Ten Years of Grid Cells // Annual Review of Neuroscience. VII 2016. 39. 19–40.

Royer Sébastien, Sirota Anton, Patel Jagdish, Buzsáki György. Distinct Representations and Theta Dynamics in Dorsal and Ventral Hippocampus // Journal of Neuroscience. II 2010. 30, 5. 1777–1787.

Sargolini Francesca, Fyhn Marianne, Hafting Torkel, McNaughton Bruce L., Witter Menno P., Moser May-Britt, Moser Edvard I. Conjunctive Representation of Position, Direction, and Velocity in Entorhinal Cortex // Science. V 2006. 312, 5774. 758–762.

Savelli Francesco, Knierim James J. Origin and Role of Path Integration in the Cognitive Representations of the Hippocampus: Computational Insights into Open Questions // Journal of Experimental Biology. II 2019. 222, Suppl_1. jeb188912.

Savelli Francesco, Yoganarasimha D., Knierim James J. Influence of Boundary Removal on the Spatial Representations of the Medial Entorhinal Cortex // Hippocampus. XII 2008. 18, 12. 1270–1282.

Schweinfurth Manon K. The Social Life of Norway Rats (Rattus Norvegicus) // eLife. IV 2020. 9. e54020.

Sharp P. E., Kubie J. L., Muller R. U. Firing Properties of Hippocampal Neurons in a Visually Symmetrical Environment: Contributions of Multiple Sensory Cues and Mnemonic Processes // Journal of Neuroscience. IX 1990. 10, 9. 3093–3105.

Shipston-Sharman Oliver, Solanka Lukas, Nolan Matthew F. Continuous Attractor Network Models of Grid Cell Firing Based on Excitatory–Inhibitory Interactions // The Journal of Physiology. XI 2016. 594, 22. 6547–6557.

Si Bailu, Kropff Emilio, Treves Alessandro. Grid Alignment in Entorhinal Cortex // Biological Cybernetics. VIII 2012. 106, 8-9. 483–506.

Si Bailu, Treves Alessandro. A Model for the Differentiation between Grid and Conjunctive Units in Medial Entorhinal Cortex // Hippocampus. XII 2013. 23, 12. 1410–1424.

Skaggs William E., McNaughton Bruce L., Wilson Matthew A., Barnes Carol A. Theta Phase Precession in Hippocampal Neuronal Populations and the Compression of Temporal Sequences // Hippocampus. 1996. 6, 2. 149–172.

Solstad Trygve, Boccara Charlotte N., Kropff Emilio, Moser May-Britt, Moser Edvard I. Representation of Geometric Borders in the Entorhinal Cortex // Science. XII 2008. 322, 5909. 1865–1868.

Spanne Anton, Jörntell Henrik. Questioning the Role of Sparse Coding in the Brain // Trends in Neurosciences. VII 2015. 38, 7. 417–427.

Stella Federico, Si Bailu, Kropff Emilio, Treves Alessandro. Grid Cells on the Ball // Journal of Statistical Mechanics: Theory and Experiment. 2013. 2013, 03. P03013.

Stella Federico, Treves Alessandro. The Self-Organization of Grid Cells in 3D // eLife. III 2015. 4. e05913.

Stella Federico, Urdapilleta Eugenio, Luo Yifan, Treves Alessandro. Partial Coherence and Frustration in Self-Organizing Spherical Grids // Hippocampus. 2020. 30, 4. 302–313.

Stensola Hanne, Stensola Tor, Solstad Trygve, Froland Kristian, Moser May-Britt, Moser Edvard I. The Entorhinal Grid Map Is Discretized // Nature. XII 2012. 492, 7427. 72–78.

Stensola Tor, Stensola Hanne, Moser May-Britt, Moser Edvard I. Shearing-Induced Asymmetry in Entorhinal Grid Cells // Nature. II 2015. 518, 7538. 207–212.

Stepanyuk Andrey. Self-Organization of Grid Fields under Supervision of Place Cells in a Neuron Model with Associative Plasticity // Biologically Inspired Cognitive Architectures. VII 2015. 13. 48–62.

Sutherland Gary R, McNaughton Bruce. Memory Trace Reactivation in Hippocampal and Neocortical Neuronal Ensembles // Current Opinion in Neurobiology. IV 2000. 10, 2. 180–186.

Taube J. S., Muller R. U., Ranck J. B. Head-Direction Cells Recorded from the Postsubiculum in Freely Moving Rats. I. Description and Quantitative Analysis // The Journal of Neuroscience. II 1990a. 10, 2. 420–435.

Taube J. S., Muller R. U., Ranck J. B. Head-Direction Cells Recorded from the Postsubiculum in Freely Moving Rats. II. Effects of Environmental Manipulations // The Journal of Neuroscience. II 1990b. 10, 2. 436–447.

Taxidis Jiannis, Pnevmatikakis Eftychios A., Dorian Conor C., Mylavarapu Apoorva L., Arora Jagmeet S., Samadian Kian D., Hoffberg Emily A., Golshani Peyman. Differential Emergence and Stability of Sensory and Temporal Representations in Context-Specific Hippocampal Sequences // Neuron. XII 2020. 108, 5. 984–998.e9.

Torao-Angosto Melody, Manasanch Arnau, Mattia Maurizio, Sanchez-Vives Maria V. Up and Down States During Slow Oscillations in Slow-Wave Sleep and Different Levels of Anesthesia // Frontiers in Systems Neuroscience. 2021. 15.

Tukker John J, Beed Prateep, Brecht Michael, Kempter Richard, Moser Edvard I, Schmitz Dietmar. Microcircuits for Spatial Coding in the Medial Entorhinal Cortex // Physiological Reviews. VII 2021.

Turi Gergely F., Chen Xinyue, Teng Sasa, Lim Emily CY, Dias Carla, Hu Ruining, Zhen Fenghua, Peng Yueqing. Modulation of Infraslow Oscillation in the Dentate Gyrus during Non-REM Sleep. V 2023. 2023.05.12.540575.

Turing A. M. The Chemical Basis of Morphogenesis // Philosophical Transactions of the Royal Society of London B: Biological Sciences. VIII 1952. 237, 641. 37–72.

Urdapilleta Eugenio, Si Bailu, Treves Alessandro. Self-Organization of Modular Activity of Grid Cells // Hippocampus. VIII 2017.

Urdapilleta Eugenio, Troiani Francesca, Stella Federico, Treves Alessandro. Can Rodents Conceive Hyperbolic Spaces? // Journal of The Royal Society Interface. VI 2015. 12, 107. 20141214.

Väyrynen Tommi, Helakari Heta, Korhonen Vesa, Tuunanen Johanna, Huotari Niko, Piispala Johanna, Kallio Mika, Raitamaa Lauri, Kananen Janne, Järvelä Matti, Palva J. Matias, Kiviniemi Vesa. Sleep Specific Changes in Infra-Slow and Respiratory Frequency Drivers of Cortical EEG Rhythms. I 2023. 2023.01.20.524831.

Waller David, Nadel Lynn. Handbook of Spatial Cognition. X 2012.

Ward Lawrence M. Synchronous Neural Oscillations and Cognitive Processes // Trends in Cognitive Sciences. XII 2003. 7, 12. 553–559.

Watson Brendon O. Cognitive and Physiologic Impacts of the Infraslow Oscillation // Frontiers in Systems Neuroscience. 2018. 12.

Wernle Tanja, Waaga Torgeir, Mørreaunet Maria, Treves Alessandro, Moser May-Britt, Moser Edvard I. Integration of Grid Maps in Merged Environments // Nature Neuroscience. XII 2017. 1.

Widloski John, Fiete Ila R. A Model of Grid Cell Development through Spatial Exploration and Spike Time-Dependent Plasticity // Neuron. VII 2014. 83, 2. 481–495.

Wills Tom, Cacucci Francesca, Burgess Neil, O'Keefe John. Development of the Hippocampal Cognitive Map in Pre-weanling Rats // Science (New York, N.Y.). VI 2010. 328, 5985. 1573–1576.

Wilson M. A., McNaughton B. L. Dynamics of the Hippocampal Ensemble Code for Space // Science. VIII 1993. 261, 5124. 1055–1058.

Wilson M. A., McNaughton B. L. Reactivation of Hippocampal Ensemble Memories during Sleep // Science. VII 1994. 265, 5172. 676–679.

Witter Menno P., Moser Edvard I. Spatial Representation and the Architecture of the Entorhinal Cortex // Trends in Neurosciences. XII 2006. 29, 12. 671–678.

Yartsev Michael M., Ulanovsky Nachum. Representation of Three-Dimensional Space in the Hippocampus of Flying Bats // Science. IV 2013. 340, 6130. 367–372.

Yartsev Michael M., Witter Menno P., Ulanovsky Nachum. Grid Cells without Theta Oscillations in the Entorhinal Cortex of Bats // Nature. XI 2011. 479, 7371. 103–107.

Yoon KiJung, Lewallen Sam, Kinkhabwala Amina A., Tank David W., Fiete Ila R. Grid Cell Responses in 1D Environments Assessed as Slices through a 2D Lattice // Neuron. III 2016. 89, 5. 1086–1099.

Young B. J., Fox G. D., Eichenbaum H. Correlates of Hippocampal Complex-Spike Cell Activity in Rats Performing a Nonspatial Radial Maze Task // Journal of Neuroscience. XI 1994. 14, 11. 6553–6563.

Zhang K. Representation of Spatial Orientation by the Intrinsic Dynamics of the Head-Direction Cell Ensemble: A Theory // Journal of Neuroscience. III 1996. 16, 6. 2112–2126.

Zilli Eric A. Models of Grid Cell Spatial Firing Published 2005–2011 // Frontiers in Neural Circuits. IV 2012. 6.

van Strien N. M., Cappaert N. L. M., Witter M. P. The Anatomy of Memory: An Interactive Overview of the Parahippocampal–Hippocampal Network // Nature Reviews Neuroscience. IV 2009. 10, 4. 272–282.

Acknowledgements

I would like to express my sincere gratitude to my supervisor, Alessandro, for welcoming me into the group and introducing me to the fascinating world of spatial cognition and brain science. Throughout my journey, Alessandro has been a constant source of guidance and support, always ensuring that I comprehend the intricacies of the subject matter. Knowing that Alessandro's brilliant mind has thoroughly processed and analyzed these concepts instills me with confidence and tranquility.

My deep sincere gratitude also goes to Professor Mayank, for introducing me to the wonderful world of brain oscillation. I have gained invaluable insights into various aspects of data analysis, including what is data, how to process the data, and how an understanding of the data been formed. I am truly grateful for his mentorship and the knowledge he has imparted to me.

I would like also to extend my deepest gratitude to Professor Bailu, for his invaluable guidance and unwavering support in keeping me on the right track throughout my research journey. His expertise and collaboration have been instrumental in exploring the fascinating topics of grid pattern anchoring and distortion. I am truly grateful for the opportunity to work alongside Professor Bailu and for their continuous guidance, which has significantly contributed to the progress of my work.

I also thank Mathew, Davide Crepaldi, Domenica Bueti, Davide Zoccolan, and all the faculty for making CNS a big nice party.

Also thanks to friends, some of whom we may haven't talked with each for a while, but thanks for strolling in my mind time by time.

Last but very important, thanks to my wife, my daughter, my parents, and my parents-in-law, thanks for all kinds of support.